» DELIVERABLE D3.3

EVALUATION OF MATERIALS CHARACTERIZATIONS

www.salient-project.eu

Funded by the European Union

PROJECT INFORMATION

Project information	**GA No. 101069600** **"Novel Concepts for SAfer, LIghter, Circular and Smarter VehiclE Structure DesigN for Enhanced CrashworThiness and Higher Compatibility"**
Project acronym	SALIENT
Funding scheme	RIA
Starting date	01 Sept 2022
End date	31 Aug 2025
Duration	36 months
Coordinator	CTAG (Spain)
Project website	*www.salient-project.eu*

DELIVERABLE/REPORT INFORMATION

Deliverable n°	**D3.3**
Deliverable title	Evaluation of materials characterizations
WP No. & title	WP3 - Innovations in Materials Development and Manufacturing Processes
WP Leader	tPE
Contributors	CID
	ASAS
	CTAG
	tPE
	FRA
	CRF
	UNN
	IDI
	VIF

Type	R - Report
Authors	Jorge Velasco (CID)
	Patryk Nossol (FRA), Arham Saleem (FRA), Robert Meltke (FRA)
	Tolgahan Çali, Ilyas Artunç Sari (ASAŞ)
	Sebastian Iwan, Frank Schettler (tPE)
	Engy Ghoniem, Richard Fu, Ahmed Elmarakbi (UNN)
	Vanessa Ventosinos, Miguel Moldes (CTAG)
	Matteo Basso (CRF)
Reviewers	Ahmed Elmarakbi (UNN), Matteo Basso (CRF)
Submission Date	30.09.2023

TRACK OF CHANGES

Version	Date	Author	Description
V[0.0]	11.09.2023	Jorge Velasco	Preliminary version including Table of Contents
V[0.1]	13.09.2023	Jorge Velasco	Content included in sections 3, 4.1 and 5.
V[0.2]	17.09.2023	Jorge Velasco	Content added to sections 3, 4 and 5.
V[0.3]	26.09.2023	Jorge Velasco	Content added to sections 1, 2 and 5.
V[0.4]	28.09.2023	Jorge Velasco	Full draft version
V[0.5]	29.09.2023	Jorge Velasco	Final version

DISSEMINATION LEVEL

Abbreviation	Meaning	
PU	Public, fully open (Deliverables flagged as public will be automatically published in CORDIS project's page).	[X]
SEN	Sensitive, limited under the conditions of the Grant Agreement.	

LIST OF ABBREVIATIONS

Abbreviation	Meaning
AFM	Atomic Force Microscope
CAD	Computer Aided Design
CAM	Computer Aided Manufacturing
CC	Compact Compression
CF	Carbon Fibre
CFRP	Carbon Fibre Reinforced Polymer
CNC	Computer Numerical Control
CT	Compact Tension
C-ELS	Calibrated End-Loaded Split
DCB	Double Cantilever Beam
DIC	Digital Image Correlation
DMA	Dynamic Mechanical Analyzer
EDX	Energy Dispersive X-Ray Analysis
FEM	Finite Element Method
FES	Front End Structure
ILSS	Inter-Laminar Shear Strength
LVDT	Linear Variable Displacement Transducer
PA6	Polyamide-6
PV	Prüfvorschrift (Test specification)
QS	Quasi-static
RT	Room Temperature
SEM	Scanning Electron Microscopy
SMA	Shape Memory Alloy
SPM	Scanning Probe Microscope
TP	Thermoplastic

UD	Unidirectional
XRD	X-Ray Diffraction

TABLE OF CONTENTS

LIST OF FIGURES

LIST OF TABLES

1. EXECUTIVE SUMMARY

Innovations in materials development and manufacturing processes (WP3 of Salient project) require all kinds of characterization activities in order to validate the appropriateness of the developments made. Aligned with that, the main objective of the deliverable D3.3 from Task 3.2 was to carry out and describe a tailored while comprehensive set of micro- and macrostructural characterization tests at coupon level for the four materials considered for the development of the FES concepts within Salient: aluminium, composite (TP/CFRP), hybrid (Al + TP/CFRP) and SMA/CFRP. Several partners were involved in this task according to their expertise on the development of materials (link to T3.1/T3.3) and their related manufacturing processes (link to T3.4) and the simulation of its behaviour (D3.2 from T3.2 and link to T5.2).

The tests were conducted in such a way that the obtained results can be used to corroborate their performance against the specific demands of each component in the FES, according to the designs being made in WP2. The main objective of the testing campaign on the aluminium and TP/CFRP materials was to provide the inputs for the development of material cards for simulation codes. Therefore, a strong focus was put on assessing the crashworthiness of these materials through a wide variety of quasi-static and dynamic tests and of different load cases and material orientations. Failure analysis was also a major objective, and consequently specific tests were implemented for that purpose. In the case of the hybrid material, the main objective was to study its durability in the long term, when subjected to cyclic loading exposures. The different physical properties of the aluminium and the TP and the bonding between them imply different response to cyclic loads that needs to be analysed to ensure the suitability for automotive structural applications. Finally, due to the innovativeness of the SMA/CFRP material concept, the main objective of the test campaign was to evaluate its potential to modify the behaviour of the FES in a crash event, while at the same time to assess the quality of the integration of the SMA wires within the TP/CFRP.

The outcomes of T3.2, D3.2 provide valuable feedback and real data to the partners to enhance the materials design, the associated manufacturing process, the simulation models at material and component level, as well as the design of the FES component in further iteration loops.

2. INTRODUCTION

The overall objective of WP3 of Salient is to optimize advanced lightweight materials (aluminium alloys, thermoplastic continuous fibre reinforced plastic (TP/CFRP), hybrid composite materials and shape memory alloys embedded in TP/CFRP (SMA/CFRP)) for their application in the design of the FES concepts within WP2, with an emphasis on sustainability, recycling and reuse. Characterization activities and mechanical testing are essential in order to gain knowledge on advanced materials behaviour including failure mechanisms, as well as to find the best application for each material, either individually or in combination with others. The design, planning and execution of a tailored testing campaign for each of the four aforementioned materials is the main objective of D3.3 derived from Task 3.2, dated from M5-M13 of the project. Closely linked to it, the results obtained during the testing campaign feed the development of material cards also within Task 3.2.

As such, a multidisciplinary team has participated in the mechanical testing and characterization activities described in this deliverable. On the one hand, tPE, FRA, UNN and ASAŞ manufactured and provided coupons as required per each test setup and objective. On the other hand, CID, CTAG, CRF and FRA employed their expertise on testing activities to carry out the tests successfully as per relevant standards in each case, and also proposed and designed specific testing procedures where needed. In order to generate a comprehensive set of results suitable to be used for material card development purposes, IDI and VIF provided support through all the process and established specific requirements for some of the tests executed. Finally, UNN carried out several different microstructural tests (SEM, SPM, XRD, scattering) to characterize materials' pre- and post-failure microstructure and damage.

The overall planning and the detailed description of all testing procedures and derived results for each material are provided in the subsequent sections of this deliverable. As such, Section 3 gathers all the information regarding the aluminium alloy Al6063. In Section 4, the testing campaign for the TP/CFRP is described. The hybrid material evaluation including durability assessment is reported in Section 5. Finally, the behaviour of different SMA/CFRP concepts together with the assessment of its potential to modify the pre-defined behaviour of the composite in or after a crash is detailed in Section 5. A discussion on the test results along with recommendation for further testing and/or optimizations of the materials design is provided for each material.

3. ALUMINIUM AL6063 CHARACTERIZATION

The testing campaign designed for the Aluminium material developed by ASAŞ aims at generating a broad while at the same time comprehensive knowledge about the extruded Al6063 behaviour at micro- and macroscales. Therefore, not only aspects related to the performance of the material in different static and/or dynamic load cases are characterized, but also the failure mechanisms and their implications at microstructural level are investigated through a variety of tests at coupon scale. Also, specific tests requested by IDI and VIF to get data needed to feed advanced material cards for simulation codes (LS-Dyna) have also been included.

As such, the overall scope of the testing campaign for the Al6063 is summarized in Table 1. In all tests except the mini-tensile tests (that are aimed to evaluating the anisotropy of the material), the coupons have a 0º orientation with respect to the direction of extrusion of the profiles from which they were machined. The procedures and results of each test can be found in the subsequent sections of this chapter.

Table 1: Overview of test campaign performed on Al6063

Test name	Scale	Goal
SEM	Micro	Characterize the microstructure of the material before and after failure
X-ray diffraction	Micro	Determine the aluminium's crystalline structure
SPM	Micro	Investigate the surface properties of the material
Scattering	Micro	Investigate the internal structure of the material
Static tensile	Macro	Test the behaviour of the material when subjected to tensile forces, at quasi-static velocity
Dynamic tensile	Macro	Test the behaviour of the material when subjected to dynamic tensile forces, at several strain rates
Mini-tensile tests	Macro	To evaluate anisotropy of the material after the extrusion process
Static biaxial	Macro	Test the behaviour of the material when subjected to biaxial stress states, at quasi-static velocity
Static shear	Macro	Test the behaviour of the material when subjected to shear stress states, at quasi-static velocity
Static bending (3P)	Macro	Test the behaviour of the material when subjected to flexural loads, at quasi-static velocity
Creep	Macro	Characterize the long-term behaviour of the material
DMA	Micro	Evaluate dynamic properties of the material (frequency domain)

3.1 MANUFACTURING OF COUPONS

Aluminium coupons were machined by a 5-axis CNC Milling Machine owing to CAM technology. In order to shorten operation time and energy consumption, the CAD data for CAM programming was designed to maximize the amount of specimens. Sample designs were taken from the standards. Feed rate, rotational speed, and cutting depth were assigned regarding the opted optimum stock material and cutting tool. Examples of the coupons machined for testing purposes are presented in Figure 1 below.

Figure 1: Examples of Al6063 coupons for testing. From left to right: QS tensile, dynamic tensile, shear and biaxial (small notch) coupons.

Besides, extruded profiles were also used to manufacture coupons for microstructural tests through milling. An example of this operation and the obtained coupons is shown in Figure 2.

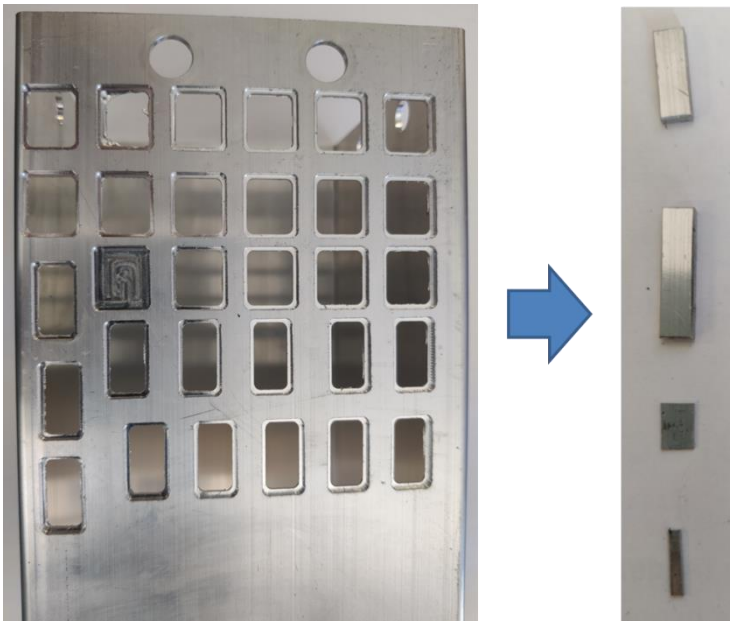

Figure 2: Manufacturing of coupons from extruded profiles for dynamic properties and microstructural characterization. Left: profile after milling operation; Right: specimens obtained

Further details about the design and manufacturing of the Al6063 alloy can be found in D3.1, here only a brief description is provided focusing on the close relationship existing between material manufacturing (T3.1) and material characterization (T3.2).

3.2 MICROSTRUCTURAL CHARACTERIZATION

3.2.1 MICROSTRUCTURAL AND FRACTOGRAPHY CHARACTERIZATION

Microstructural and fractography characterisations were performed to explore the Al alloy's microstructures and fracture surface details and investigate the topographical features and optical scattering phenomena, including surface roughness and morphology effects, which are vital for understanding the failure mechanisms under different loading conditions.

Firstly, the microstructural analysis of the AL6063 surface and fracture surfaces were characterised using a Scanning Electron Microscope (SEM) at Northumbria University, UK. For SEM analysis, the SEM operation parameters include an accelerating voltage of 10-20 kV and various magnifications determined per condition to reveal the details of morphology and compositions. With one example shown in Figure 3, the surface evaluation reveals the alloy's anisotropic rolling direction and proves surface-free defects.

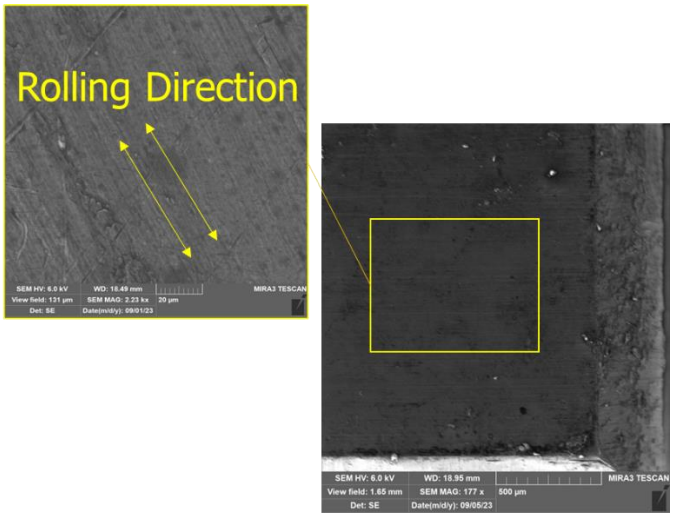

Figure 3 SEM morphologies for AL6063 surface.

Figure 4 comprehensively presents the fracture morphologies under various loading conditions. Figure 4 (a) illustrates the fracture morphology resulting from a small notch impact test, offering insights into the fracture mechanism (i.e., ductile fracture with dimples). Notably, the fracture surface displays a plane inclined at an angle relative to the plane perpendicular to the specimen's axis. Figure 4 (b), (c), and (d) depict the fracture morphologies observed during tensile testing for specimens with anisotropic orientations of 0, 45, and 90 degrees, respectively. In all the cases, a multitude of sizable and deep equiaxed dimples were observed on the fractured surfaces, a characteristic of the typical ductile fracture. Figure 5 shows one example of the fractography of the Al6063 alloy under the biaxial loading. We can observe a much flatter fracture surface compared to Figure 4 (a-d). In Figure 5, many dimples are indicative of an intergranular mode, and good ductility is still evident on the fracture surfaces, albeit with shallower depths and a higher number of voids.

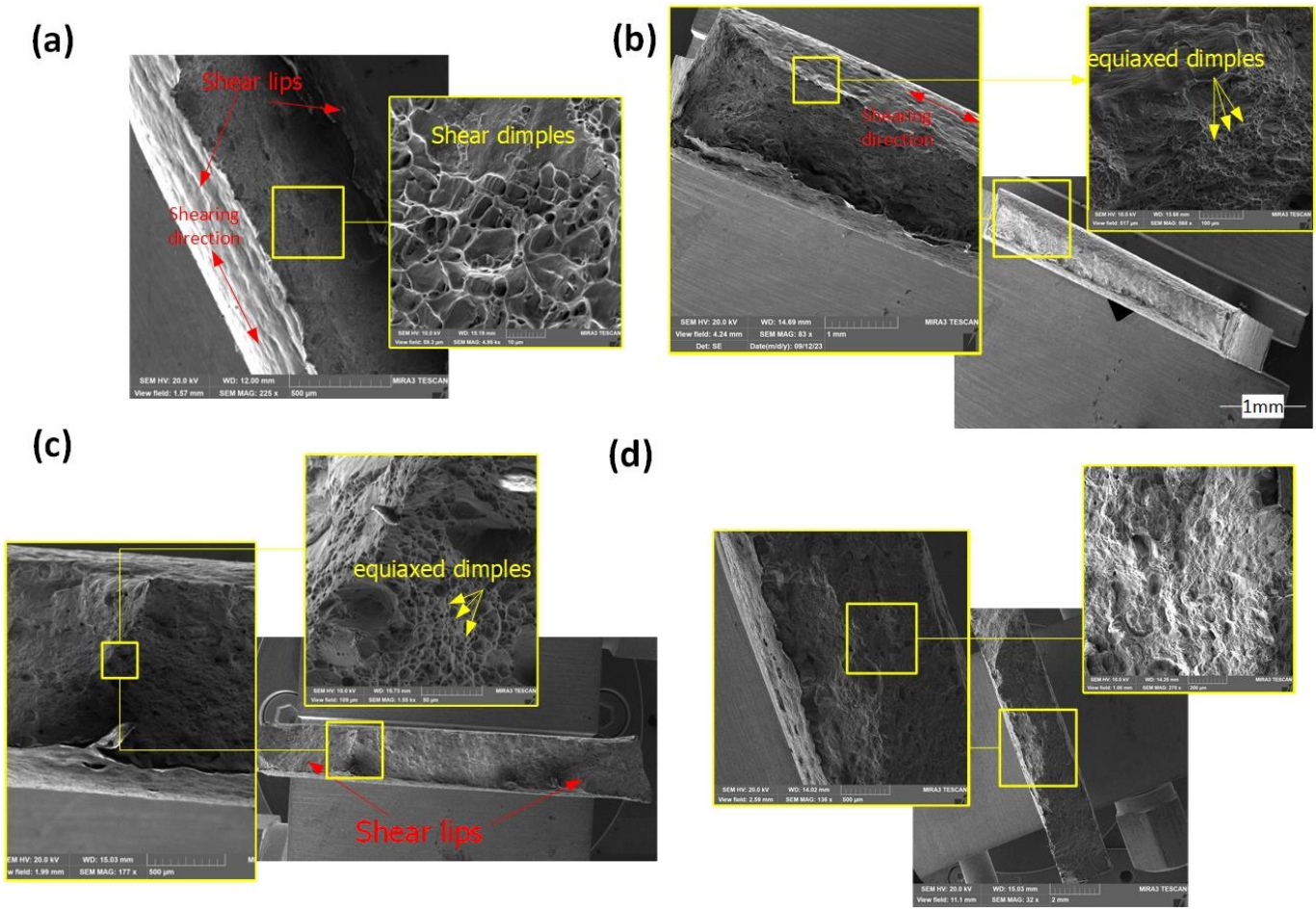

Figure 4. SEM for the fracture surface of the AL6063 alloy under different loading conditions, (a) for small notch test, (b - d) for tensile testing for samples with different anisotropy orientations 0, 45, and 90◦ respectively.

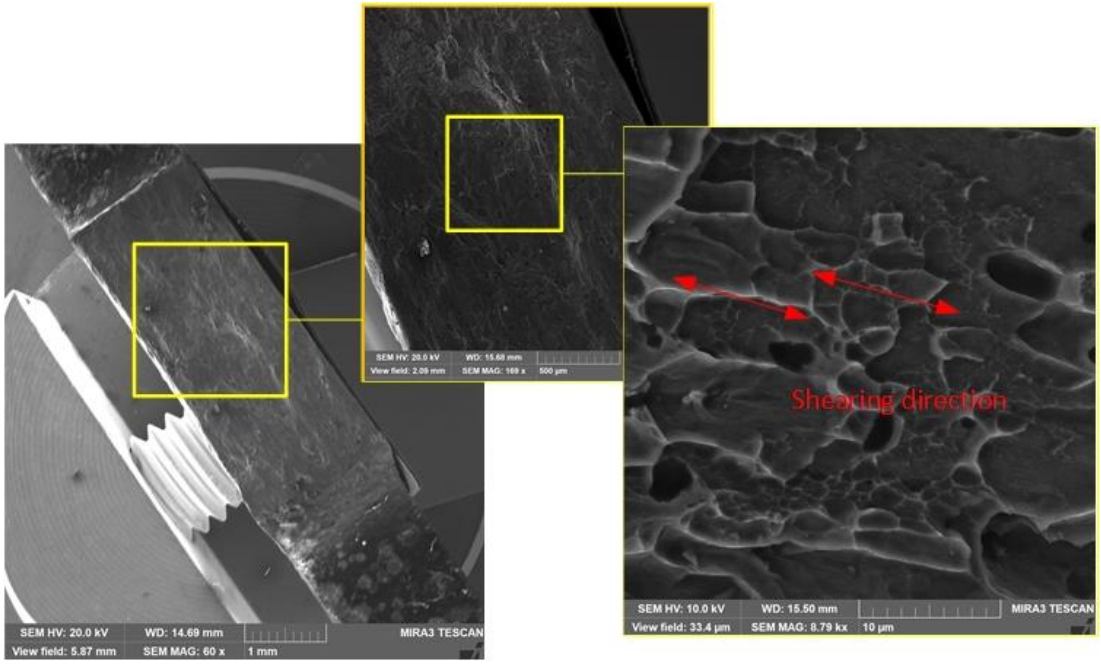

Figure 5. SEM fracture morphology of Al6063 under Biaxial loading.

3.2.1 STRUCTURE AND SURFACE CHARACTERIZATIONS

UNN conducted a comprehensive analysis of structural and surface characteristics of the as-received Al6063 obtained from CID, with some of examples for the corresponding test outcomes presented in Figure 6. Information regarding to the crystalline structures of aluminium 6063 was obtained through X-ray diffraction (XRD) analysis (Northumbria University, UK). One of the examples of XRD profiles of the Al6063 sample from CID in its as-received state is depicted in Figure 6(a). This pattern reveals the presence of fundamental diffraction peaks associated with α-Al, possessing a face-centred cubic (FCC) crystal structure. The XRD patterns confirm a single-phase structure, with a notable preference for the α phase's (111) peak at approximately 2θ = 38.3 degrees. The presence of other prominent peaks corresponding to (200) α, (220) α, and (311) α substantiates a random distribution of grain orientations [1].

To assess the damping characteristics of Al6063, a Dynamic-Mechanical Analyzer (DMA) from PerkinElmer® (DMA 8000), located at Northumbria University, UK, was utilised. Figure 6(b) displays examples of the DMA test results concerning damping properties. It is worth noting that these results did not yield substantial information for temperature ranges up to 350 degrees Celsius, primarily because, at this temperature, the machine is better suited for assessing thermoplastics and elastomers.

An optical scattering test was conducted using a laser interferometer at Northumbria University, UK, and one of the obtained results is presented in Figure 6(c). The laser interferometer generates light scattering and interferometric effects. Also, it shows morphology and roughness profiles with concave–convex structures in different directions, indicating an Al6063 smooth surface with a maximum roughness value of approximately 8.2 micrometres.

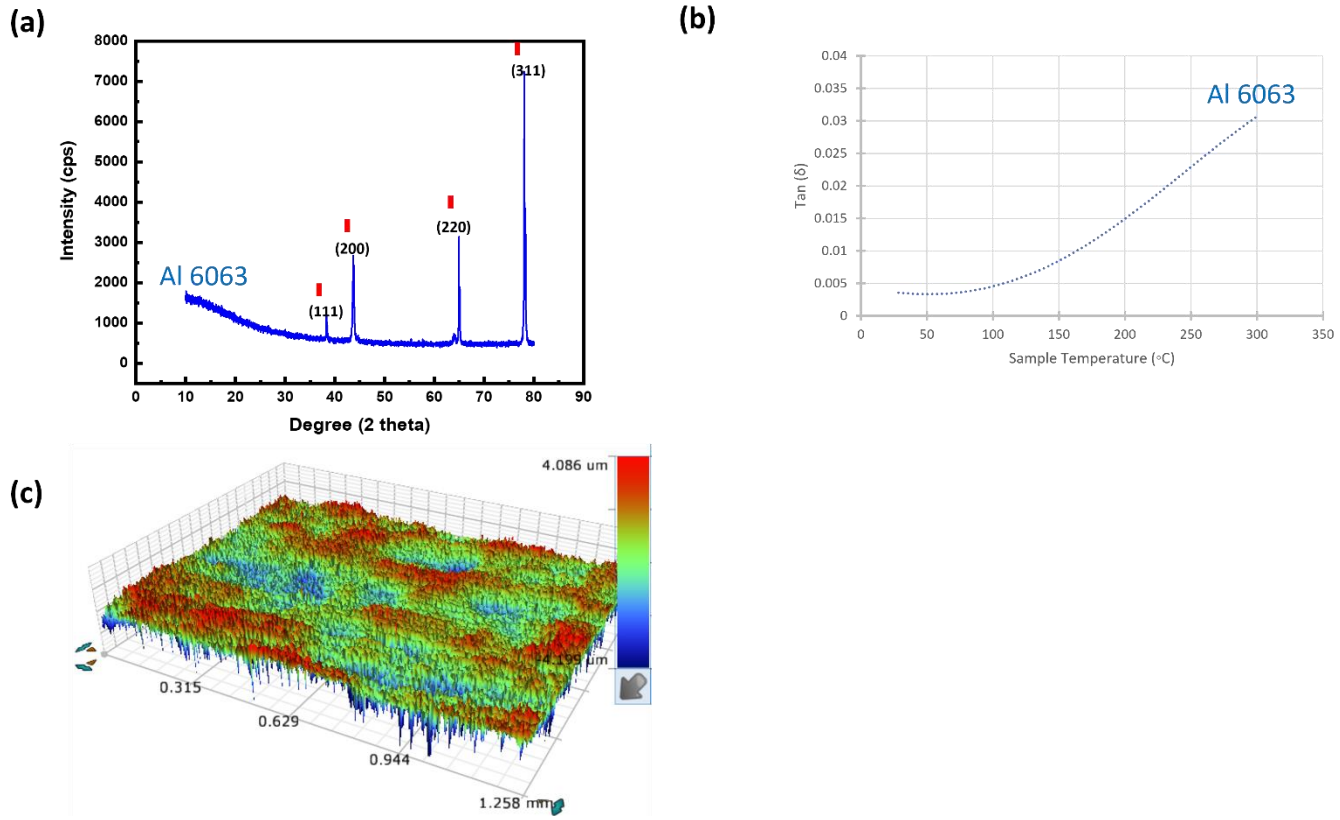

Figure 6.Aluminum 6063 Structural and surface characterisations results, (a) X-ray diffraction profile of Al 6063, (b) Dynamic mechanical analysis (DMA) test results, and (C) Scattering by laser interferometer.

3.2.2 CREEP RECOVERY AND STRESS RELAXATION TESTS

A tension clamp was employed to conduct a creep/ recovery and stress relaxation tests using a PerkinElmer® DMA 8000 instrument, Northumbria University. The test specimens had a dimension of 10 mm × 2 mm × 0.5 mm. Figure 7 displays one example of the strain-time and stress-time curves which illustrate the creep/recovery and stress relaxation characteristics of Al6063 alloy. The results example depicted in Figure 7(a) involved a creep and recovery cycle conducted at an operating temperature of 85°C. To ensure thermal equilibrium, the specimens were allowed to stabilize at this temperature for a 5-minute period before subjecting them to a consistent temperature and stress level. A constant load of 4N was then imposed on the material for a duration of 15 minutes at the 85°C temperature, followed by an identical 15-minute recovery phase. These specific creep testing conditions were maintained for a total duration of 30 minutes to observe the material's creep and recovery behaviours. Notably, the specimens did not experience creep rupture during the tests due to the relatively lower stress levels and shorter durations employed. Furthermore, the recovery phase showcased the material's ability to partially regain its original shape once the stress was removed, highlighting its viscoelastic properties.

The stress relaxation characteristics of AL6063 were explored utilising a DMA8000 dynamic mechanical analyser. The experimental setup involved applying a predetermined stress level of 0.5 N to a 10 mm × 2 mm × 0.5 mm AL6063 sample, followed by monitoring its response as it gradually eased over a 10-minute duration. The stress relaxation profile typically exhibits two distinct phases: an initial variable-rate relaxation phase marked by rapid stress reduction and a subsequent steady-rate relaxation phase characterised by a slower and more consistent decrease in stress levels. In accordance with Figure 7(b), our observations for the shown example indicated the presence of the steady-state relaxation phenomenon. Stress relaxation assessments serve as a valuable tool for evaluating the formability of aluminium alloys, with higher stress relaxation values indicating improved formability efficiency and reduced spring-back tendencies.

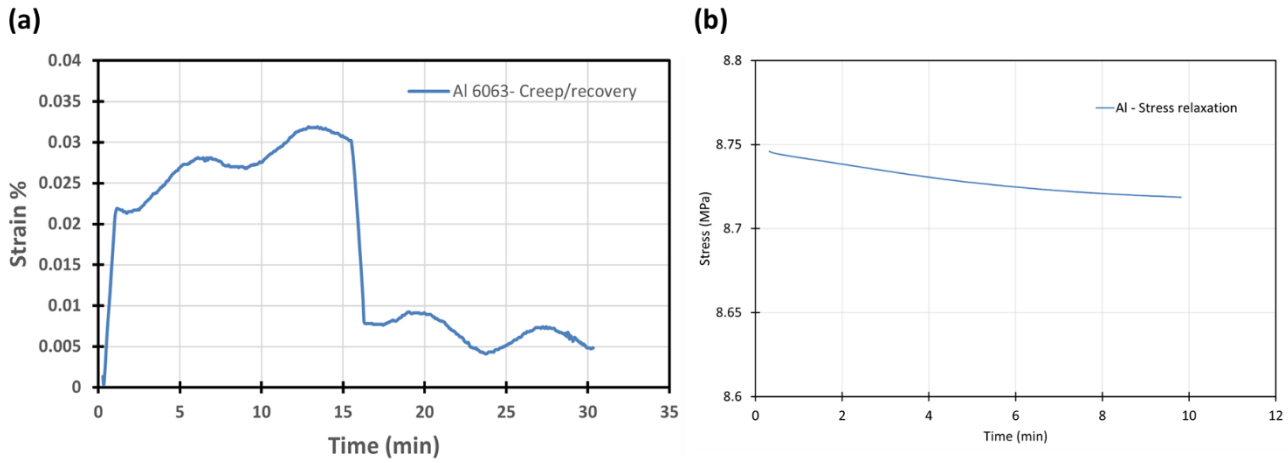

Figure 7. Creep/recovery and stress relaxation curves of Al6063 at constant temperature of 85°.

3.3 TENSILE TESTS

3.3.1 TEST PROCEDURE

Tensile testing of aluminium samples at room temperature and QS velocity was performed according to the prescriptions of the standard ASTM E8 [2], using a standard coupon geometry of 2mm thickness (Figure 8).

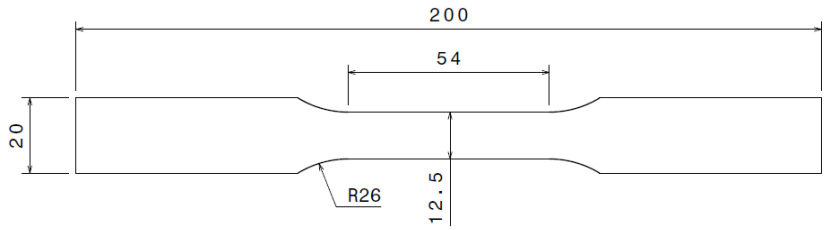

Figure 8: Specimen dimensions of the QS tensile test coupons as per ASTM E8.

Initially two specimens were employed to fix the boundary conditions of the test. The displacement speed of the actuator was set to 6 mm/min, in order to get a target strain rate of $0.005s^{-1}$, measured taking as reference a global gauge length of 50mm located around the centre of the specimen, in the longitudinal direction. After that, 5 additional specimens were tested in the aforementioned conditions to gather representative results.

Moreover, DIC technique was applied to this test to enhance and maximize the data collection process, with a view of using this data to enhance the correlation accuracy the material cards. DIC technique is a non-contact method that allows measuring 2D (setup with one high-speed camera) or 3D (setup with two high-speed cameras) displacement and strain fields, providing full-field measurements over the entire optically visible image, in contrast with conventional measurements using extensometers or LVDT sensors that are limited to one single axis displacement/strain measurements. Furthermore, DIC technique does not have any limitation in what concerns the material to be measured or the speed at which the test is executed, being able to provide results at sub-pixel accuracy [3].

To employ DIC technique successfully, a speckled pattern has to be painted on the specimens so that the system is able to track greyscale patterns throughout the test. An example is shown in Figure 9.

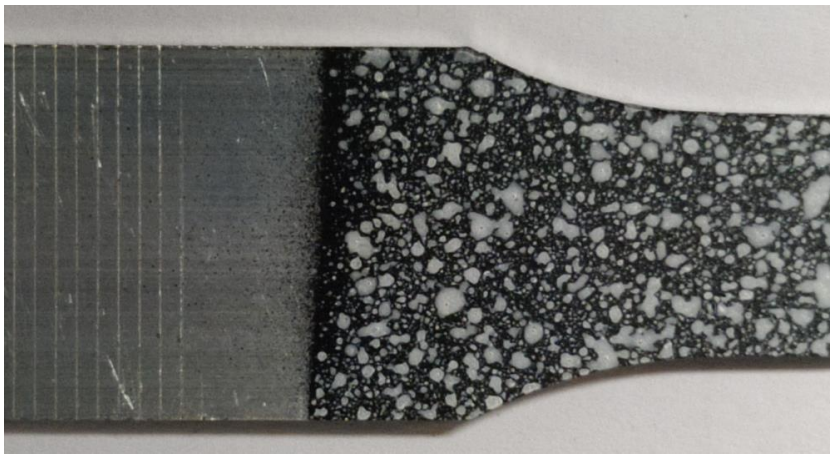

Figure 9: Detail of the speckled pattern painted on tensile specimens for DIC analysis.

In the QS tensile tests, DIC was used to measure global (50 mm around the centre of the specimen) and local (10 mm around the failure location) deformations, both in the longitudinal and transversal directions. An overview of the test setup can be seen in Figure 10.

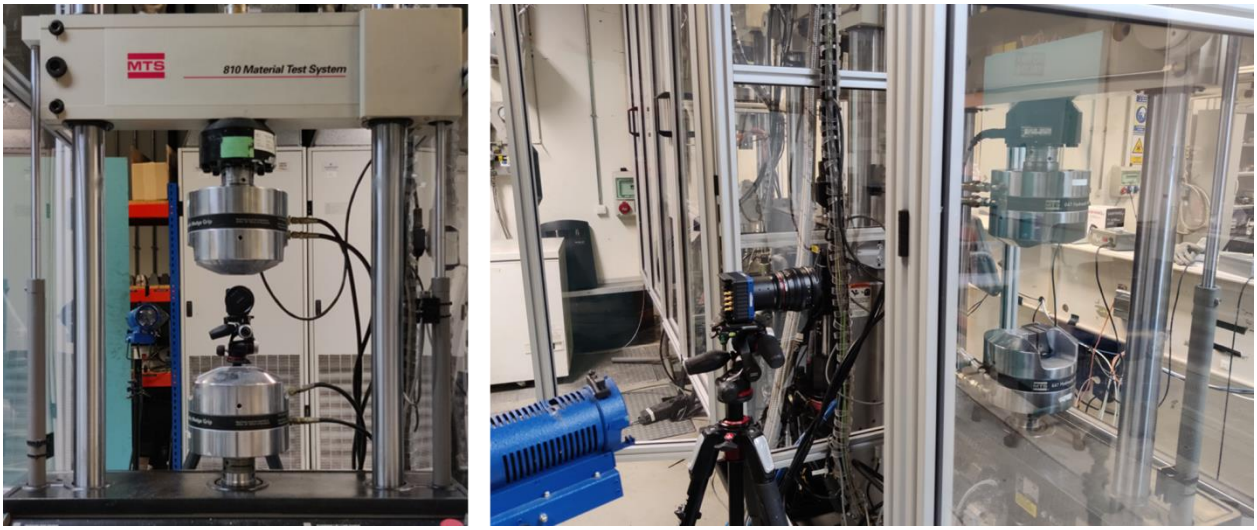

Figure 10: Front (left) and side (right) view of the testing equipment used for the QS tests.

Once the QS tests were completed, the next step was to perform the dynamic tensile tests at several strain rates. To this end, a shorter specimen was chosen, according to the specifications of the standard ISO 8253 (specimen type 3) [4]. The dimensions of the specimen used are presented in Figure 11; thickness was kept at 2mm.

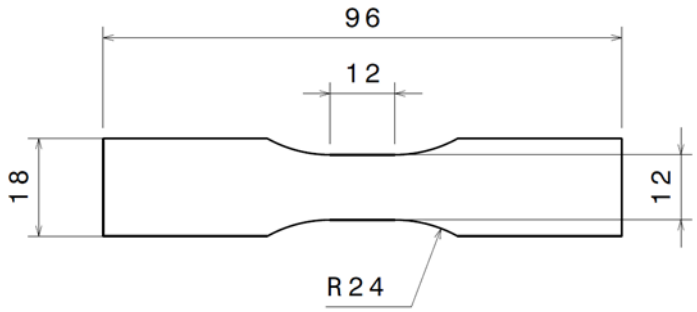

Figure 11: Specimen dimensions of the dynamic tensile test coupons as per ISO 8253.

Regarding the target strain rates (nominal values of 1, 10 and 200 s^{-1}), they were measured taking as reference a global gauge length of 10 mm located in the centre of the specimen and in the longitudinal dimension of the coupons. At least five specimens were tested for each target strain rate. Table 2 summarizes the relationship between the targeted strain rate and the displacement speed of the machine actuator that has to be applied.

Table 2: Target strain rates and resulting displacement speeds to be applied.

Strain rate	Displacement speed
1 s^{-1}	20 mm/s
10 s^{-1}	200 mm/s
200 s^{-1}	4 m/s

For these tests, a different testing machine was needed, as it has to able to introduce the loads needed to execute the test at much higher speeds (compared with the QS scenario), while at the same time ensure a reliable measurement of the test variables. The test equipment and setup employed for the dynamic tensile tests is shown in Figure 12.

Figure 12: Front (left) and side (right) view of the testing equipment used for the dynamic tensile tests.

Analogously, in the dynamic tests DIC was employed for the same purposes as in the QS scenario.

3.3.2 TEST RESULTS

Quasi-static tensile tests

The results of the QS tensile tests are presented in Figure 13. The aspect of the samples after the test is shown in Figure 14.

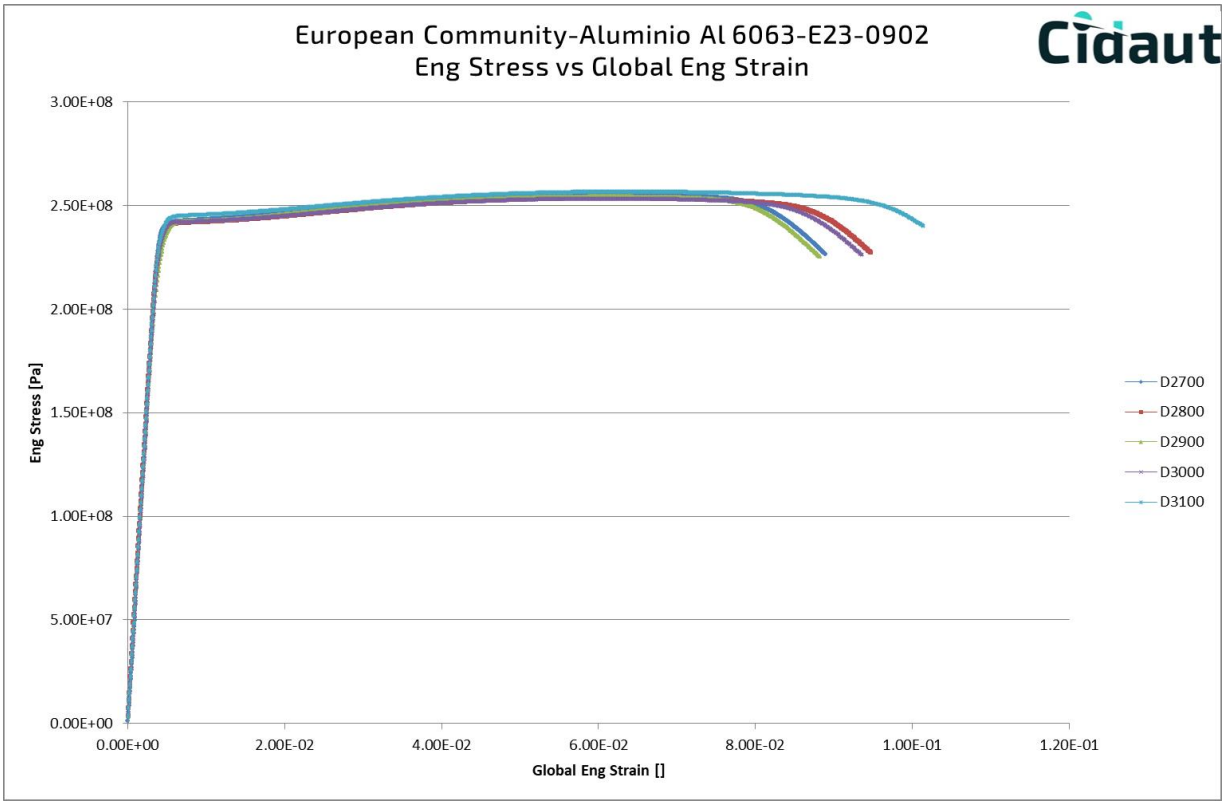

Figure 13: Stress-strain curves of the QS tensile samples.

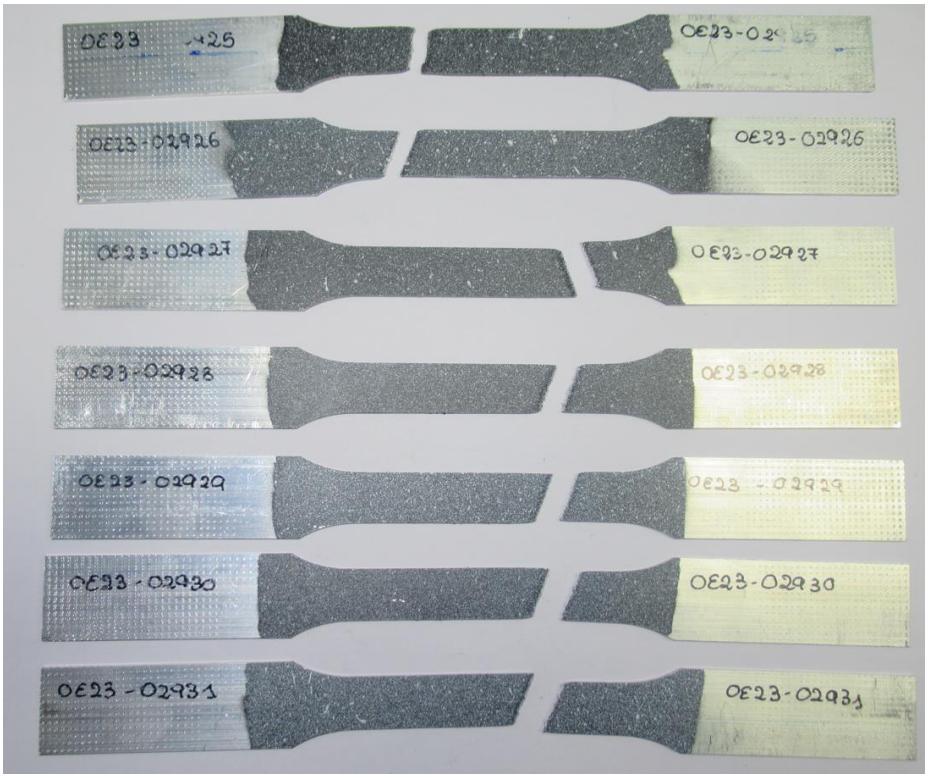

Figure 14: Specimens after execution of QS tensile test as per ASTM E8

In Figure 15, the failure area of one of the specimens is shown, in which it can be seen that in a very advanced stage of the test (immediately before failure), there is a certain amount of lateral displacement appearing in the material, due to the stress concentration effect.

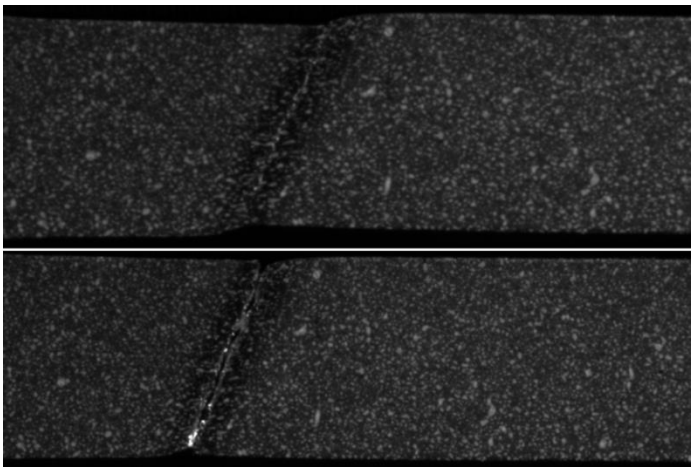

Figure 15: Detail of the failure of the QS tensile coupons. Top: frame before full breakage. Bottom: frame after full breakage

In general, a great repetitiveness across all samples was obtained, both in terms of performance (yield strength, ultimate strength, strain rate, Young modulus, etc.) and failure mechanism observed. There is a slightly higher dispersion on the failure strains, albeit it is within the usual values for this kind of materials. All samples present a brittle failure mode, without any significant development of necking during the tests. The evolution of stress/strain is quite homogeneous during the test until the latest stages of the test, in which a strain concentration appears in the failure zone. This strain evolution can be clearly seen in Figure 16 below, in which full field strain measurements are presented corresponding to an early, intermediate and late stage of the tests. The global gauge length of 50mm is also included in the pictures to ease the interpretation of the results.

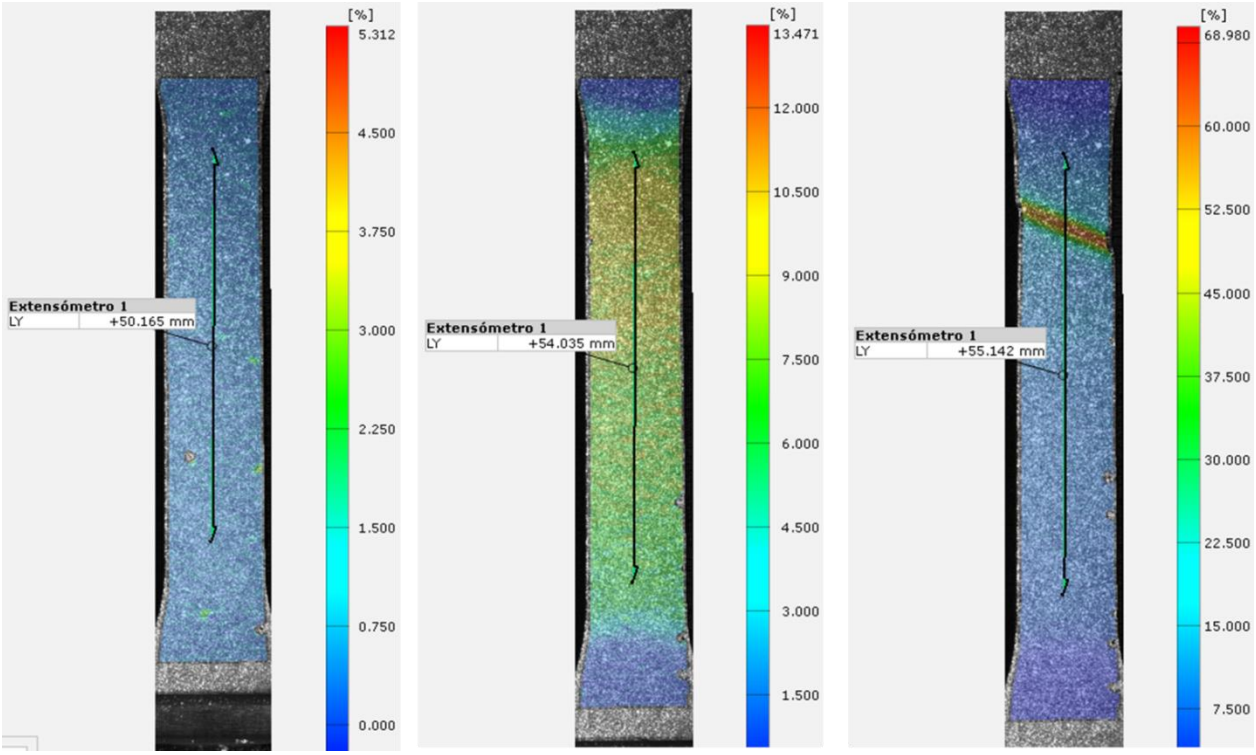

Figure 16: Strain fields measured during QS tensile test. Left: early stage; Centre: intermediate stage; Right: stage right before failure

Dynamic tensile tests

The results of the dynamic tensile tests are presented in Figure 17. The aspect of one representative sample of each strain rate tested is presented as example in Figure 18. The results are presented in an aggregated manner for the three tested velocities ($1s^{-1}$, $10s^{-1}$ and $200s^{-1}$) to ease the comparison and the assessment of results.

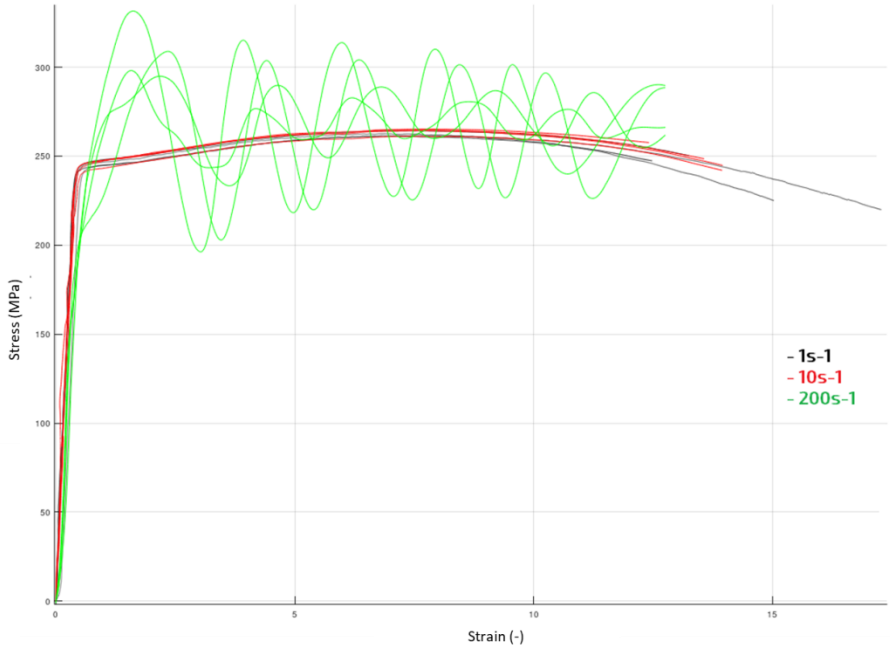

Figure 17: Comparative results of the dynamic tensile tests performed on Al6063 coupons.

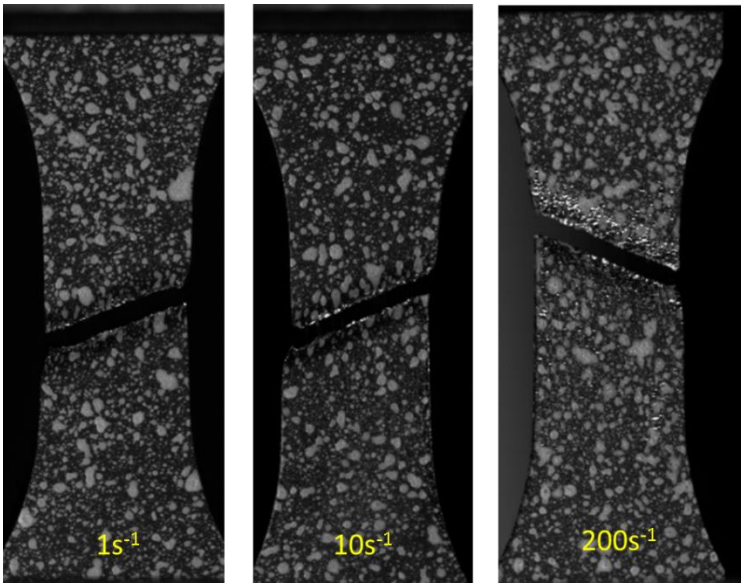

Figure 18: Examples of coupons after failure tested at several strain rates.

Looking at the figure above, it can be concluded that failure is hardly influenced by the strain rate at which the test is conducted; being it in all cases a brittle fracture. It is worth remarking that the area of the coupon affected by the failure is greater in the coupons tested at the highest strain rates (white marks on the speckled pattern appear), what is probably associated to the highest energy put in place in this configuration.

Despite it being subjected to an extrusion process that causes grain orientation, it is observed in Figure 17 that the Al6063 alloy presents only mild sensitivity to strain rate. Theoretically, materials tend to become stiffer and less deformable when the strain rate increases. Nevertheless, aluminium has traditionally been considered a material with low strain rate sensitivity below $1000s^{-1}$. Besides, it has been reported in literature that post-processing of Al alloys by means of heat treating or cold working can decrease even more the strain rate sensitivity [5], as happens in this case (a T6 heat treatment was applied after extrusion). Accordingly, examples can be found in literature of other wrought alloys showing little or no sensitivity to strain rate at moderate values in the 5xxx and 7xxx series [6], and even also for the Al6063 alloy [7]. Thus, the results obtained here are considered perfectly in line with the current state of the art on the subject.

Finally, it has to be remarked that the force (and consequently stress) measurements at the highest strain rate present a noticeable oscillatory behaviour because of the appearance of resonance effects in the system at the frequency range of this test. This is due to the fact that no physical extensometers were employed in these tests, and while it is not considered critical in the sense that it does not entail any significant impact on the interpretation and use of the results, a post-processing (filtering + smoothing) stage is needed to increase the quality of the data.

3.4 MINI-TENSILE TEST (ANISOTROPY EVALUATION)

3.4.1 TEST PROCEDURE

The anisotropy that is induced in the material during the extrusion process designed and carried out at ASAS was characterized by means of an additional set of tensile tests. In this batch of tests, samples extracted from extruded profiles at 0º, 45º and 90º with respect to the direction of extrusion were tested in a QS test setup at RT using mini-tensile specimens, identical to the ones employed for the dynamic tensile tests (see Figure 11). Further details about the test setup and main testing parameters can be found in previous section 3.3.1.

3.4.2 TEST RESULTS

In Figure 19 the results (stress-strain graphs) for the three orientations are presented in an aggregate manner to ease their interpretations, while in Figure 20 the aspect of the coupons after failure is shown, also for all orientations.

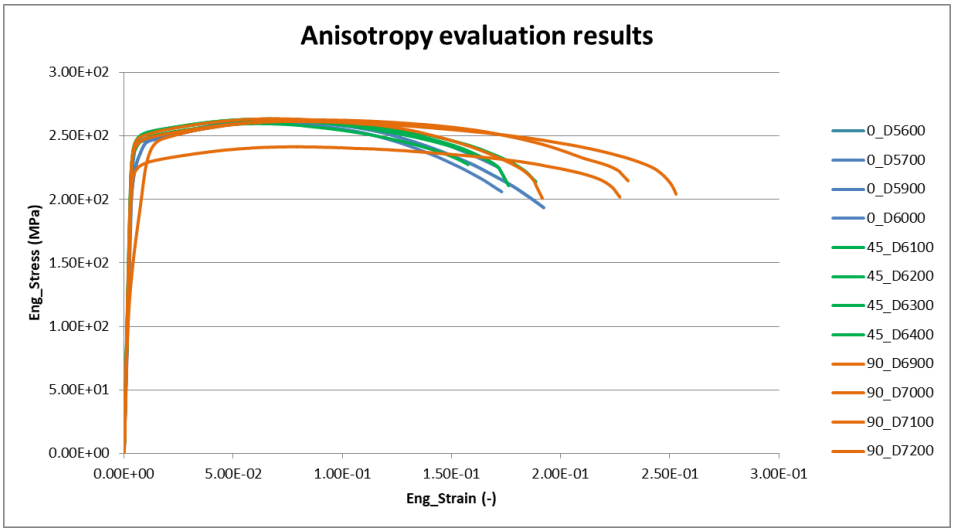

Figure 19: Anisotropy evaluation results for the Al6063

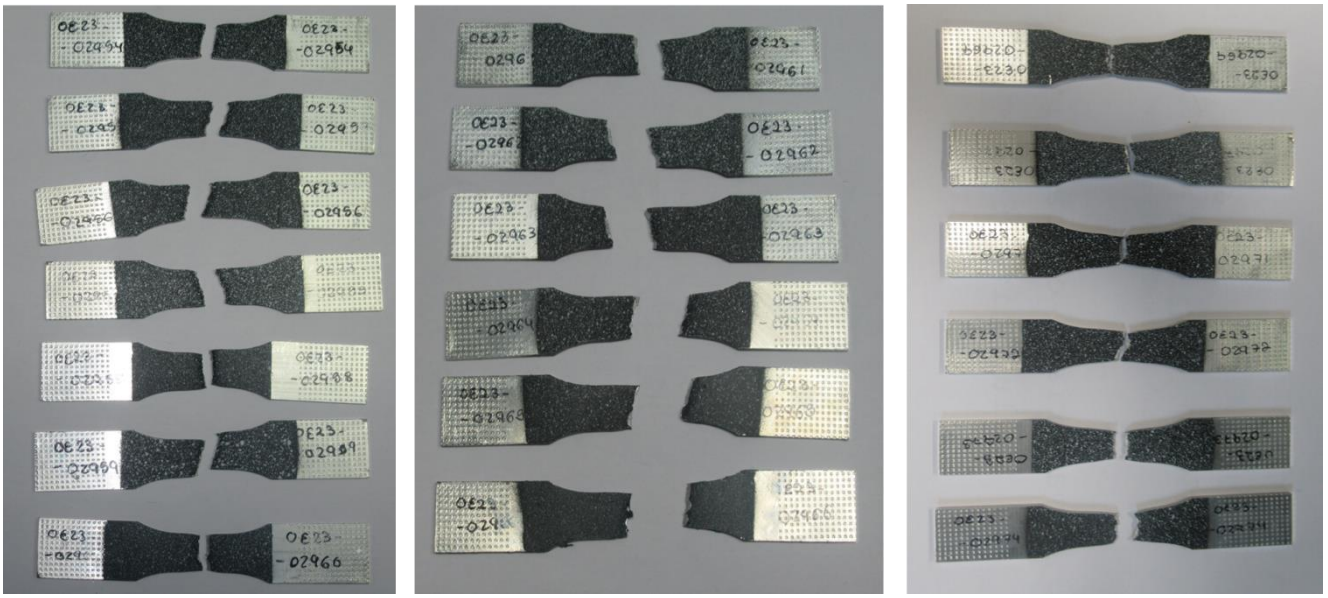

Figure 20: Specimens after QS mini-tensile test. Left: 0º coupons; Center: 45º coupons; Right: 90º coupons.

The measured values of stress and strain for all tested coupons (4 valid results per each material orientation) show that there are no strong signs of anisotropic behaviour in this material, even though it has been subjected to an extrusion process. If there is any anisotropy, it cannot be clearly distinguished from the inherent scattering of the coupons tested, in terms of Young modulus, yield strength and ultimate strength. This is aligned with the observations made at microstructural scale, reported in section 3.2.1, in which it was seen that the same grain structure appears after failure regardless of the orientation of the material. Apparently there are some differences in the strain registered in the 90º coupons (in three out of four coupons), that reach higher ultimate strains than the other coupons from 0º and 45º orientations, and also the stress drop prior to failure appears at higher strains. This might be related to the failure mode appearing in the coupons (Figure 20).

Looking at the failure modes of the coupons (Figure 20), it is remarked that the failure mechanisms are to some extent influenced by the orientation of the material. Coupons at 0º present a brittle failure mode at macroscopic scale in most cases, less evident than that of the thicker specimens (Figure 14) because of the different coupon geometry employed. In the 45º coupons, a transition is observed, in which there is still a predominance of the brittle failure mode, but failure surfaces are not as sharp as in the 0º coupons. Finally, the failure mode is different for the 90º coupons. Signs of ductile failure mechanisms can be seen in many of the samples, and also there is a higher amount of necking, although still limited, if compared to the other orientations.

3.5 BIAXIAL TEST

3.5.1 TEST PROCEDURE

Similarly to the case of the QS tensile test, biaxial testing of aluminium samples at room temperature and QS velocity was performed using a tensile test setup, based on the specifications of ASTM E8, therefore the procedure and equipment is essentially the same explained in section 3.3.1 for the QS tensile tests and will not be repeated here for conciseness. DIC is also used to measure the strain fields throughout the tests.

In this case, the biaxial stress state is induced in the coupons by means of the geometry of the coupons, not by introducing pure biaxial loads as in the tensile test. A notch is machined on the coupons (Figure 21), so that during the development of the test, longitudinal and transverse loads are induced in a concentrated region of the specimen between the two notches, that corresponds to biaxial-like stress states (target triaxiality around 0.5-0.66). Hence, in this test the coupon has a non-standard geometry, defined specifically for the purposes of this test based on the wide experience of IDI and VIF in the testing of materials for material card development purposes.

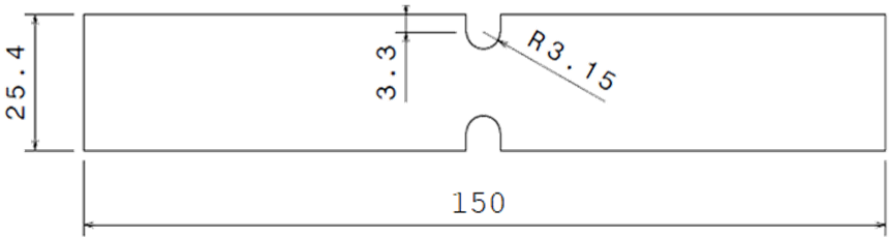

Figure 21: Dimensions of the biaxial test coupons – non-standard geometry.

3.5.2 TEST RESULTS

The results of the QS tensile tests are presented in Figure 22. The aspect of the samples after the test is shown in Figure 23.

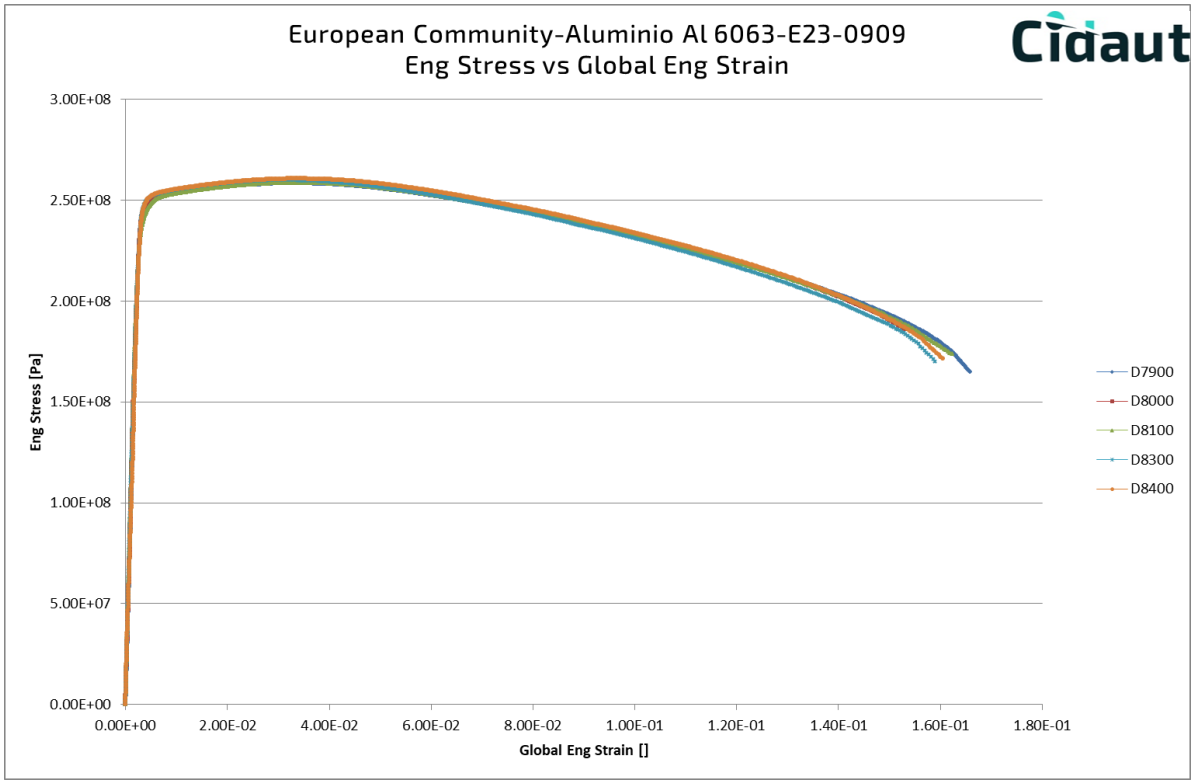

Figure 22. Stress-strain curves of the QS biaxial samples.

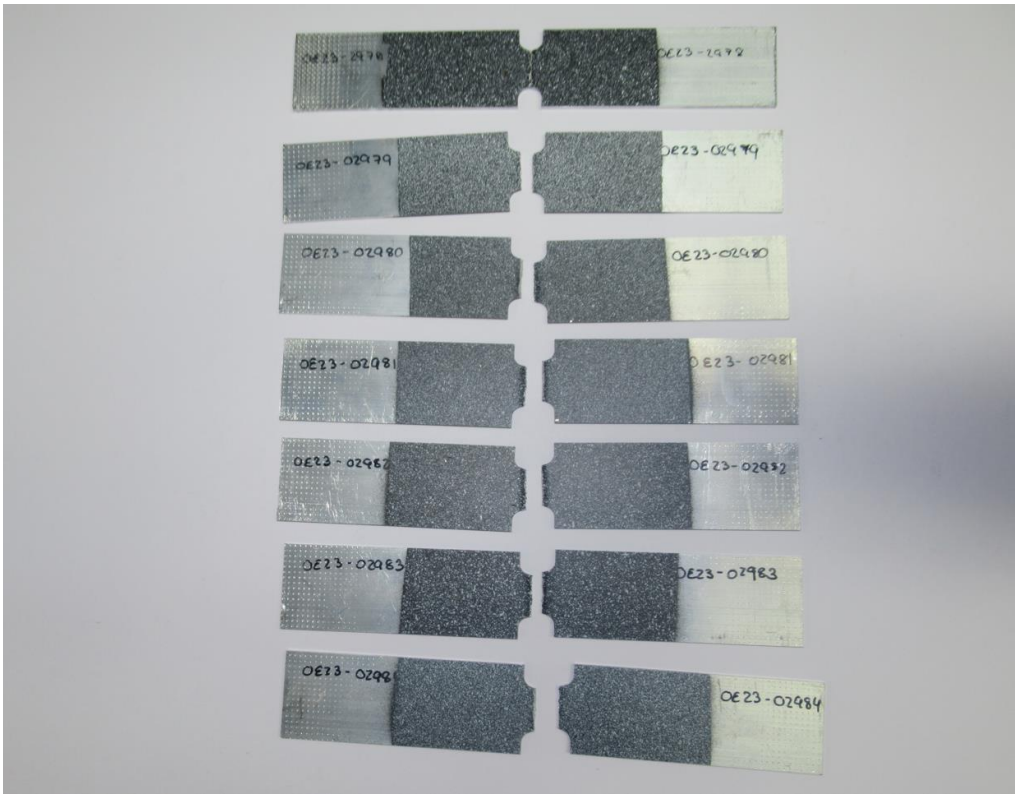

Figure 23: Specimens after execution of QS biaxial test based on ASTM E8

Excellent repetitiveness was achieved during the tests in all considered variables (global strain, stress and failure mode). Failure mechanisms found as expected for this geometry design, proving the appropriateness of the design employed for this test. A detail of the failure region of a sample is depicted in Figure 24.

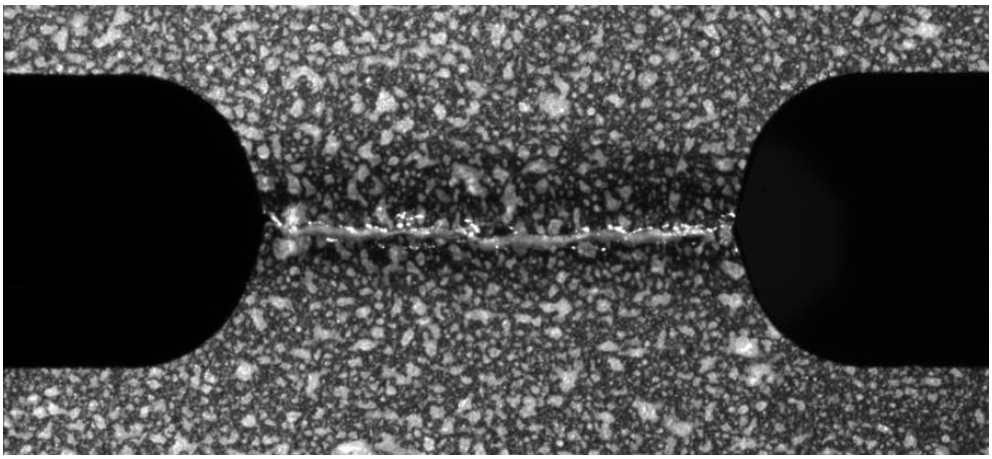

Figure 24: Detail of the failure area of a biaxial specimen.

DIC was also used in this test configuration. In Figure 25 it can be seen that deformation during the test is mostly concentrated in the coupon area between the notches, while the rest of the coupon is essentially unaltered, what proves additionally the validity of the design. At late stages of the tests, the central area of the coupons becomes so deformed that is difficult for the system to track deformations with sub-pixel accuracy (Figure 25, right).

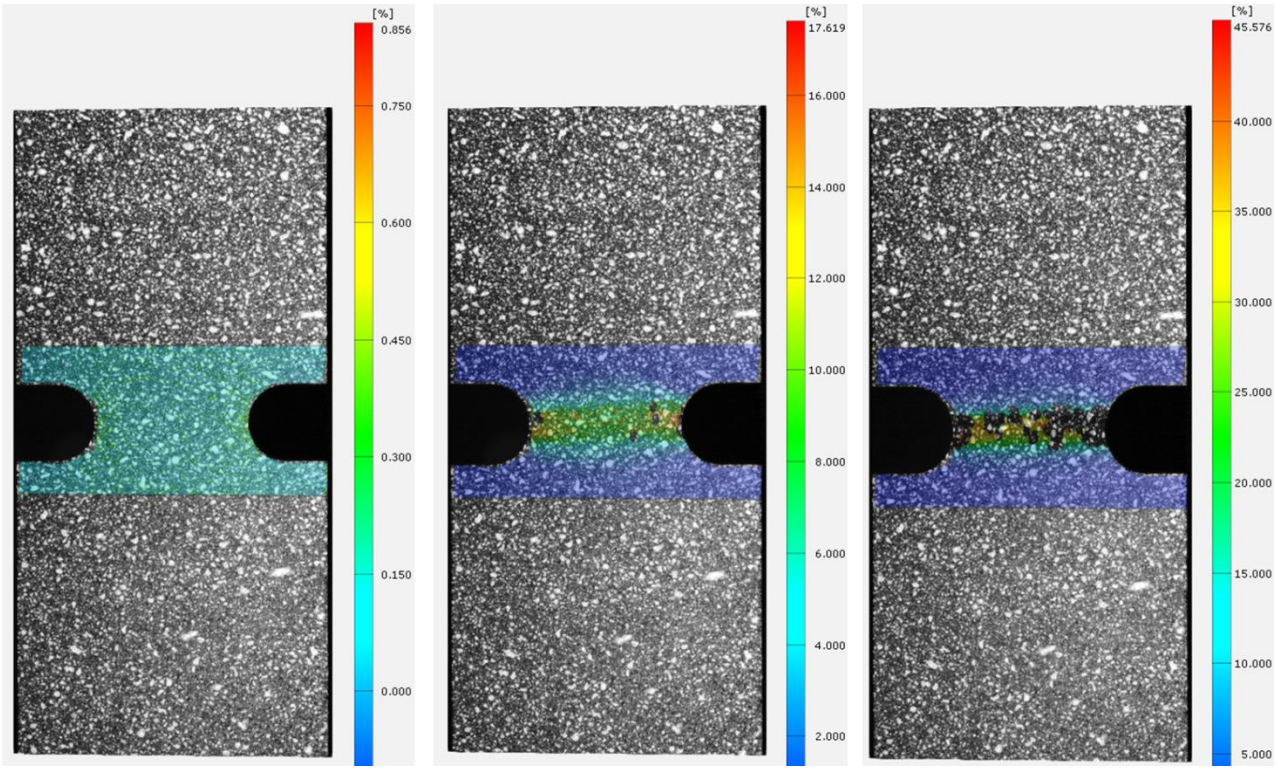

Figure 25: Strain fields measured during QS biaxial test. Left: early stage; Centre: intermediate stage; Right: stage close to failure.

Several different virtual extensometers were placed in the DIC analysis software to keep track of global (longitudinal and transversal) as well as local deformations with different reference lengths. Some of the extensometers used for the analysis are shown in Figure 26.

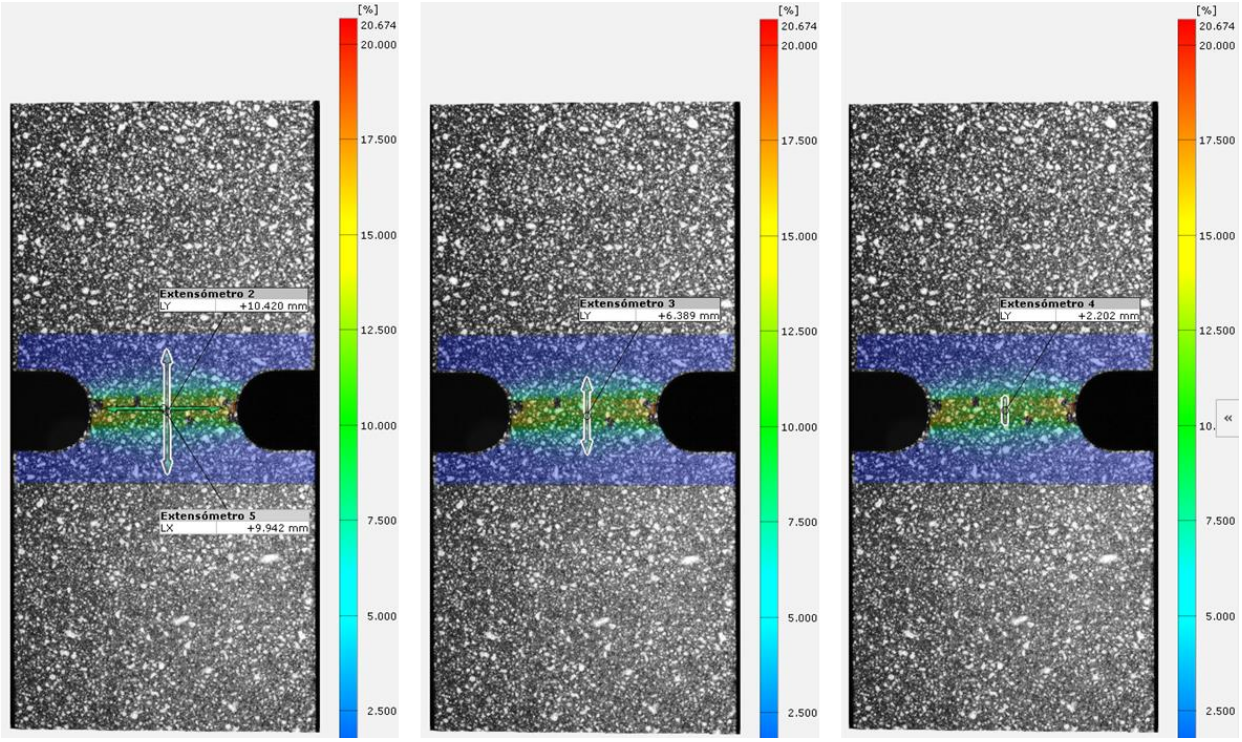

Figure 26: Global and local extensometers to monitor deformation during biaxial test

3.6 SHEAR TEST

3.6.1 TEST PROCEDURE

The planning and design of the shear tests follows the same logic as the previous biaxial test. Again, the setup and test boundary conditions are the same as in the QS tensile and QS biaxial tests and are based on the standard ASTM E8. Analogously, the (approximately pure) shear stress state is induced on the coupons thanks to their geometry (Figure 27), although the test itself is executed as if it was a tensile setup. In this case, an ad-hoc slot is machined on the coupons, so that when the specimen is deformed during the test, a shear stress state (target triaxiality around 0-0.15) develops in the small area between the slots ends (5 mm region).

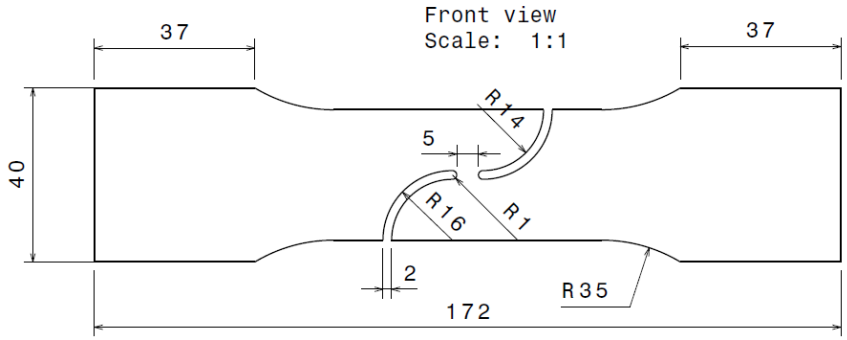

Figure 27: Dimensions of the shear test coupons – non-standard geometry.

Hence, in this test the coupon has a non-standard geometry, defined specifically for the purposes of this test based on the wide experience of IDI and VIF in the testing of materials for material card development purposes.

3.6.2 TEST RESULTS

The results of the QS shear tests are presented in Figure 28. The aspect of the samples after the test is shown in Figure 29.

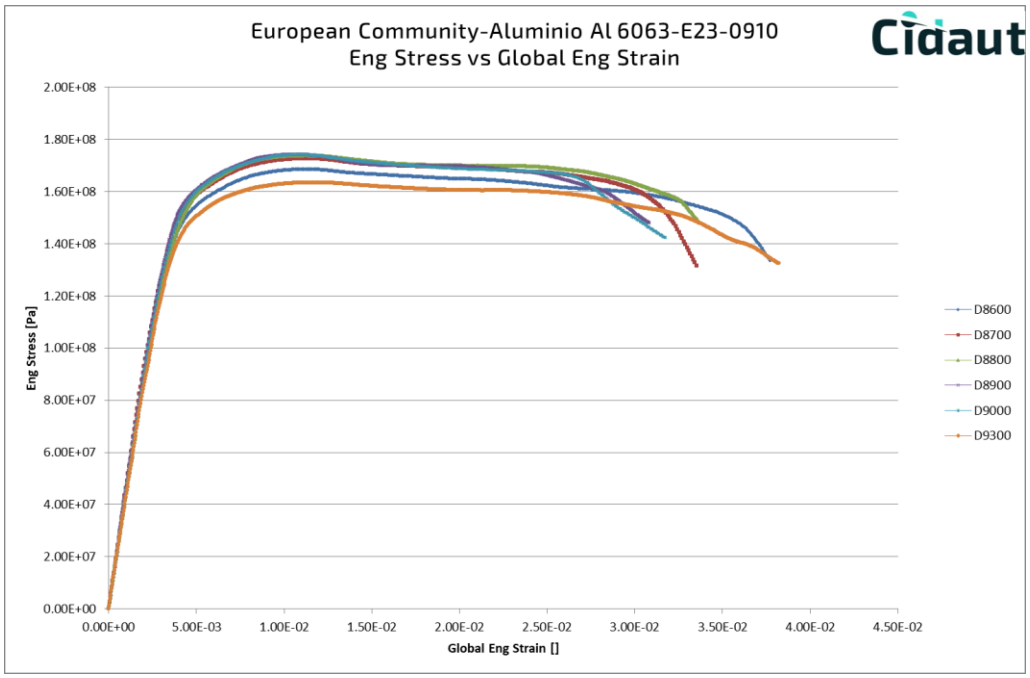

Figure 28: Stress-strain curves of the QS shear samples.

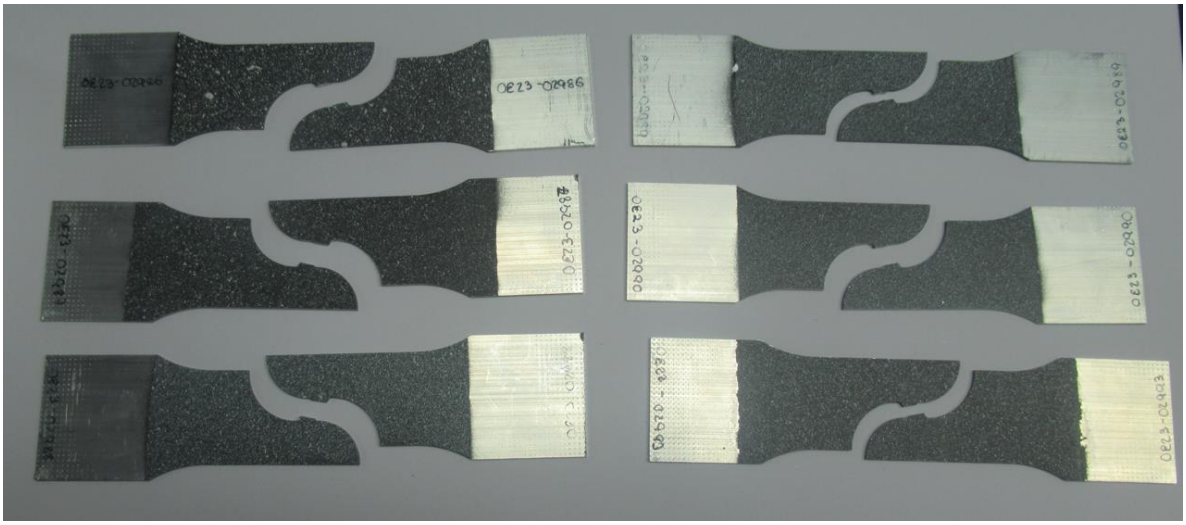

Figure 29: Specimens after execution of QS shear test based on ASTM E8.

Compared to the other QS tests, the shear test presents the highest dispersion, although in any case the repetitiveness is good and consistent behavior is found across all samples. Due to the shear failure mechanisms, it is difficult to define precisely the instant in which specimens fail, that explains the dispersion in failure strains that can be seen in Figure 28. A detailed picture of the failure area is shown in Figure 30, in which the shear deformations can be clearly seen on the speckled pattern.

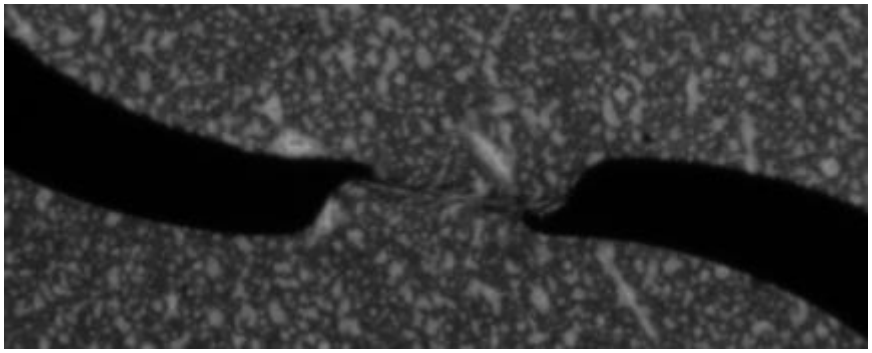

Figure 30: Detail of the failure area of a QS shear coupon.

DIC was also used to track full-field deformations during the tests (Figure 31). At advanced stages of the test, the most deformed areas of the coupon were lost; nevertheless global deformations can be successfully tracked throughout the whole duration of the tests as demonstrated in Figure 32.

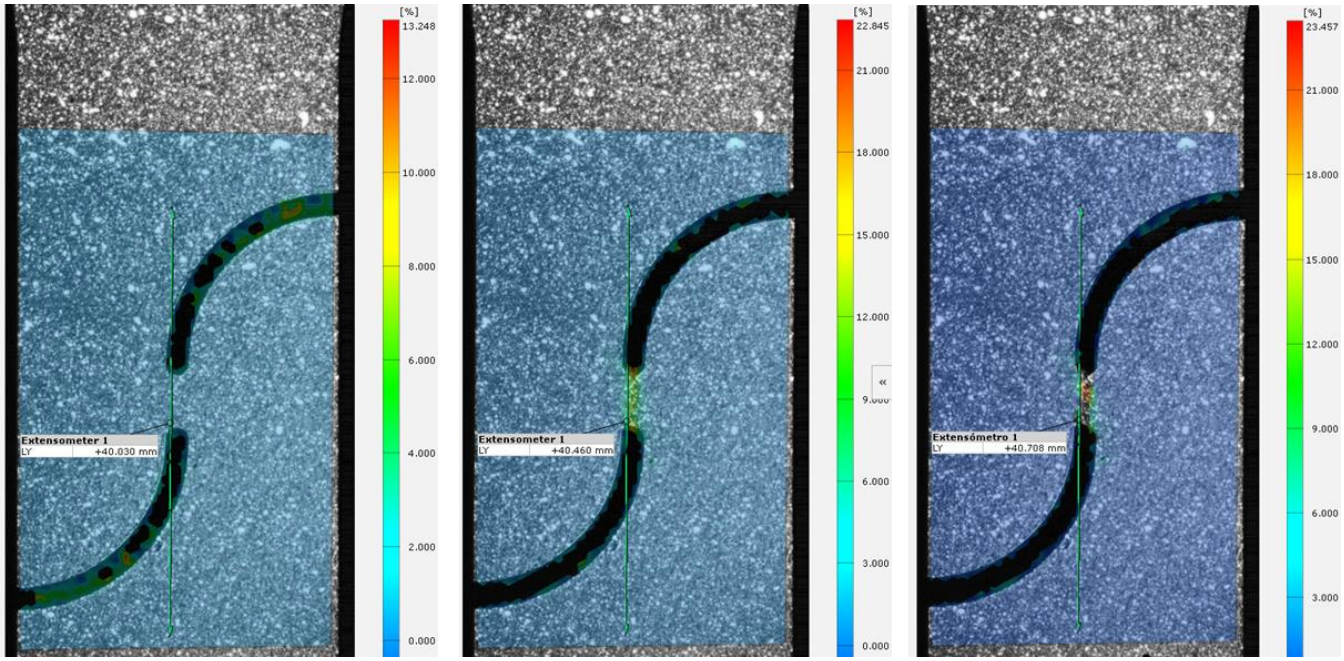

Figure 31: Strain fields measured during QS shear test. Left: early stage; Centre: intermediate stage; Right: stage close to failure.

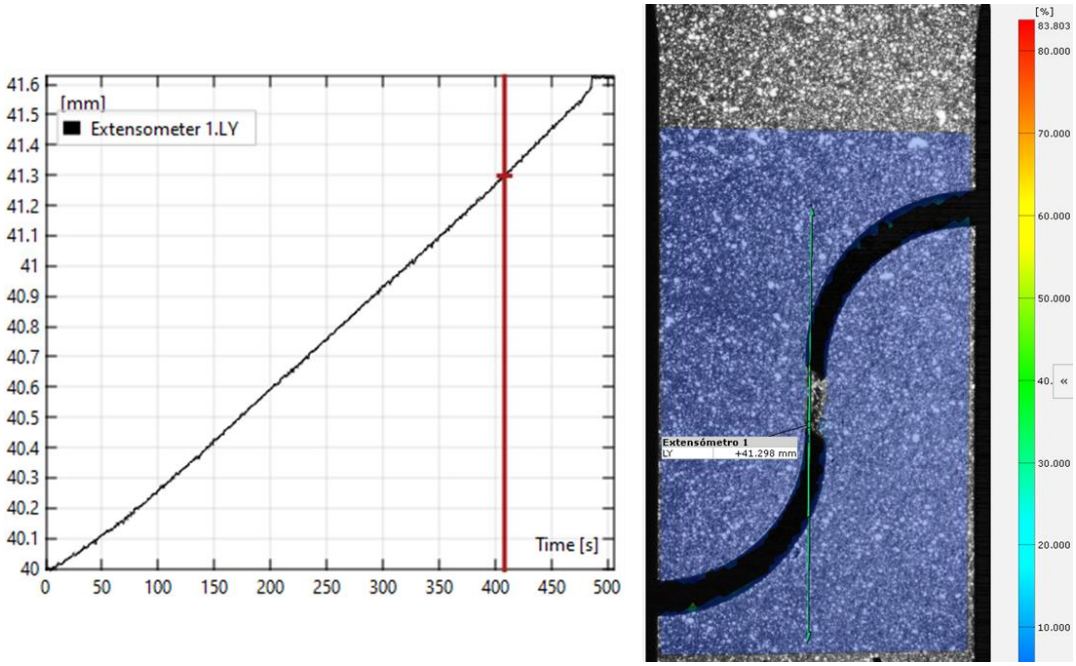

Figure 32: Tracking of global deformation on shear specimens after full-field signal is lost.

3.7 THREE POINT BENDING TEST

3.7.1 TEST PROCEDURE

Three point bending testing of aluminium samples at room temperature and QS velocity was performed according to the prescriptions of the standard ASTM D790 [8], using a standard coupon geometry of 2mm thickness (Figure 33)

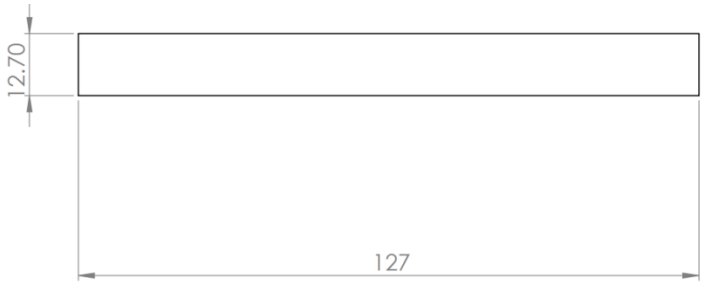

Figure 33: Dimensions of the three point bending coupons as per ASTM D790.

In the setup, the distance between supports was derived using the 16:1 relationship recommended by the standard; therefore this parameter was fixed at 32mm.

3.7.2 TEST RESULTS

The stress-strain results of the three point bending tests are presented in Figure 34. The aspect of the samples after the test is shown in Figure 35. Great repetitiveness was found between the samples during the tests. No failure was reached. Due to the test setup employed (see 3.7.1), the maximum displacement allowed by the testing equipment is reached before failure occurs.

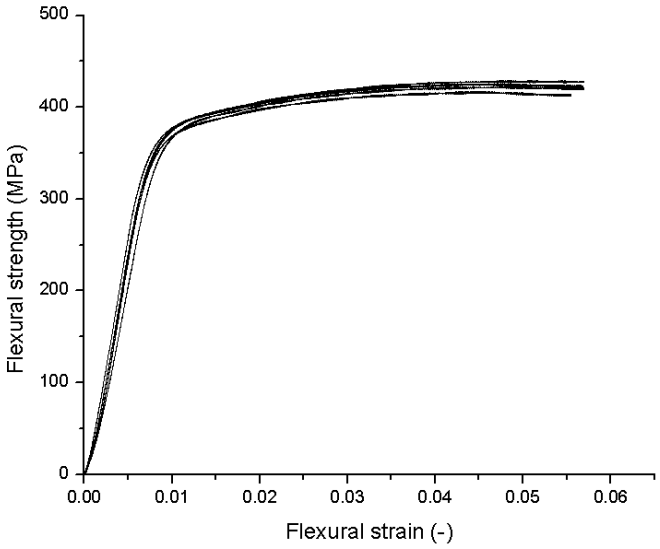

Figure 34: Stress-strain curves of the three point bending samples.

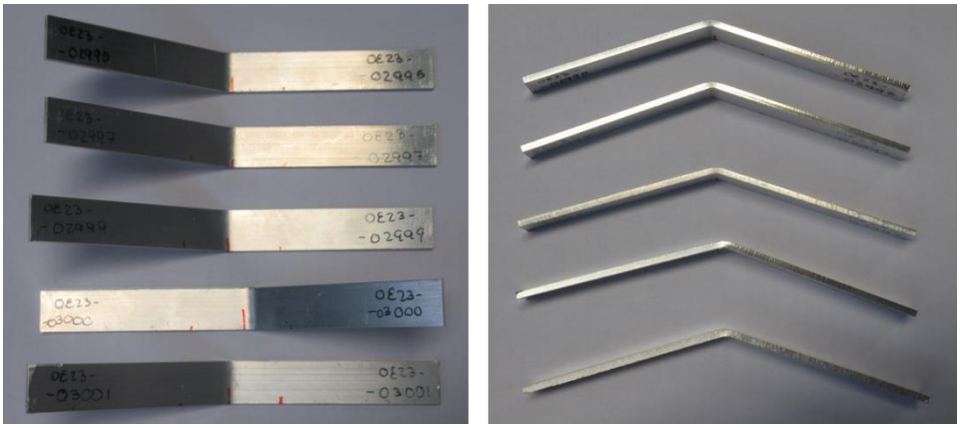

Figure 35: Specimens after execution of three point bending tests as per ASTM D790.

3.8 DISCUSSION ON TEST RESULTS

The results of the tests carried out on the Al 6063 alloy proved that the material has predictable and repetitive behaviour and failure mechanisms in any test condition as expected by the partners. Coupon geometries proposed worked well in every load case and test condition studied and therefore provided valuable insights about the behaviour of the material as well as high-quality data for the development of high-fidelity simulation models (material cards) proposed in Task 3.2 and described in D3.2.

The material presents low sensitivity to coupon orientation and strain rate, which is coherent with the available literature on the subject. The extrusion process does not have a severe impact on the material properties, and besides the application of a T6 heat treatment afterwards (see D3.1) mitigates most changes that may have been induced during the extrusion process, as seen in the microstructural characterization of the coupons after failure. From a purely technical point of view, it is recommended to use physical extensometers in further tests that may be performed at higher strain rates (≥ 200s^{-1}) using universal testing machines to avoid potential resonance effects that can affect the data collection process.

After this testing campaign, it is not identified any specific optimization need in the material formulation and/or in the testing procedures applied to it in order to enhance either its energy absorption capabilities or its microstructure.

4. TP-CFRP CHARACTERIZATION

The testing campaign designed for the TP/CFRP material developed by tPE aims at characterizing extensively the behaviour of the material at micro- and macroscales. As such, not only aspects related to the performance of the material in different static and/or dynamic load cases are characterized, but also different failure mechanisms and their implications at microstructural level are investigated through a variety of tests at coupon scale. Also, specific tests requested by IDI and VIF to get data needed to feed advanced material cards for simulation codes (LS-Dyna) have also been included.

The overall scope of the testing campaign for the TP/CFRP (PA6+48%CF) is summarized in Table 3. Specific lay-ups and thicknesses were produced according to the requirements of each test; details can be consulted in section 4.1. The procedures and results of each test can be found in the subsequent sections of this chapter as well.

Table 3: Overview of test campaign performed on the TP/CFRP material.

Test name	Scale	Goal
SEM	Micro	Characterize the microstructure of the material before and after failure
X-ray diffraction	Micro	Determine the aluminium's crystalline structure
SPM	Micro	Investigate the surface properties of the material
Scattering	Micro	Investigate the internal structure of the material
Static tensile	Macro	Test the behaviour of the material when subjected to tensile forces, at quasi-static velocity, at 0º and 90º orientations
Dynamic tensile	Macro	Test the behaviour of the material when subjected to dynamic tensile forces, at velocities higher than QS
Quasi-iso tensile	Macro	Test the behaviour of the material when subjected to tensile forces, in a quasi-isotropic lay-up [0º, +45º, -45º]
Compression	Macro	Test the behaviour of the material when subjected to compression forces, at 0º and 90º orientation
Bending	Macro	Test the behaviour of the material when subjected to flexural loads, for three different lay-ups
Compact tension/compression	Macro	Evaluate the translaminar fracture toughness under tensile/compression loads
Interlaminar failure	Macro	Evaluate interlaminar failure mechanisms (mode I, mode II)
Creep/stress relaxation	Macro	Characterize the long-term behaviour of the material
DMA	Micro	Evaluate dynamic properties of the material (frequency domain)

4.1 MANUFACTURING OF COUPONS

For the production of the TP/CFRP specimen material, layer structures were formed according to the specified configurations and the desired characteristic values to be determined.

Therefore, the following plate configurations (Table 4) were produced for the required tests:

Table 4: Required laminate structures

	Layup description	Thickness	Test name
Laminate ID #1	$[0]_{17}$	~ 2,5 mm	Quasi-static tensile test, quasi static compression test, 0°/90°orientation
Laminate ID #1	$[0]_4$	~ 0,5 mm	Dynamic tensile test, 0°/90°orientation
Laminate ID #2	$([0\|90]_4)_s$	~ 2,5 mm	Quasi static in-plane shear test, quasi static 3-point bending test
Laminate ID #2	(±45)	~ 2,5 mm	Quasi static 3-point bending test
Laminate ID #3	$([0\|90]_9)_s$	≥ 4,5 mm	Compact tension test, compact compression test
Laminate ID #4	$([0\|45\|-45\|90]_s)_2$	~ 2,5 mm	Quasi-isotropic tensile test, quasi-isotropic 3-point bending test
Laminate ID #5	$([0]_{10}\|PTFE\|[0]_{10})$	~ 3 mm	Interlaminar failure modes

The UD tape based on PA6 and carbon fibers, which was available on a roll, was manually assembled according to the dimensions of the plate mold used and the required fiber orientation.

The stacks were formed directly in the plate mold with a circumferential dipping edge just before consolidation, as shown in Figure 36.

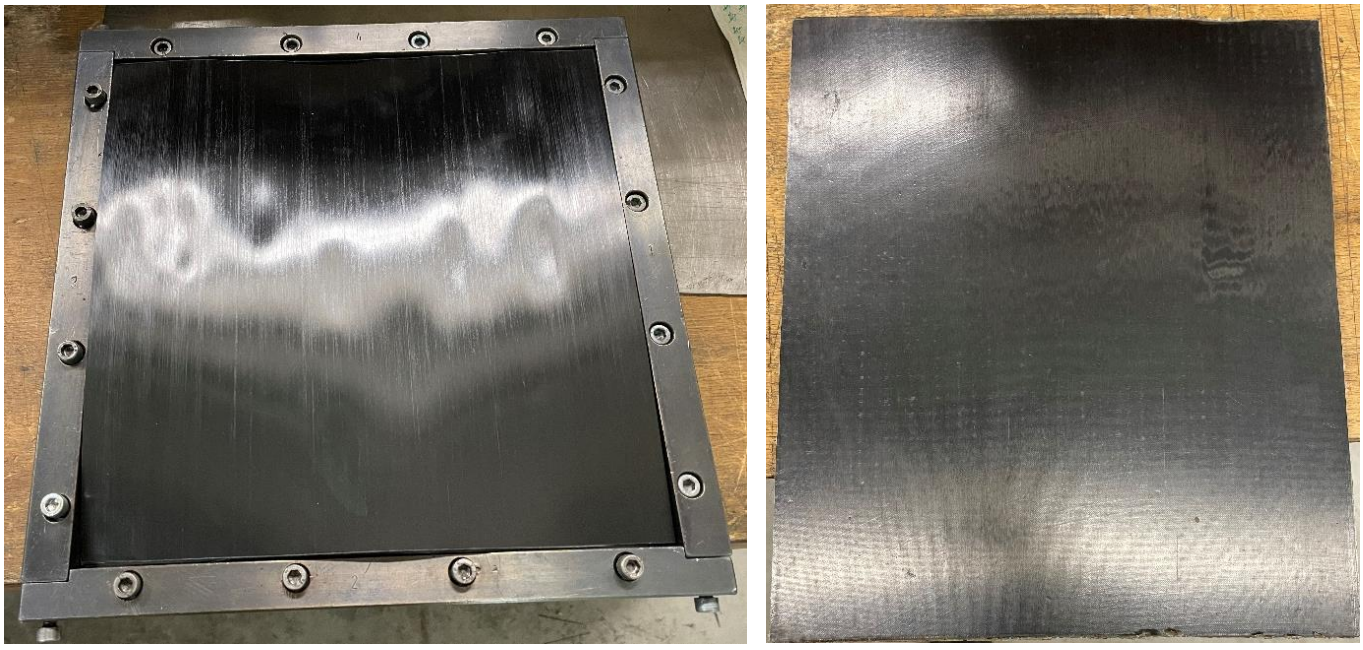

Figure 36: Laminate board before (left) and after (right) consolidation

The plates with dimensions of 260 mm x 260 mm were produced variothermally on a Collin press of type P 300 P/M. The heating program used, is shown in the following Table 5.

Table 5: Heating program used in the press

Step no.	1	2	3	4	5
Duration [sec]	1	60	500	400	1000
Temperature	180	180	255	255	50
Heating rate [K/min]	0	0	20	0	20
Pressure [bar]	0	5	20	30	40

The plates were tempered above the melt temperature at 255 °C, held at this temperature for approximately 7 min and then cooled down to 50 °C in the mold. The entire cycle per plate required a total of approximately 33 min. Afterwards the plates were demolded, subsequently trimmed with a tile cutting machine and fed to the further specimen preparation.

The specimens were removed from the sheets using a Datron Next milling machine to avoid possible crack initiation points, which can occur with other methods (e.g. abrasive water jet cutting) and reduce the mechanical properties. Figure 37 below shows the milling process and the finished panel for the ID #4 laminates.

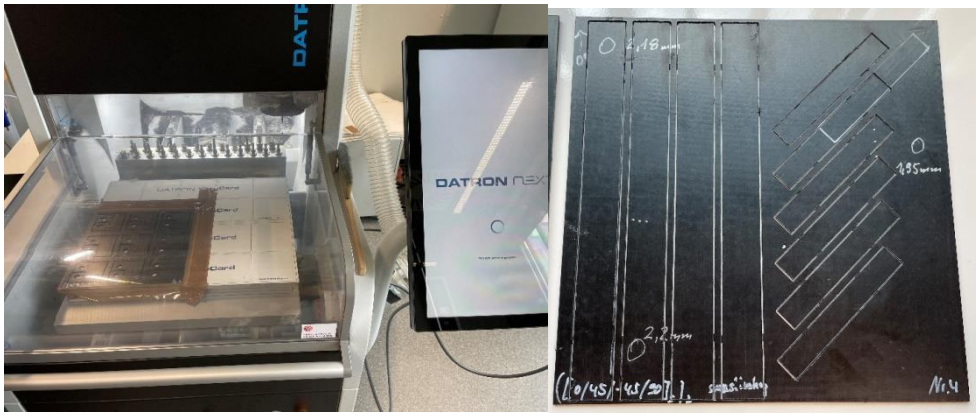

Figure 37: Milling machine during process (left) and milling layout for laminate ID #4 (right)

After the specimens were cut out except for a small remaining material ridge, they were manually detached from the plates and still finally deburred.

Figure 38: Test specimens for a variety of relevant tests

Once completed, the samples were appropriately labelled (see Figure 38) and sent to the project partners for characterization. Further details about the design and manufacturing of the TP/CFRP can be found in D3.1, here only a brief description is provided focusing on the close relationship existing between material manufacturing (T3.1) and material characterization (T3.2).

4.2 MICROSTRUCTURAL CHARACTERIZATION

4.2.1 MICROSTRUCTURAL AND FRACTOGRAPHY CHARACTERIZATION

The fractography analysis of TP/CFRP was conducted by UNN, utilising the SEM with an accelerating voltage ranging from 10 to 20 kV, and the magnification was adjusted according to the specific conditions to reveal detail morphology. Prior to imaging, a platinum coating was applied to the surface of sample to enhance image clarity as the TP/CFRP shows electro-charging effect. Figure 39 presents the fracture morphology of TP/CFRP subjected to a quasi-static tensile loading. It highlights the failure mode based on the orientation of the fibres in relation to the loading direction. These images unveil the heterogeneous nature of TP/CFRP composites when observed at a macroscopic scale, and composites were broken with many breaking and separation of carbon fibres. When the fibre orientation is perpendicular to the loading axis, as seen from one example in Figure 39(a), two combined modes of failure become evident: fibre breakage and separation (debonding). On the other hand, Figure 39(b) and 36(c) depict the fractography of samples with a fibre orientation tested at 150 degrees. In this case, the sample exhibits two distinct failure zones, i.e., the first one perpendicular to the loading direction and the second one parallel to the loading axis, as indicated in Figure 39(b) and 36(c), respectively. These damage zones exhibit various internal material failures, such as fibre breakage, fibre separation, and tape delamination. These observations suggest the presence of weak bonding between the tape layers during the manufacturing process.

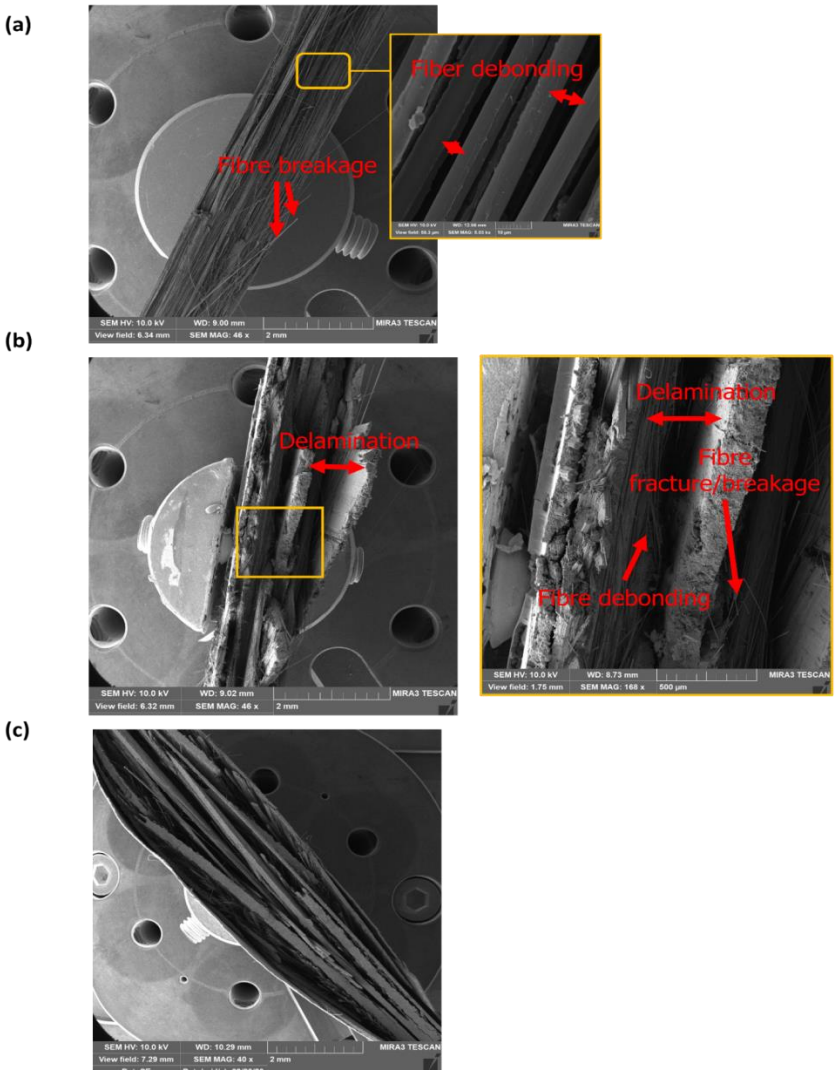

Figure 39: SEM for the fracture surface of the TP/CFRP under QS tensile test, (a) fiber orientation is 90◦, (b) fiber orientation is 150◦, 1st breakage, and (c) fiber orientation is 150◦, 2nd breakage.

4.2.2 STRUCTURE AND SURFACE CHARACTERIZATIONS

UNN further investigated the structural and surface characteristics of the as-received TP/CFRP obtained from CID, with some of the examples of the test findings illustrated in Figure 40(a) displays the XRD profile of the TP/CFRP sample, revealing distinctive diffraction peaks corresponding to PA6 α phase's (200) and α (002) peaks at approximately 2θ = 20.23° and 23.37°, respectively. These peaks confirm the monoclinic crystalline structure of PA6, which has a melting point of approximately 224±1.5°C [9]. An additional peak, situated around 26°, represents the (002) peak of graphite, a characteristic feature of numerous carbon-based products with varying degrees of basal plane alignment [10]. In our examined sample, this peak is attributed to the presence of carbon fibres (CFs) and appears at 45.2°.

The optical scattering test was carried out by employing a laser interferometer at Northumbria University, UK, and one of the example outcomes are presented in Figure 40(b). The laser interferometer generated an optical scattering effect, morphology features, and roughness profile that exhibited concave-convex structures in multiple directions, indicating that the TP/CFRP surface possesses a maximum roughness value of approximately 24 micrometres.

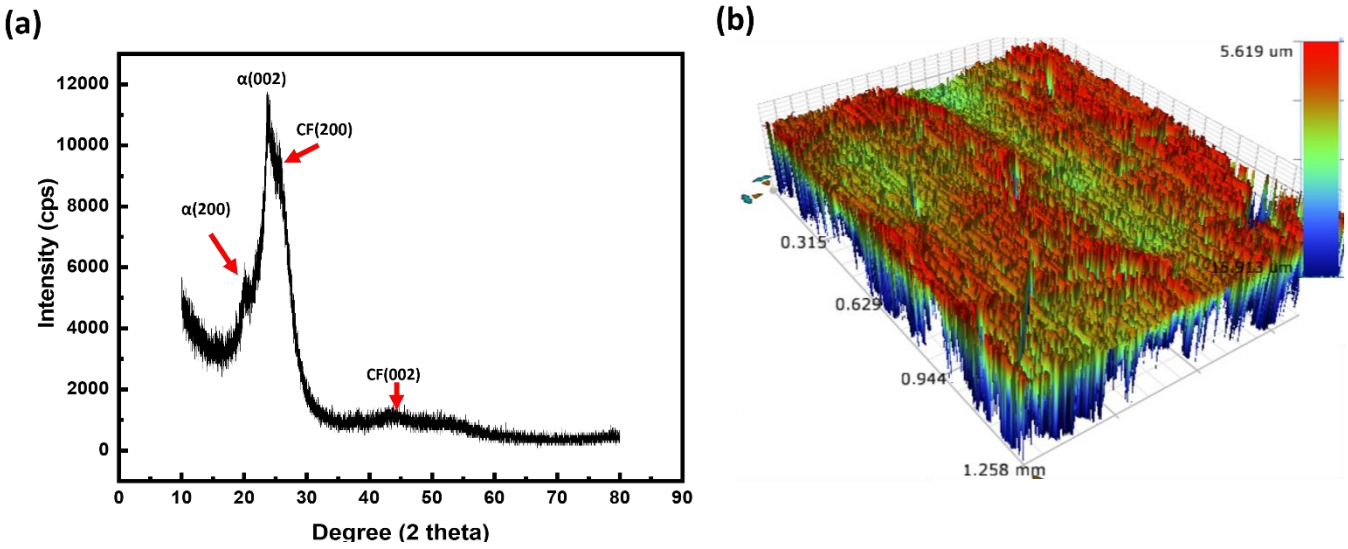

Figure 40. TP-CFRP Structural and surface characterizations results, (a) X-ray diffraction profile, and (b) Scattering by laser interferometer.

DMA test results for the TP/CFRP offer valuable insights into its damping properties and storage modulus. The selected examples of DMA test results are displayed in Figure 41. Specimen of 10 * 2 mm^2 with thickness of 0.5 mm from 4-plies laminate all at zero orientation and 48% CF composition was used. Testing was performed with constant test parameters, including a heating rate of 1 °C/min, temperature range of 35 - 215°C, and frequency of 1 Hz. The test was performed under a tensile loading and the test setup is provided in Figure 41(a). The glass transition temperature (T_g) of composites is taken by the maximum of tanδ, which implies a relaxation process and involves the extent of the mobility of small molecular groups and macromolecular chain segments. As one fo the examples presented in Figure 41(b), the T_g of the TP/CFRP is around 85°C. The storage modulus reflects the material's stiffness and its ability to store elastic energy. A higher storage modulus suggests a larger stiffness and resilience. As depicted in Figure 41(c), the storage modulus decreases with the increase of testing temperature.

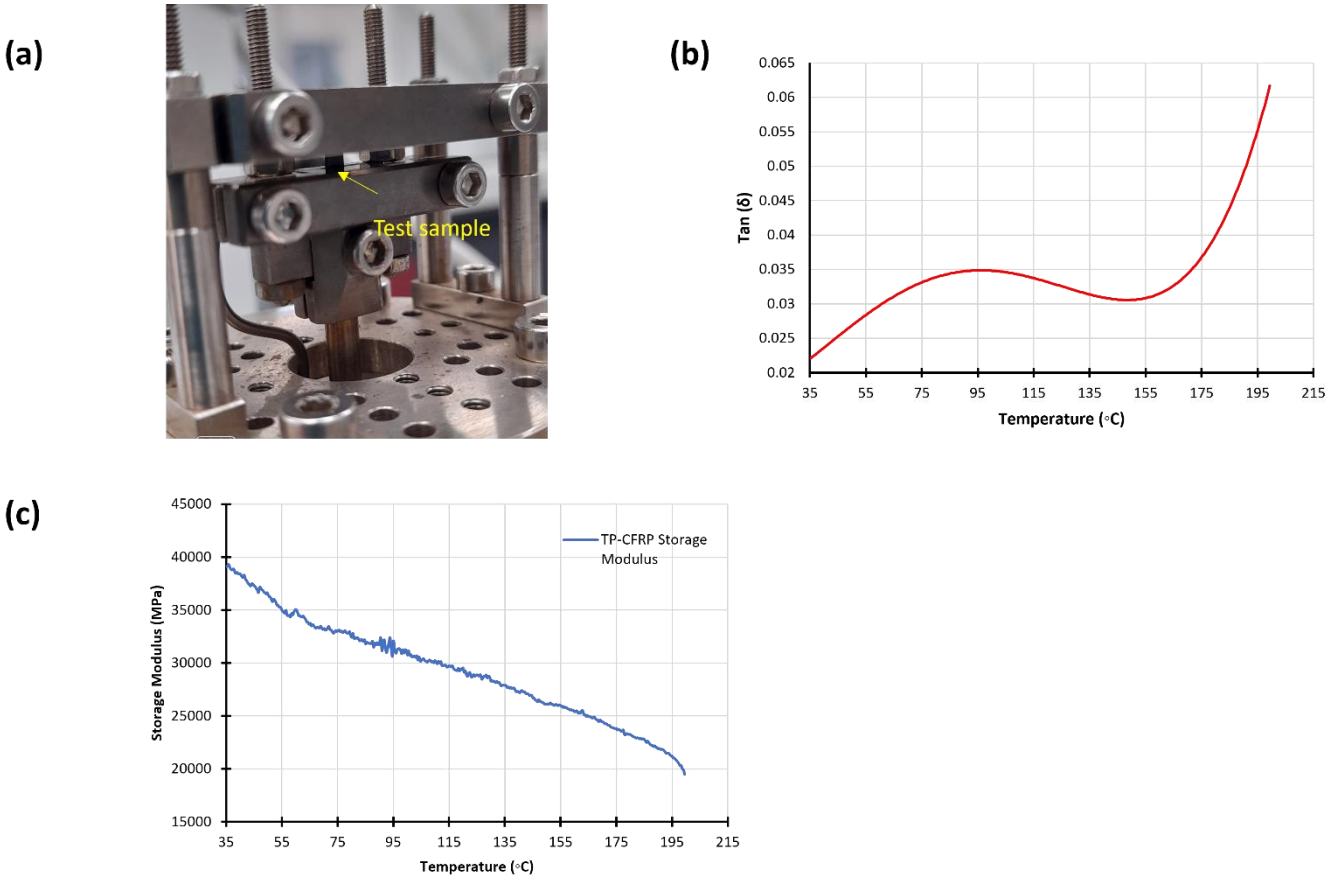

Figure 41. Dynamic-Mechanical Analyzer (DMA) test results. (a) test setup, (b) tan δ versus temperature, and (c) storage modulus (E') versus temperature.

4.2.3 CREEP/RECOVERY TEST

A tension clamp was employed to conduct a creep / recovery test using a PerkinElmer® DMA 8000 instrument, Northumbria University. The test specimens had a dimension of 20 mm × 5 mm × 2 mm. The experiments were carried out at a temperature of 85°C, and the specimens were allowed to equilibrate at this temperature for 5 minutes prior to the application of a constant temperature and stress. A constant load of 4N was applied to the material for 15 minutes at 85°C, followed by an identical 15-minute recovery step. The specimens were subjected to these creep testing conditions for a duration of 30 minutes to observe their creep and recovery behaviours. Figure 42 displays one example of the strain-time curves which illustrate the creep and recovery characteristics of TP-CFRP composites. The results show the typical creep behaviour of viscoelastic materials, characterized by instantaneous elastic deformation, primary creep, and secondary creep. It's worthwhile to note that due to the lower levels of stress and shorter creep durations in these studies, creep rupture of the specimens did not occur.

The stress relaxation characteristics of TP-CFRP were explored utilising the DMA machine. The experimental setup involved applying a predetermined stress level of 0.5 N to a 10 mm × 2 mm × 0.5 mm sample, followed by monitoring its response as it gradually eased over a 10-minute duration. The stress relaxation profile typically exhibits two distinct phases: an initial variable-rate relaxation phase marked by rapid stress reduction and a subsequent steady-rate relaxation phase characterised by a slower and more consistent decrease in stress levels. In accordance with Figure 42(b), our observations for the shown example indicated the presence of both relaxation stages. TP-CFRP exhibits a unique viscoelastic response due to the combination of its carbon fibre reinforcement and polymer matrix. When subjected to a constant stress load, CFRP tends to undergo minimal stress relaxation over time, as the high tensile strength of carbon fibers and the resilience of the polymer matrix contribute to maintaining the applied stress.

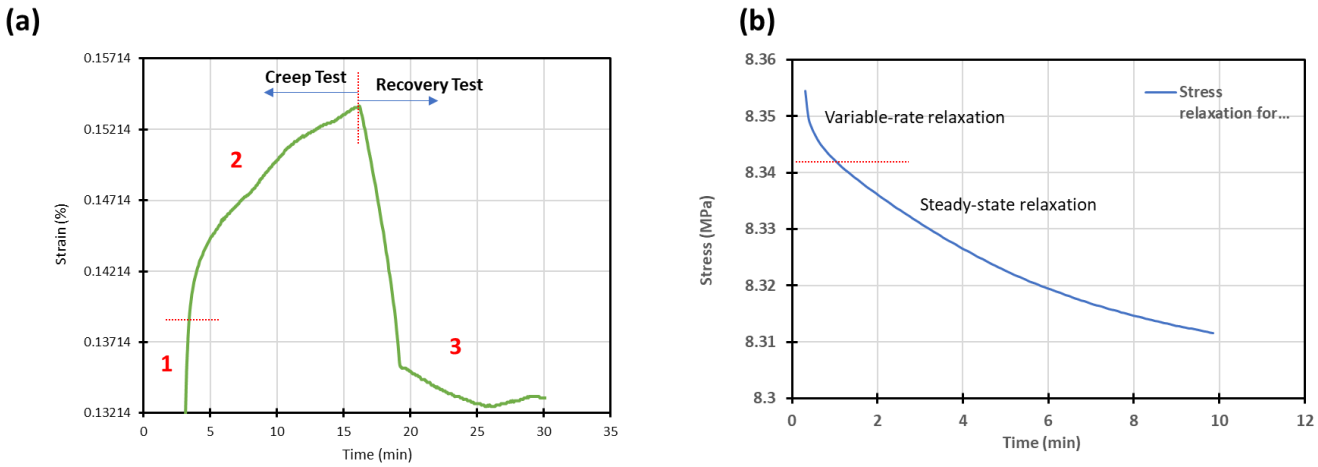

Figure 42. Creep and recovery and stress relaxation curves of TP-CFRP at constant temperature of 85°.

4.3 TENSILE TESTS

4.3.1 TEST PROCEDURE

Tensile tests on TP/CFRP at 0º and 90º orientations were executed according to the standard ASTM D3039 [11]. Due to the uncertainties that usually entail the testing of UD composites, two different geometries were tested:

- Thick coupons: 250 mm x 25 mm x 2.5 mm
- Thin coupons: 250 mm x 15 mm x 0.5 mm

Coupons of both geometries were extracted from plates manufactured by tPE. DIC was used to monitor the evolution of strains during the tests.

To determine the optimal setup of the tests, a trial and error procedure was followed employing the thick coupons, because their bigger dimensions mean that they are able to withstand higher forces during the tests and therefore potential issues become more evident. Initially, a coupon without tabs was tested; no failure appeared because of slippage issues (Figure 43).

Figure 43: Coupon tested without tabs after test finished.

After that, it was decided to glue tabs in the standard way to smooth transfer loads from the machine to the coupon, that is to say, with both ends at 90º. In this case, an undesired failure mode was obtained because failure appeared at the tab ends (Figure 44), which is the weakest part of the coupon in thin configuration because of the stress concentrations that are induced. Besides, it is necessary to take into account that this laminate is much weaker in the transversal direction, so any load that is transferred in a non-longitudinal direction may potentially cause premature failure of the coupon.

Figure 44: Coupon tested with sharp tabs after failure.

Finally, a configuration using tabs milled at 45º in one end to smooth load transfer even more proved to be effective, leading to acceptable force values and more appropriate failure modes as shown in Figure 45.

Figure 45: Coupon tested with milled tab ends after failure.

Results of all tests performed are reported in the following section 4.3.2.

4.3.2 TEST RESULTS

QS tensile tests on 0º coupons

Results of the QS tensile tests for the 0º coupons are depicted in Figure 46 and Figure 47 for the thick and thin coupons respectively.

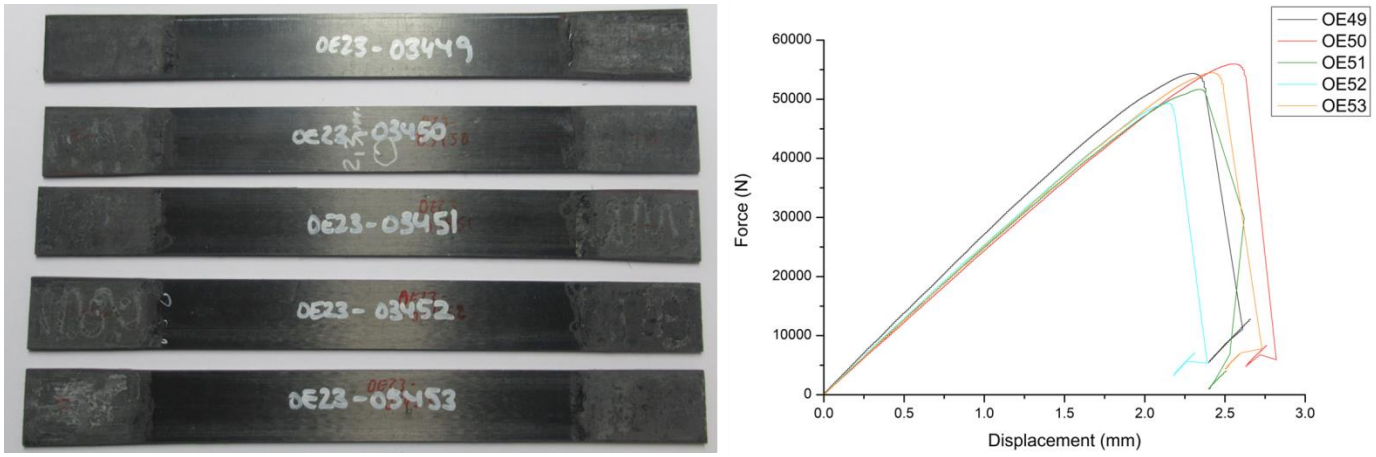

Figure 46: Aspect of the coupons (left) and force-displacement values from QS tests at 0º (right), for the thick coupons.

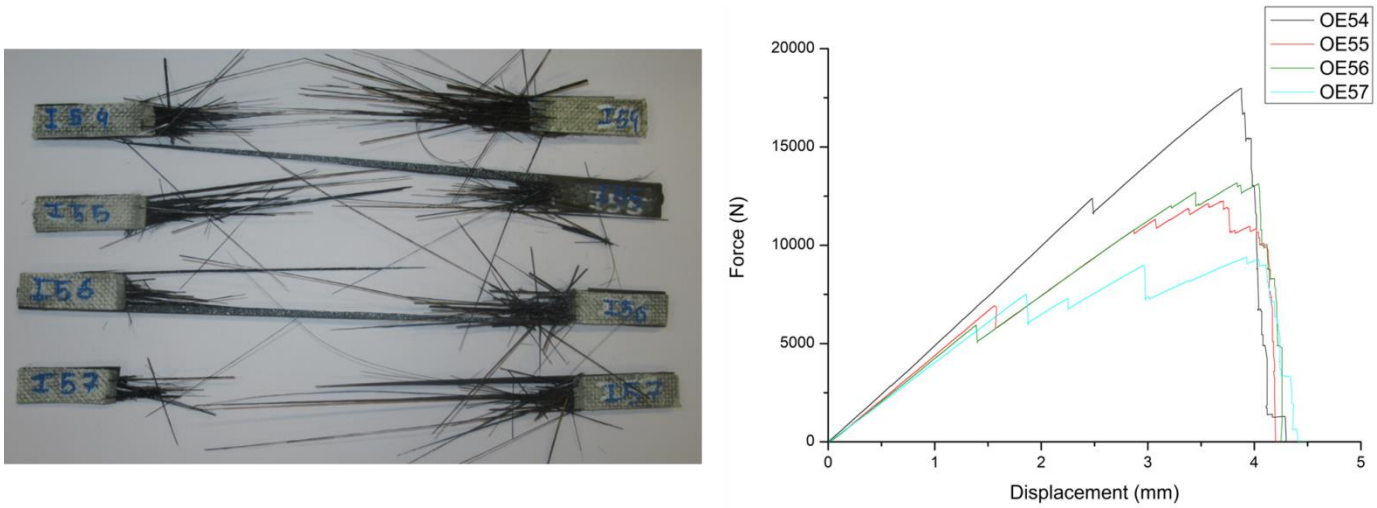

Figure 47: Aspect of the coupons (left) and force-displacement values from QS tests at 0º (right), for the thin coupons.

Comparing Figure 46 and Figure 47, it can be seen that a more appropriate behaviour is obtained in the thin specimens. If we convert the data to stress values, thick coupons break at around 1000 MPa, which is below the limits estimated by tPE. On the other hand thin coupons, even though the present a higher dispersion, reach values in the range 1600-2000 MPa, much more performing material in this sense. Besides, it can be seen that the material is able to withstand load even if it partially fails until the ultimate strength is reached. Thus, the thin geometry was selected as the most appropriate to carry out the dynamic tests reported below in this section.

QS tensile tests on 90º coupons

Results of the QS tensile tests for the 0º coupons are depicted in Figure 48 and Figure 49 for the thick and thin coupons respectively.

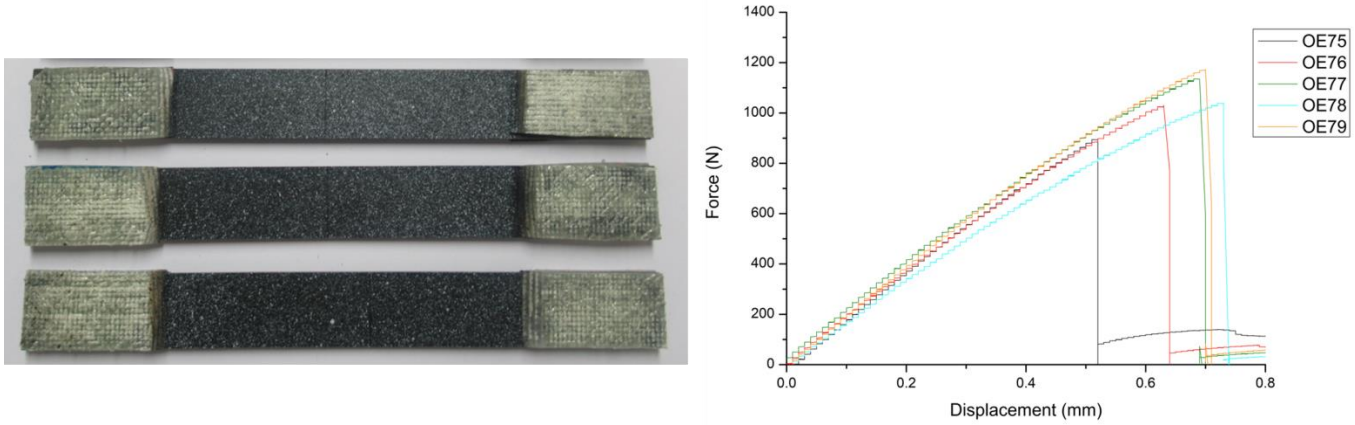

Figure 48: Aspect of the coupons (left) and force-displacement values from QS tests at 90º (right), for the thick coupons.

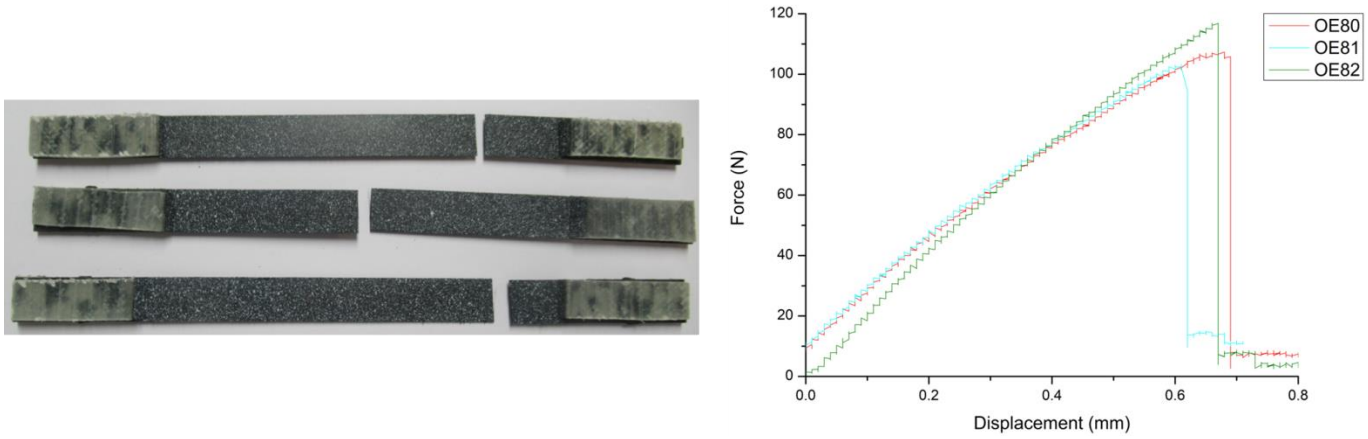

Figure 49: Aspect of the coupons (left) and force-displacement values from QS tests at 90º (right), for the thin coupons.

Looking at the results obtained, transversal failure is obtained for all coupons regardless of the geometry employed. Also ultimate stress values are in the range 16-18 MPa in both cases, so it is concluded that in this configuration of the material the geometry of the coupons does not play a role regarding the execution of the tests and the values obtained from them. It is remarkable to mention that, if these results are compared with the ones at 0º, much less performance (60x to 100x less performance depending on the geometry) is obtained, so this aspect may be critical for the real performance of the material and has to be carefully considered in the design stage of the laminates used in the FES components.

Dynamic tensile tests

Dynamic tensile tests were carried out on 0º coupons at $50s^{-1}$ strain rate. The aspect of the coupons after the test is presented in Figure 50. Given the nature of this material, the main objective of this test is to determine how much stiffer the material becomes when subjected to dynamic loads, that is to say, the sensitivity of the Young modulus of the material at high strain rates.

Figure 50: Aspect of the 0º coupons after dynamic tensile tests at $50s^{-1}$.

Regarding this tests, two major remarks can be made. Firstly, the failure mode of the coupons, although longitudinal as in the QS tests, seems much less controllable. Failure tends to appear at the end of the coupons or even within the clamped length (not at the tabs' end as could be easily interpreted as potentially improvable from a technical point of view). Secondly, once the first elements of failure appear, it propagates suddenly in an abrupt

manner, in such a way that the coupon gets completely broken and consequently is not able to withstand loads anymore. As a result, force values measured are lower here than in the QS tests previously reported on the thin geometry.

4.4 QUASI-ISO TENSILE TEST

4.4.1 TEST PROCEDURE

In the development process of a material card for simulation codes representing the behaviour of strongly anisotropic composites, it is always recommendable to test in tensile condition the same material formulation in a quasi-isotropic ("quasi-iso") lay-up ($([0|45|-45|90]_s)_2$ in this case) to cross-check the performance of the material models, enriching at the same time the tensile analysis reported in section 4.3. So, a series of quasi-isotropic coupons with the same dimensions as the thick QS tensile tests (250 mm x 25 mm x 2.5 mm) were tested at QS velocity. To ensure consistency of results, ASTM D3039 was also followed in this characterization, and tabs with ends milled at 45º were employed. Due to the cross-checking nature of the test, only three samples were tested.

4.4.2 TEST RESULTS

The aspect of the CT coupons after the test is shown in Figure 51. The Force-displacement curves are presented in Figure 52.

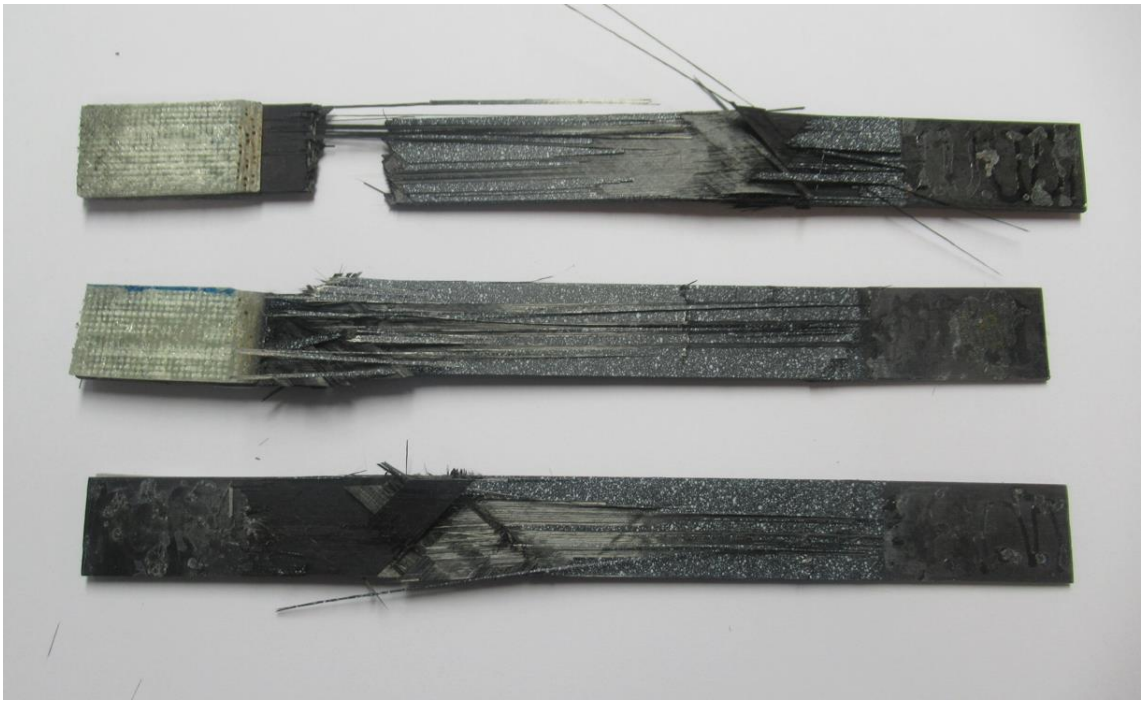

Figure 51: Aspect of quasi-iso coupons after QS tensile test as per ASTM D3039.

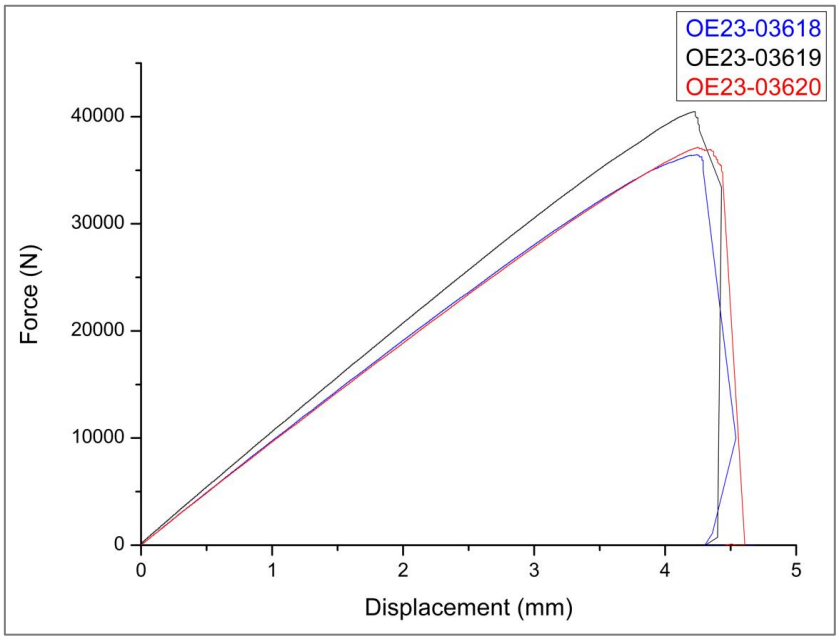

Figure 52: Force-displacement curves of the quasi-iso tested coupons.

Looking at the broken samples, the first feature to highlight is that failure occurs within the clamps as advised in the standard and not in the tab ends. In this test, the likelihood of this failure location was higher than in the 0º UD coupons with thick dimensions, because the amount of force put in place in the test is significantly lower in this test (in the range 35-40kN as shown in Figure 52 above). Also, a sharp and sudden decrease in force values is registered, which indicates that no slipping is taking place; this also correlates well with the fact that all coupons fail in a brittle and instantaneous manner.

Regarding the failure mechanism of the coupons, in all cases there are some release of material belonging to the outer layers at 0º right before the coupons broke. After that point, failure is mostly driven by the breakage of the layers at ±45º, potentially triggering other failure mechanisms afterwards (to be remarked that all coupons from Figure 51 present at least a location where layers at ±45º are in an out-of-plane position as a consequence of failure).

4.5 COMPRESSION TESTS

4.5.1 TEST PROCEDURE

Compression tests on the TP/CFRP material were carried out in pure UD configuration (both at 0º and 90º) and quasi-static velocity following the standard ASTM D6641 [12]. Therefore, coupons of 140 mm x 12 mm x 2.5 mm were manufactured to this end. Five coupons were tested for each orientation.

In compression tests, avoiding buckling is a key issue to ensure the highest quality and validity of the results obtained. Thus, most of the coupons' length was clamped, leaving only 12 mm of free length in which compression effectively took place. A scheme of the test setup is provided in Figure 53. Besides, DIC was also employed to track strain throughout the test and determine in a robust manner if buckling appears during the tests; virtual extensometers and tracking areas were defined to this end as depicted in Figure 54.

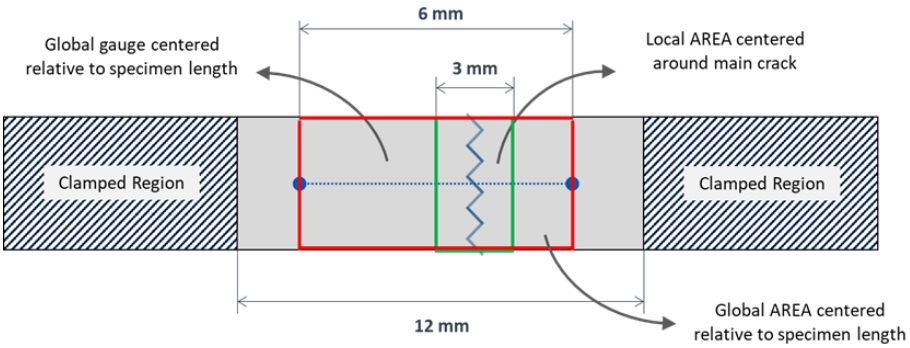

Figure 53: Setup of the compression tests including DIC monitoring features.

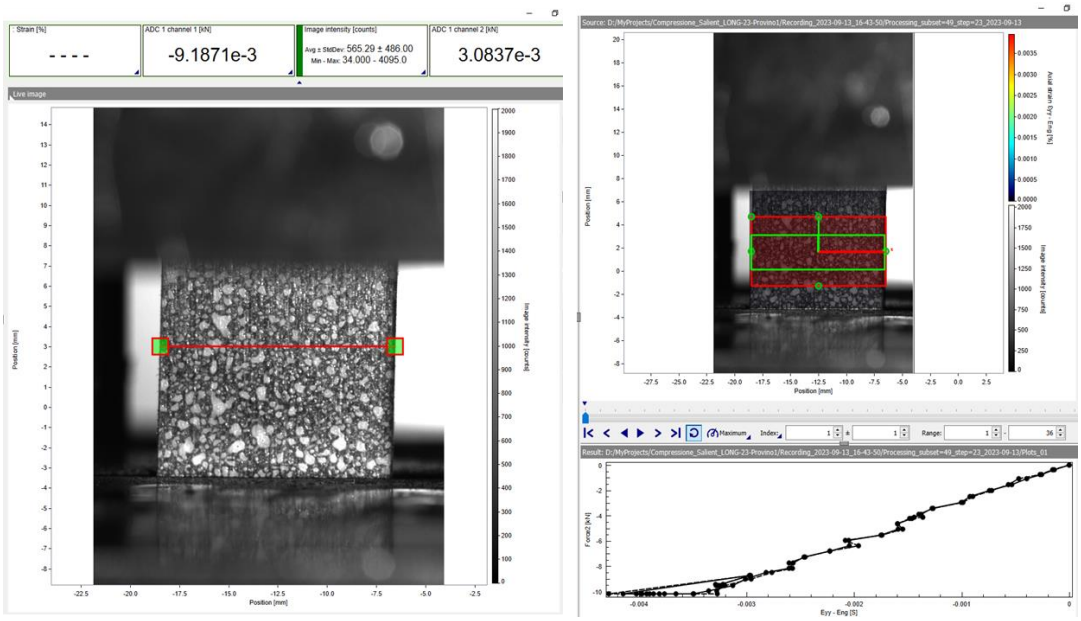

Figure 54: DIC was used to track the evolution of compression tests.

4.5.2 TEST RESULTS

Compression tests at 0º orientation

The aspect of the compression coupons after testing is presented in Figure 55. The results are graphed in Figure 56.

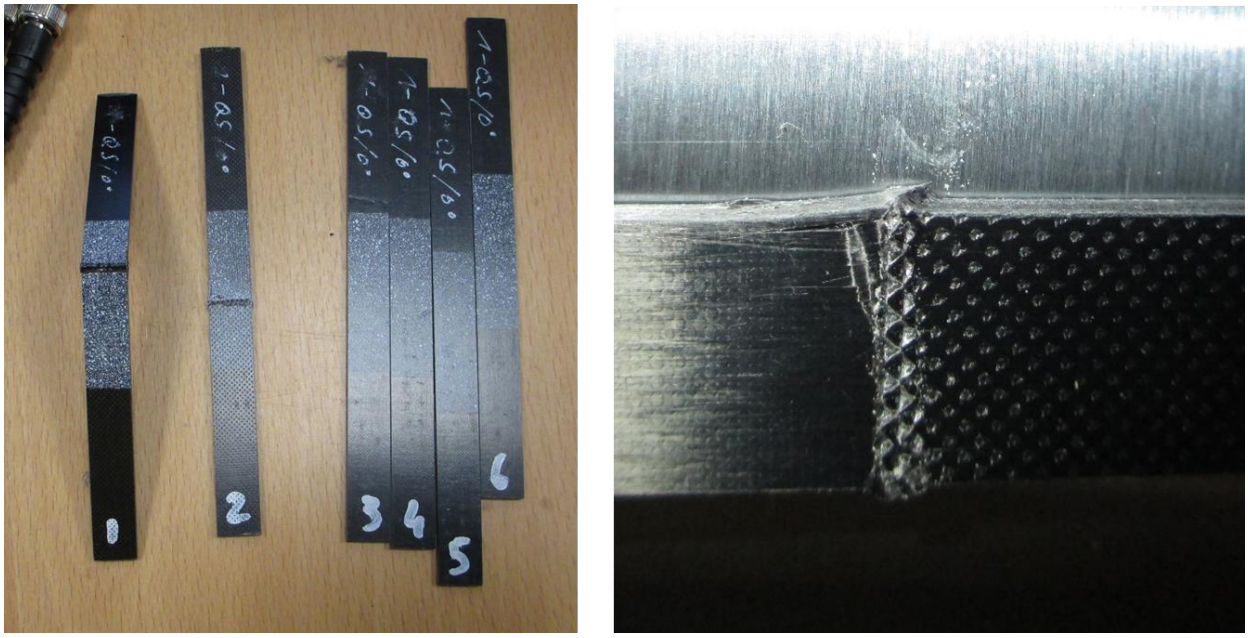

Figure 55: Compression coupons oriented at 0 º after testing (left) and detail of the failure mechanism (right).

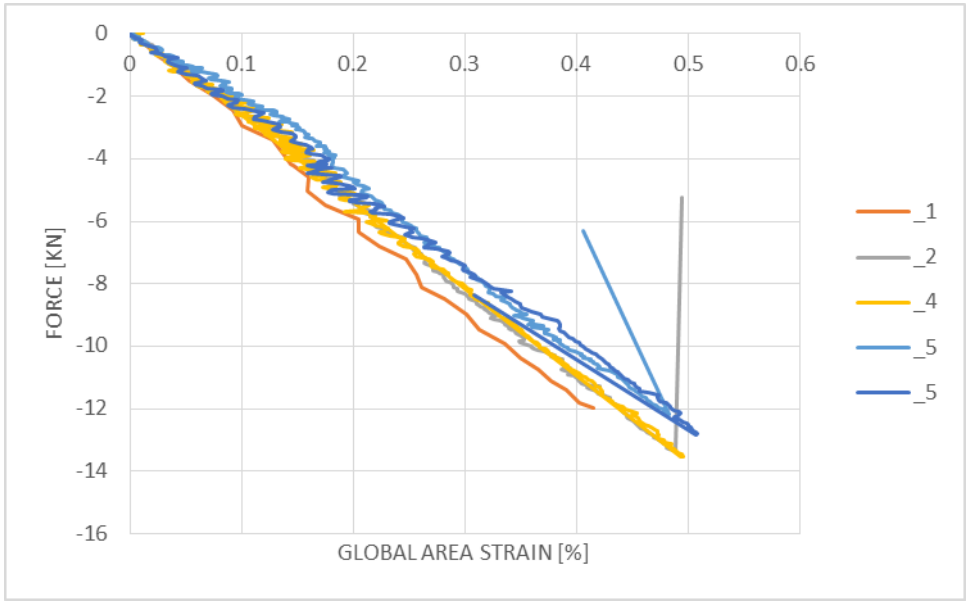

Figure 56: Force vs global area strain measured during the compression tests at 0º.

Coupons tested showed consistent behaviour during the test, achieving comparable values in terms of compressive modulus (98 GPa on average), ultimate compression strength (493 MPa on average) and compression at break (0.47% on average). Failure mode is repetitive across all samples, as can be seen in Figure 55 (right) the breakage of the carbon fibres occurs at a certain compression level, and the test is stopped immediately after that event. Thanks to the high stiffness of the material in this orientation, no signs of buckling appeared during the test, as is also evidence by the shape (straight line) of the curves obtained in Figure 56.

Compression tests at 90º orientation

The aspect of the compression coupons after testing is presented in Figure 57. The results are graphed in a similar fashion to the previous ones in Figure 58.

Figure 57: Compression coupons oriented at 90 º after testing

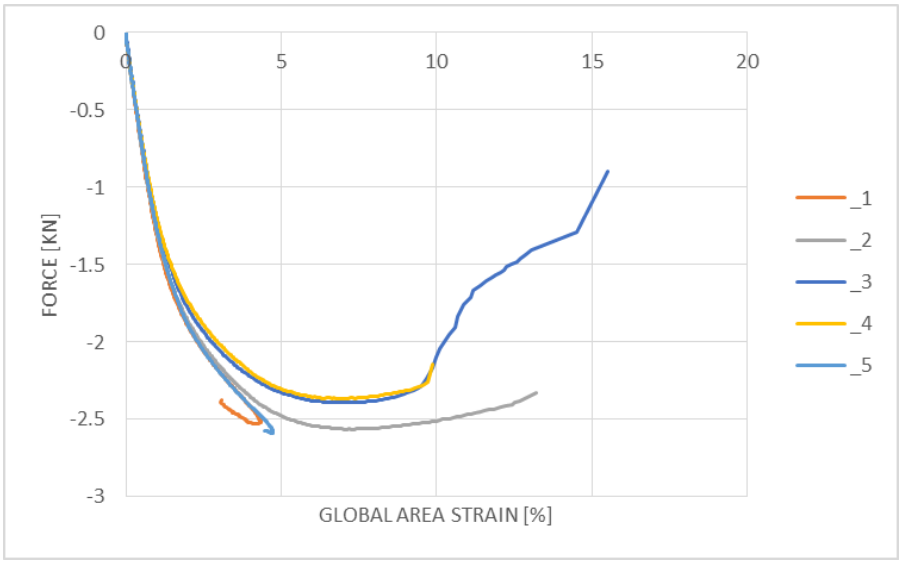

Figure 58: Force vs global area strain measured during the compression tests at 90º.

The values obtained for the coupons at 90º orientation are significantly lower than those obtained on 0º coupons, as the carbon fibres do not play a significant role here and basically what was tested was the polyamide matrix. Anyway, coupons tested showed consistent behaviour during the test again, achieving comparable values in terms of compressive modulus (5.4 GPa on average), and ultimate compression strength (79 MPa on average). There is great dispersion in the compression at break measured, although this is typical of this kind of test and materials because it is very challenging to determine during the tests the exact point at which the matrix is collapsing and/or some buckling is appearing and therefore tests have to be stopped. Regarding failure modes, they are repetitive across all samples and in some cases the oblique failure surface suggests that at least some amount of out-of-plane displacement has occurred before or during failure.

4.6 TRANSLAMINAR FAILURE TESTS

4.6.1 TEST PROCEDURE

Translaminar fracture under tension or compression is one of the primary failure modes of UD fibre-reinforced composites. The engineering objective of Salient to develop an optimized, efficient, sustainable, and damage tolerant solution employing TP/CFRP requires the characterization of the fracture toughness of the material in order to maximize its load-carrying performance. Besides, this is particularly relevant when FEM is used to simulate failure and damage occurring in composite laminates such as fibre failure, matrix breaking, and delamination. To this end, compact geometries are frequently recommended over other coupon configurations because these have predominantly bending stress states, which allow smaller specimen sizes to achieve plain strain states.

Hence, both compact tension (CT) and compact compression (CC) tests were carried out within Task 3.2. A specific laminate $([0|90]_9)_s$ with thickness of 4.5mm was manufactured to this end, following the recommendations from IDI. The coupon geometry defined is inspired in the general guidelines provided by ASTM D5045 [13], ASTM E399 [14], and also success stories found in literature [15], and are depicted in Figure 59. The execution of the test followed the procedure set by ASTM E1922 [16].

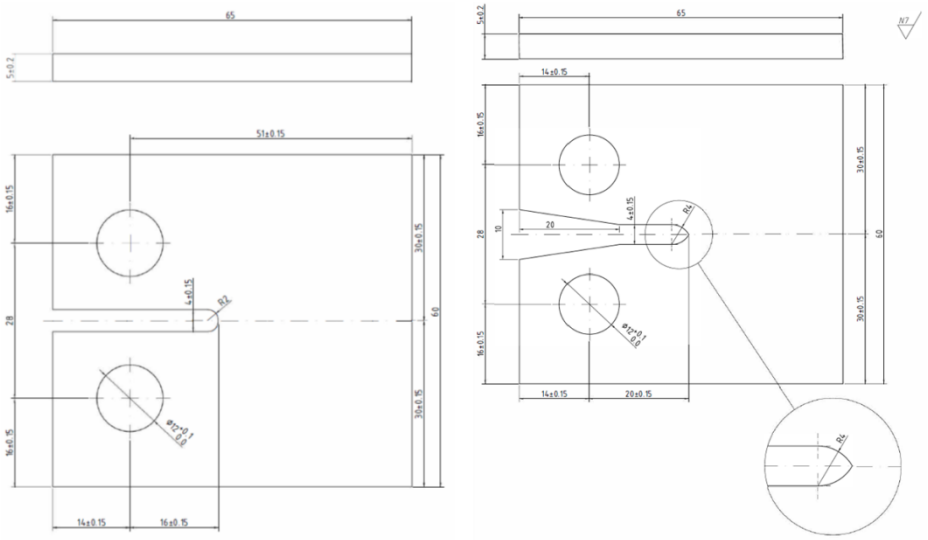

Figure 59: Coupon geometries for CT (left) and CC (right) tests.

Following the recommendations of ASTM D5045, to ease crack formation and propagation, a 0.4 mm width sharp notch was sawed in the CT coupons from the notch root. All notches were measured to keep traceability of results during and after the test, an example is shown in Figure 60. DIC was employed in both CT and CC tests to keep track of deformations through the tests.

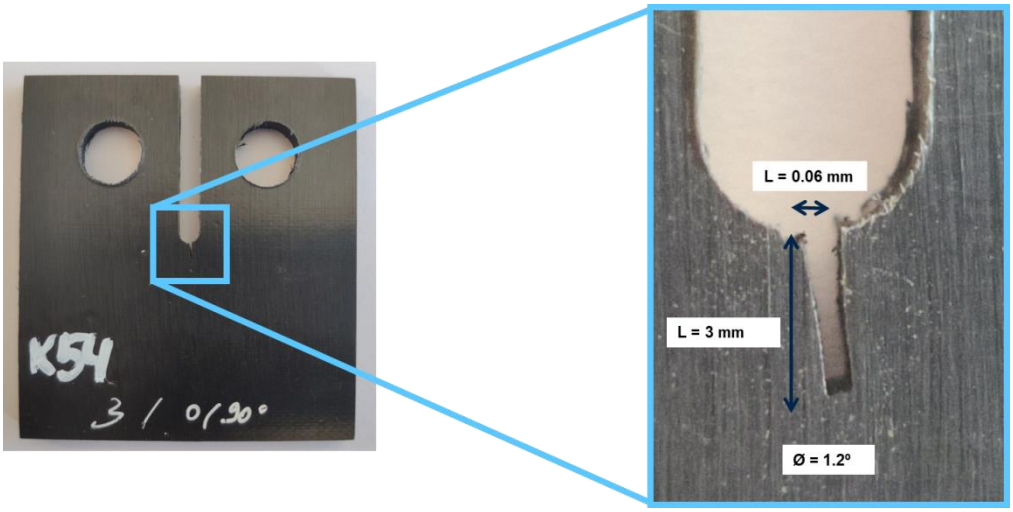

Figure 60: Sharp notches sewed on CT coupons to ease crack formation and propagation.

4.6.2 TEST RESULTS

Compact Tension (CT)

The aspect of the CT coupons after the test is shown in Figure 61. The Force-displacement curves are presented in Figure 62.

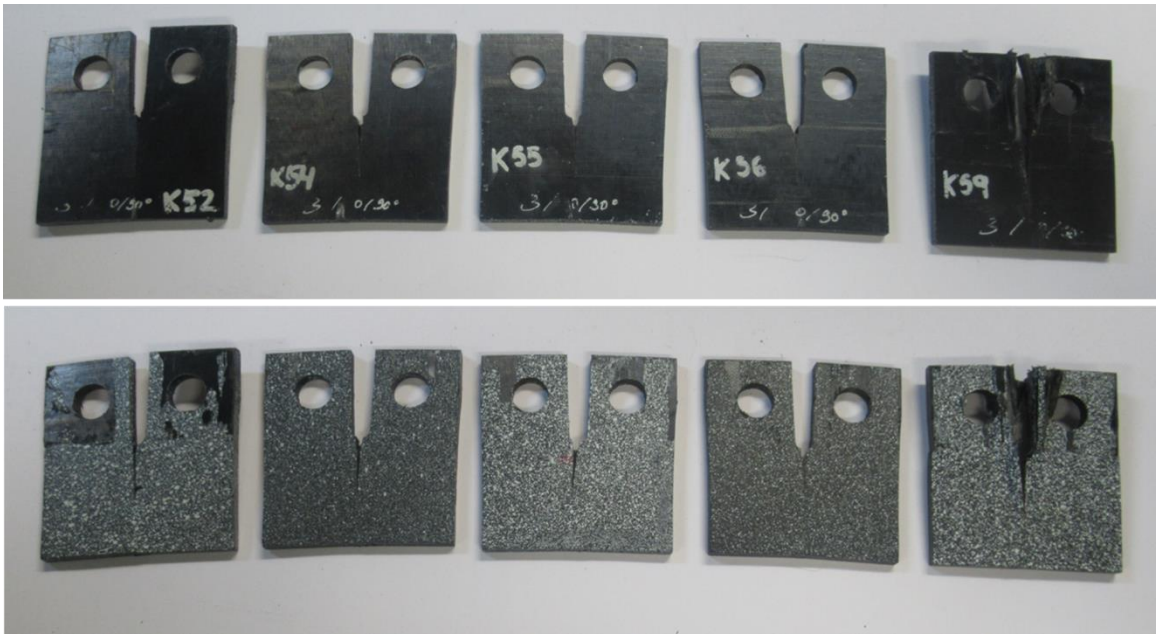

Figure 61: Aspect of CT coupons after testing.

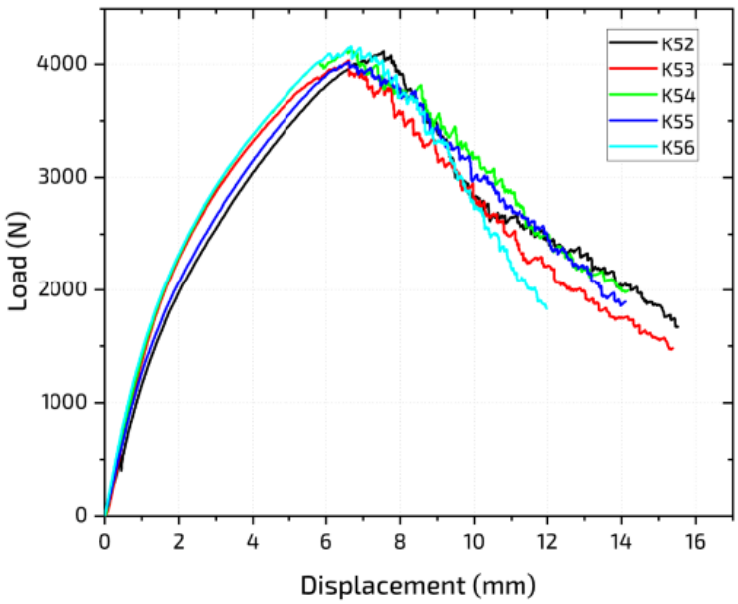

Figure 62: Force-displacement curves corresponding to CT coupons.

In general, an appropriate and consistent behavior during the tests was observed in all coupons, without undesired failure locations (e.g. in the holes or perpendicular to the notch) or premature failure signs. Force increases until cracks appear. Then, cracks develop smoothly and progressively. It is worth mentioning that at advanced stages of the tests, in some of the coupons evidences of crushing failure by compression forces in the coupon side opposite to the notch appeared (Figure 63). This has to be taken into account when working with the data coming out from these tests as they might not be usable from a certain point.

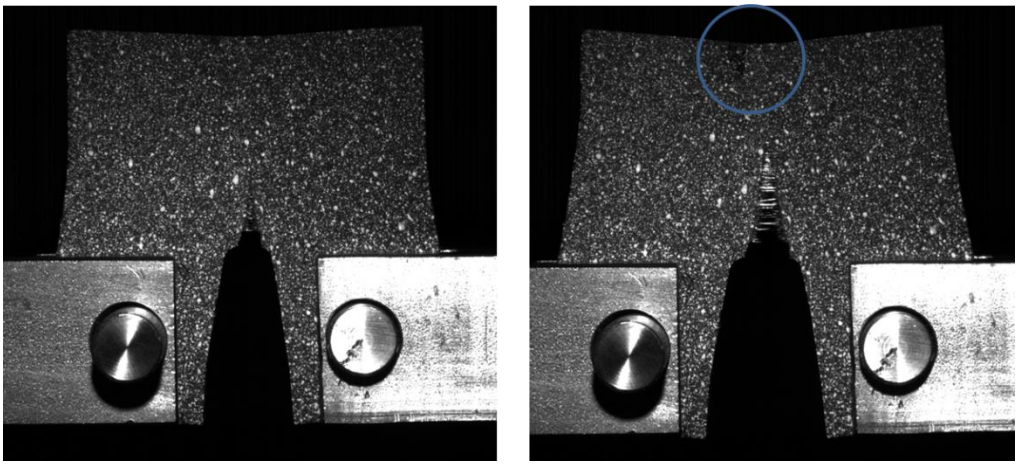

Figure 63: Evolution of CT test for K54 coupon. Left: Intermediate stage of the test. Tight: Late stage of the test showing signs of crushing by compression.

Compact compression (CC)

The aspect of the CT coupons after the test is shown in Figure 64. The Force-displacement curves are presented in Figure 65.

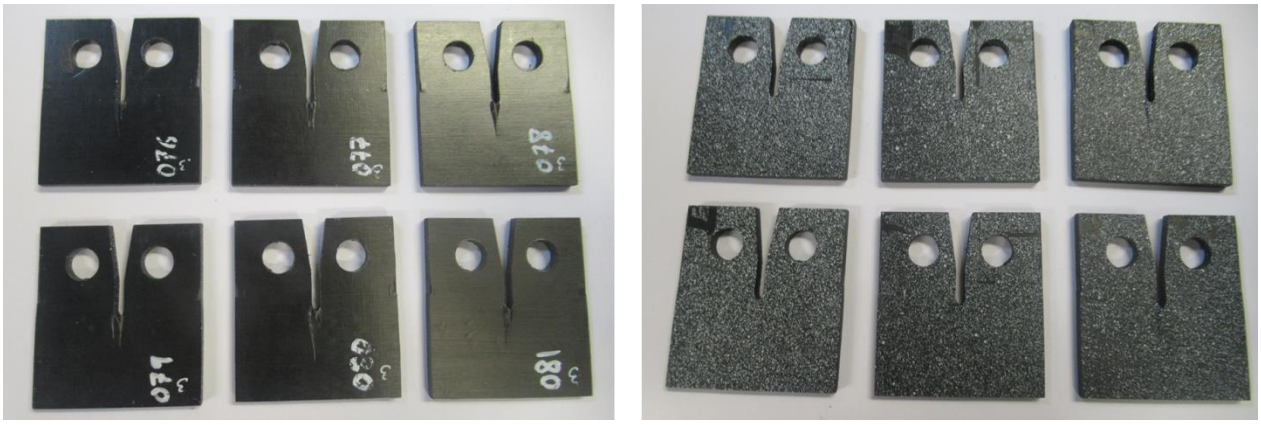

Figure 64: Aspect of CC coupons after testing.

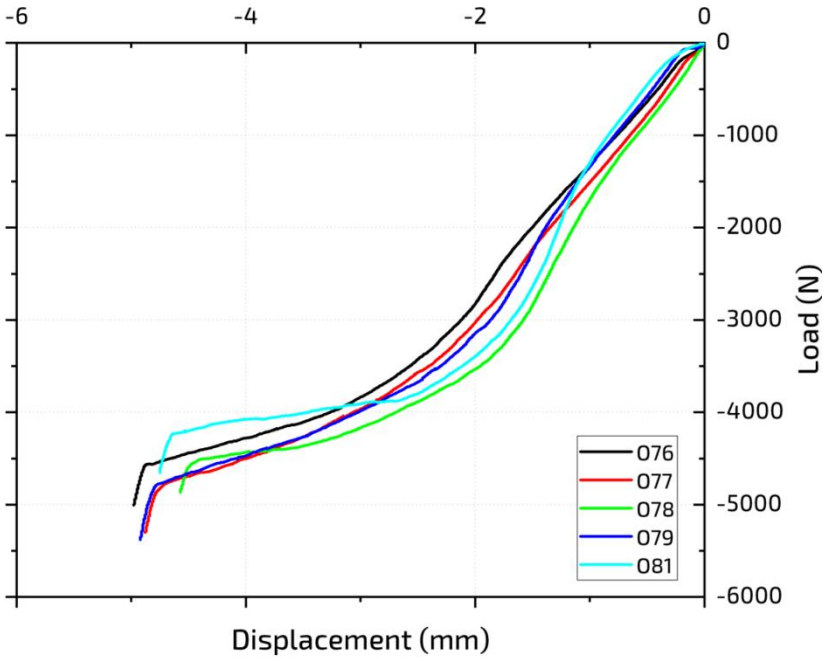

Figure 65: Force-displacement curves corresponding to CC coupons.

Also in CC tests the evolution of the tests was as expected, cracks of different topologies were observed in almost every coupon tested, appearing in most occasions at high displacements of the actuator as depicted in Figure 66, in which it can be seen that once cracks are developed, both halves of the coupon are almost in contact. On the other hand, there is some more dispersion in the results obtained in the CC tests compared to the CT tests, which is acceptable due to the higher complexity associated to the compression tests.

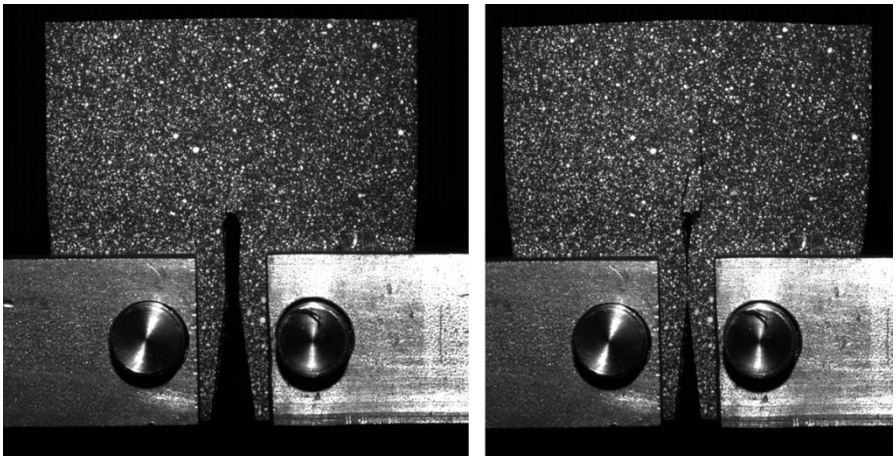

Figure 66: Appearance of cracks during CC test.

4.7 INTERLAMINAR FAILURE TESTS

4.7.1 TEST PROCEDURE

Additionally to the characterization of translaminar failure, interlaminar failure is required to have a complete understanding of the failure mechanisms of TP/CFRP material. This is due to the fact that the strength of CFRP laminates can be significantly reduced in directions that are not strengthened on purpose, such as the interlaminar direction. Besides, CFRP laminate may be susceptible to impacts, with out-of-plane impacts causing internal damage, for instance triggering peeling mechanisms. Hence, a damage tolerant design must determine how resistant a material is to interlaminar crack propagation, which is in practice done by fracture toughness testing in various modes. In general, for homogeneous isotropic materials, only fracture Mode I (crack opening mode) needs to be evaluated. In reinforced composites with anisotropic behaviour, it is advisable to evaluate other fracture modes. In this task, failure under Mode I and Mode II (crack sliding mode) is analysed (Figure 67).

Figure 67: Interlaminar fracture tests in Mode I and Mode II.

In both cases, the coupons employed have dimensions 200 mm x 25 mm x 3mm, with a 80mm-long Teflon insert in the mid-plane to allow controlled fracture, and a pure UD (0º) lay-up as schematized in Figure 68.

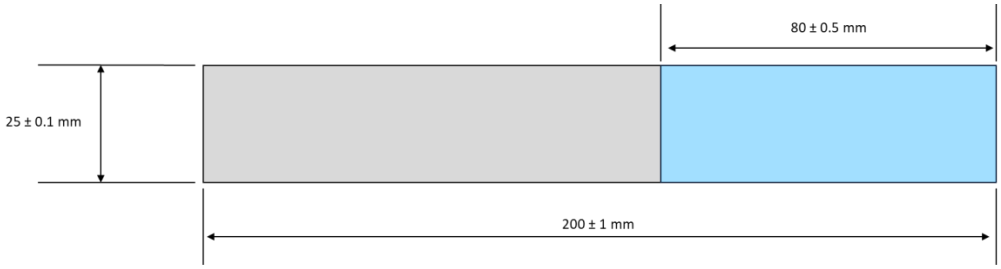

Figure 68: Coupon geometry for interlaminar failure tests.

The tests were executed following relevant standards. Interlaminar fracture toughness in Mode I (Double Cantilever Beam, DCB) were carried out as per ASTM D5528 [17]; tests in Mode II (Calibrated End-Loaded Split, C-ELS) were carried out following ISO 15114 [18].

Regarding the execution of Mode I tests, metallic hinges were purchased and glued to the coupons to ensure proper load transfer from the machine. A detail of the test setup can be seen in Figure 69. Several marks were painted on the coupon to enable a calibrated post-test measurement of crack propagation in the test videos that were generated.

Figure 69: Test setup of interlaminar failure tests in Mode I with detail of the hinges employed.

Regarding the execution of Mode II tests, dedicated tooling was designed and manufactured (Figure 70) following the recommendations from the standards as well as best practices found in literature [19]

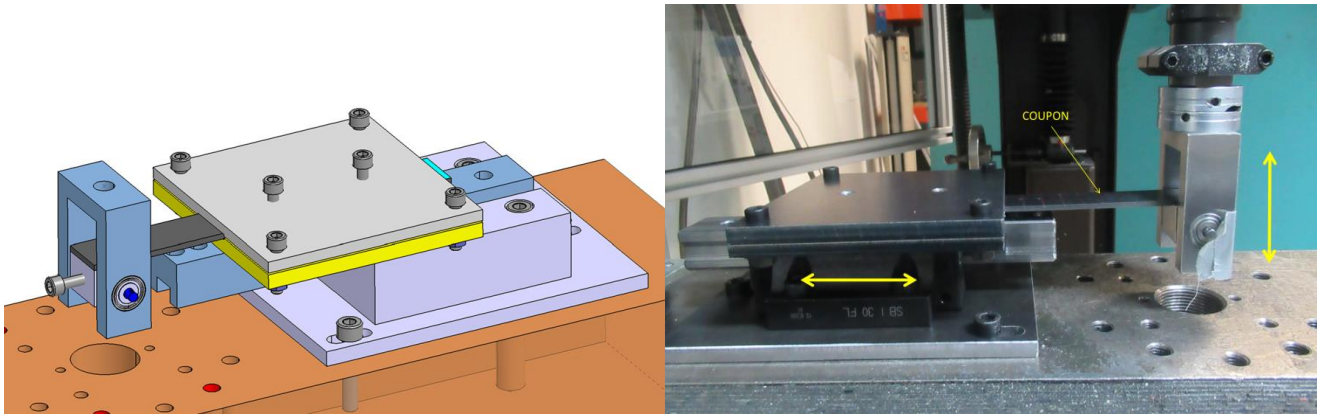

Figure 70: Tooling design (left) and actual tooling (right).

4.7.2 TEST RESULTS

Mode I tests (DCB)

The aspect of the coupons in an advanced stage of the Mode I test is shown in Figure 71. The results (Force-displacement curves measured by the machine sensors) are presented in Figure 72.

It can be seen that after the mandatory pre-cracking state (not included in the graph) does not introduce significant dispersion in the results. The loading stage is repetitive and consistent across all tested coupons. From a certain point around 40-50 mm displacement, crack propagation occurs in a more abrupt manner. After each delamination step, force values decrease until the end of the test; in this stage more dispersion is observed between the samples as expected. In Figure 72 also the unloading process is depicted.

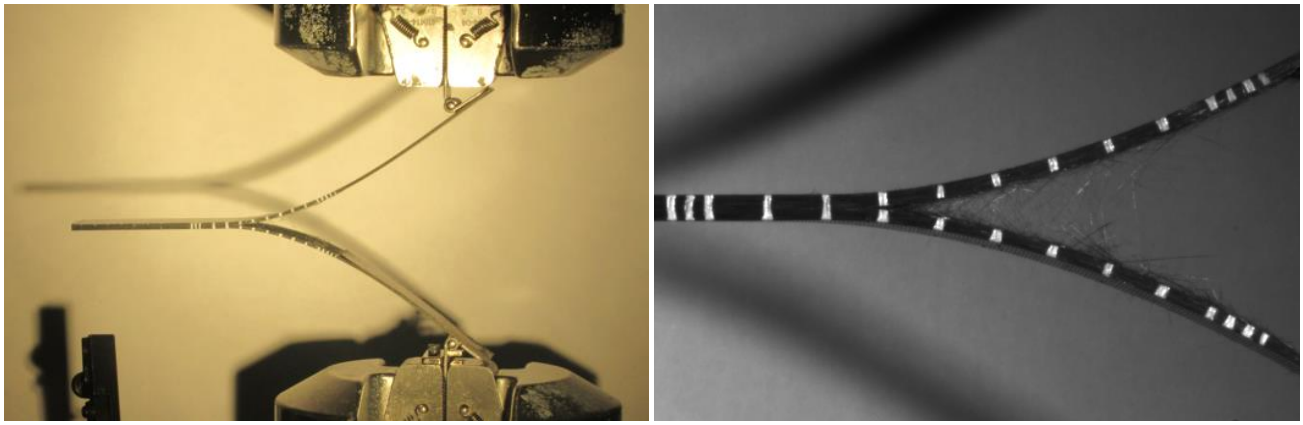

Figure 71: Coupon during Mode I (DCB) test (left) and detail of the crack propagation (right).

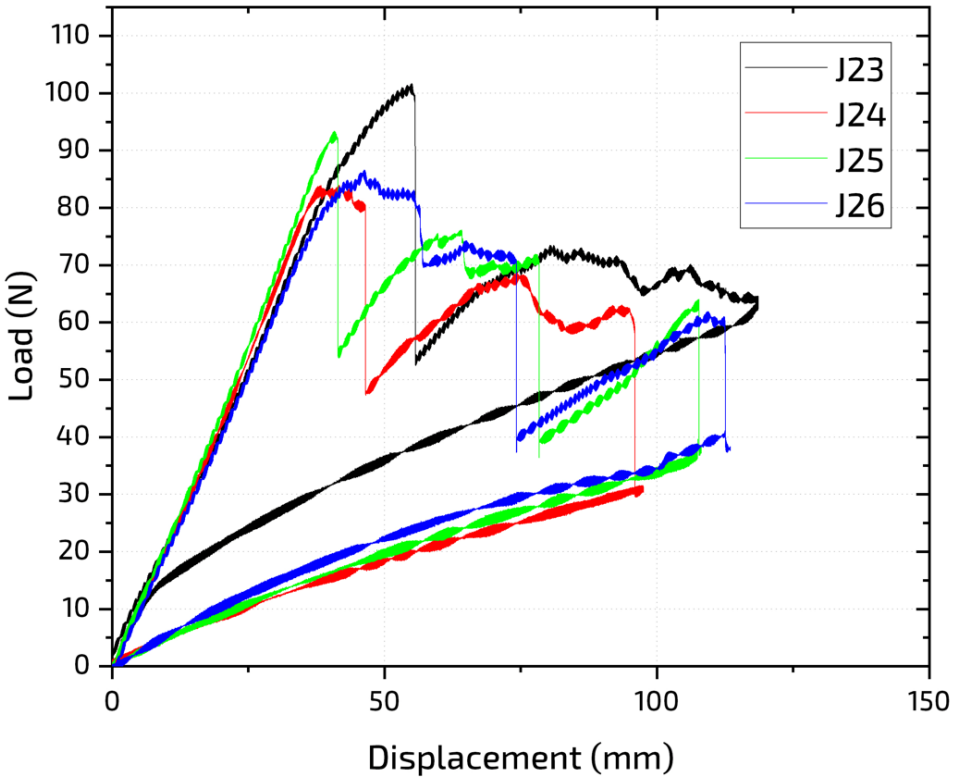

Figure 72: Force-displacement results of Mode I tests.

Mode II tests (C-ELS)

The aspect of the coupons in an advanced stage of the Mode II test is shown in Figure 73. In these tests, failure appeared during the pre-cracking stage of the test as can be seen below. Because of the great amount of bending deformation that is introduced during this preliminary step, the high compressive forces introduced in the upper half of the material cause the breakage of the fibres. Simultaneously, there are mild signs of crack propagation (Figure 73 right), although it cannot be determined precisely how much of the energy put in place is absorbed in the crack propagation and how much is absorbed in the upper laminate. Hence, it is recommended to redesign the coupon geometry to minimize bending forces and maximize shear forces during the pre-cracking stage.

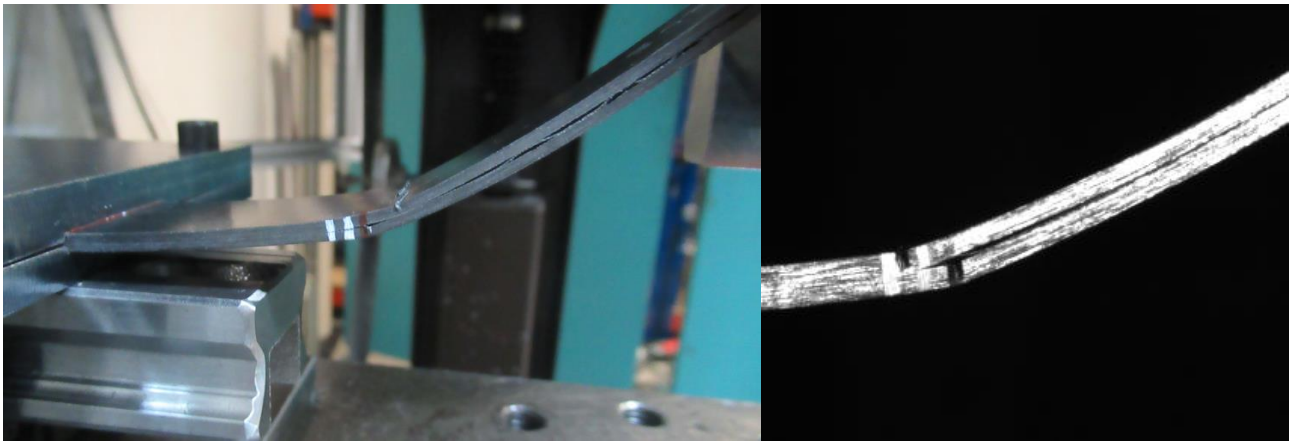

Figure 73: Coupon during Mode II (C-ELS) test (left) and detail of the crack tip area (right).

4.8 THREE-POINT BENDING TESTS

4.8.1 TEST PROCEDURE

Three-point bending tests on TP/CFRP coupons were carried out following the specifications of the standard ISO 14125 [20]. Consequently, coupons of dimensions 100 mm x 15 mm x 2 mm were produced by tPE for this purpose (Figure 74).

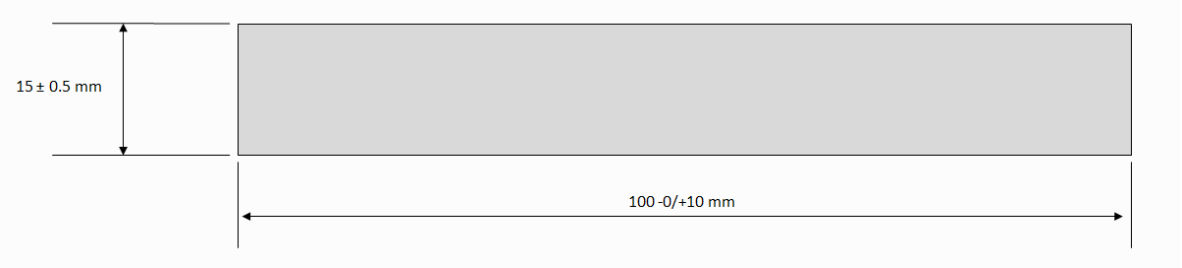

Figure 74: Geometry of the coupons used in three-point bending tests of TP/CFRP.

About the test setup, the test speed employed was 2 mm/min, with a span between supports of 27 mm. The radius of the supports and the loading edge were 2 mm and 5 mm, respectively. The test setup can be seen in Figure 75.

Figure 75: Test setup for the bending trials.

As in the case of the aluminium, three-point bending tests are used to accomplish a double objective in this testing campaign: they serve to assess the behaviour of different laminate lay-ups when the TP/CFRP is subjected to flexural forces; and on the other hand they provide a simple yet robust reference to validate the overall performance of the material cards in relatively complex load scenarios (tension and compression appear simultaneously during bending tests). Thus, three different lay-ups have been employed in these trials:

- Default configuration: $([0|90]_4)_s$
- Shear-like configuration: (±45º)
- Quasi-isotropic configuration: $([0|45|-45|90]_s)_2$

The positioning of the coupons in this test is not critical as the laminates are symmetric in all configurations.

4.8.2 TEST RESULTS

The aspect of the coupons after the bending tests is shown in Figure 76 for all tested configurations.

$([0|90]_4)_s$ (±45º) $([0|45|-45|90]_s)_2$

Figure 76: Aspect of the coupons after bending test.

The results (force-displacement and stress-strain graphs) for each tested configuration are presented in Figure 77, Figure 78, and Figure 79 respectively.

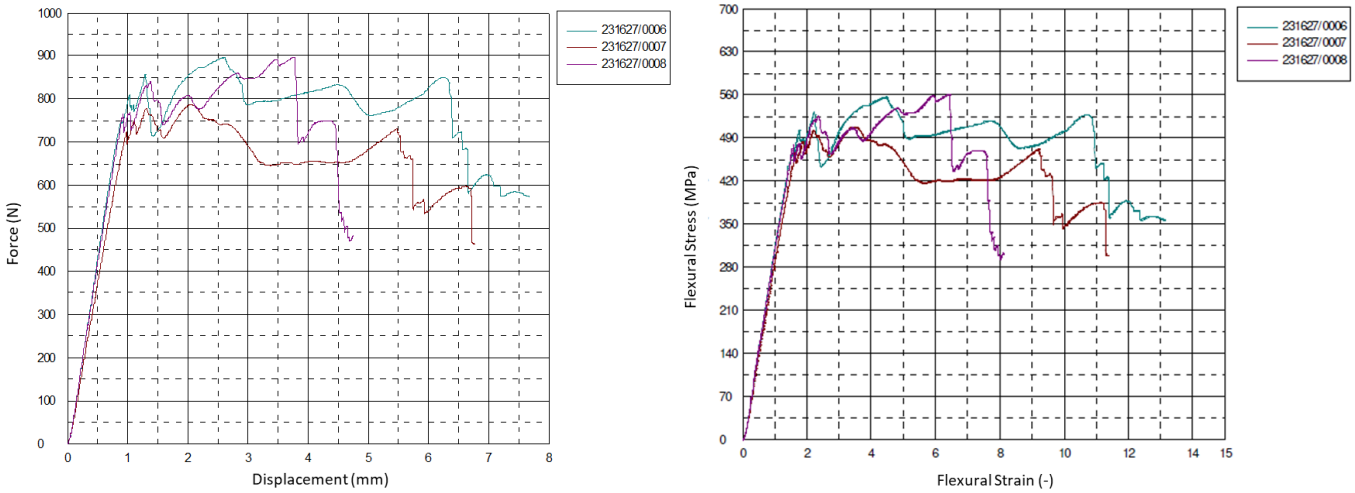

Figure 77: Bending test results for the default $([0|90]_4)_s$ configuration.

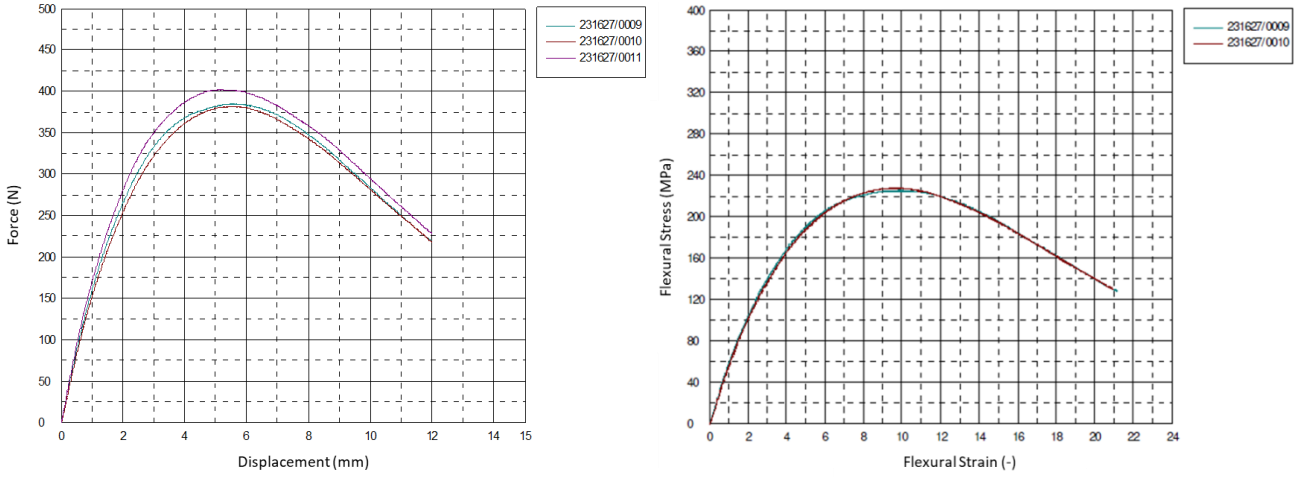

Figure 78: Bending test results for the shear-like (±45º) configuration

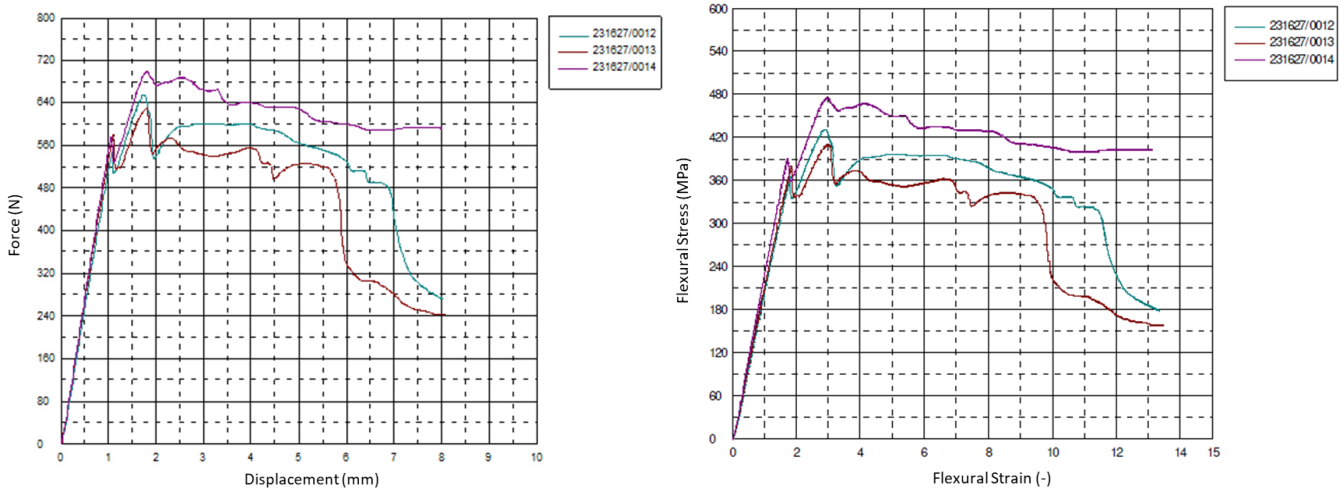

Figure 79: Bending test results for the quasi-iso $([0|45|-45|90]_s)_2$ configuration

According to the test results, the greatest performance of the material is obtained in the default $([0|90]_4)_s$ configuration (Figure 77) as expected. This laminate has the highest amount of layers at 0º among the three configurations tested, and therefore it makes sense that it is able to withstand higher forces before failure. In this

test, the initial slope is consistent and perfectly repetitive, after which a more noticeable dispersion appears in the coupons motivated by the progressive failure that develops in the material. A quite similar behaviour is found in the quasi-iso $([0|45|-45|90]_s)_2$ configuration, although in this case lower forces are achieved as there are less amount of layers oriented at 0º. The presence of layers at ±45º contributes to get a smoother development of failure during the test. Finally, the shear-like (±45º) configuration leads to the lowest force values amongst the three laminates tested, although at the same time the behaviour is the most repetitive and predictable of all of them. Finally, there is also a clear dependence of the Flexural modulus on the laminate configuration: 5-6 GPa is obtained for the shear-like configuration, 18-20 GPa is obtained for the quasi-iso configuration, and 26-28 GPa is obtained for the default configuration.

4.9 DISCUSSION ON TEST RESULTS

The TP/CFRP laminates tested and described in this section of the deliverable are built up by stacking a certain number of UD plies, as required per each test previously described. This means that the material presents strong orientation effects, especially in the pure UD configurations of some laminates used for tensile, compression and interlaminar failure tests. Thus, due to the strong anisotropy of the material, the behaviour of the TP/CFRP was extremely different depending on the specific lay-up tested, which significantly increased the complexity of the testing campaign, as in practice different orientations have to be considered as different materials from a testing point of view (coupon geometry, failure mode, test setup, machines to be employed, etc.)

In general terms, outstanding performance is found in the 0º UD laminate due to the high amount of carbon fibres inserted in the polyamide matrix. The high forces achieved during tensile tests in this configuration led to failure appearing in undesired locations (e.g. at the tabs' end) or following different failure modes than those recommended in the standards; hence, coupon geometry had to be downscaled in width and thickness directions to enable a proper execution of the tests. The evolution of tests on 0º UD laminates as well as the triggering of failure is also determined to some extent on the quality of the adhesion achieved between the carbon fibres and the polyamide matrix. On the contrary, 90º UD laminates turned out to be really soft compared with the 0º orientation. As mentioned before, this is due to the fact that in this laminate we are mostly testing the performance of the polyamide matrix without any significant contribution of the fibre material. These particularities made the testing campaign quite challenging.

Several tests considering different material lay-ups and load cases were carried out in order to get comprehensive information of the material performance as well as of the main failure mechanisms that may occur in real crash scenarios (translaminar and interlaminar failure).

Regarding the material development process as feedback to T3.1 for further work within T3.3 and the simulations of T5.2, any improvements on the adhesion of the carbon fibres and the polyamide matrix will help enhancing the already good performance of the material for crash applications, especially thinking of its use as local reinforcements to modify load transfer paths within the FES.

5. SMA/CFRP COMPOSITE CHARACTERIZATION

The testing campaign on the SMA/CFRP material had as main objective the comparative evaluation of different integration approaches of the SMA wires in the CFRP structure. Due to the complexity of the manufacturing processes needed to produce the material, the different behaviour of the wires at different temperatures due to the phase transformations (austenite ⇔ martensite) that take place, and the key influence on the effective embedment of the wires within the CFRP on the overall material performance (see D3.1 for further details on the design and manufacturing of the material), several different material configurations were tested at different temperatures (from RT up to 110ºC) on different test setups (bending and tensile), specifically:

1. CFRP material without wires → reference material

2. CFRP material with non-SMA wires embedded
3. CFRP material with 50µm diameter wires embedded
4. CFRP material with 200µm diameter wires embedded
5. CFRP material with 50µm diameter wires placed at the top of the composite

The testing program executed is also presented in Table 6. Due to material availability constraints, and considering the nature of this campaign (benchmarking of different integration approaches of SMA wires into TP/CFRP), it was decided to test only coupon per configuration and test. Besides, all aspects relative to the manufacturing of the coupons for testing, as well as all testing procedures executed and results obtained are described in the subsequent sub-chapters.

Table 6: Summary of SMA/CFRP testing campaign.

	Bending @ RT	Bending @ 75ºC	Bending @ 100ºC	Bending @RT + Heating up to 110ºC	Tensile @RT
Coupon	Reference material	Reference material	Reference material	Reference material	Reference material
	CFRP + non-SMA wires mid	CFRP + non-SMA wires	CFRP + non-SMA wires	CFRP + non-SMA wires	CFRP + non-SMA wires
	CFRP + SMA 50µm mid	CFRP + SMA 50µm mid	CFRP + SMA 50µm mid	CFRP + SMA 50µm mid	CFRP + SMA 50µm mid
	CFRP + SMA 200µm mid	CFRP + SMA 200µm mid	CFRP + SMA 200µm mid	CFRP + SMA 200µm mid	CFRP + SMA 200µm mid
	CFRP + SMA 50µm top	CFRP + SMA 50µm top	CFRP + SMA 50µm top	CFRP + SMA 50µm top	CFRP + SMA 50µm top
Test objective	Check influence of wires when in austenite phase	Check influence of wires when in transition phase	Check influence of wires when in martensite phase	Evaluate recovery potential of SMA wires	Check influence of wires when in austenite phase

5.1 MANUFACTURING OF COUPONS

Through collaboration between UNN and tPE, two manufacturing methods were developed to investigate the effects of SMA within the composite panels through coupon testing. The first method involves placing the embroided SMA wires in the middle of the panels. The second method involves placing the embroided SMA wires onto the top layer of the panels. These two methods allow for a controlled and optimized placement of SMA within the composite panels, enabling further investigations into their impact on the overall performance and behaviour of the composite material. Further details on the material design as well as on the manufacturing methods can be found in deliverable D3.1.

For the mechanical tests, samples were cutted by using the waterjet technology. For a wide range of mechanical testing bending samples with a length of 100 mm and width of 15 mm as well as tensile specimens with the dimensions (l x w) 250 mm x 15 mm were cutted. Examples of the coupons cutted from both manufacturing methods can be seen in Figure 80.

Figure 80: Cutted samples using waterjet technology placed in the origin plate

5.2 MICROSTRUCTURAL CHARACTERIZATION

5.2.1 MICROSTRUCTURAL CHARACTERIZATION

The UNN further conducted microstructural analysis of SMA/CFRP, utilizing SEM with an accelerating voltage ranging from 10 to 20 kV. Notably, no pre-preparation was employed in this analysis, and EDX elemental mapping was used to confirm the presence and location of the SMA wires. Figure 81(a) shows one example of the typical cross-sectional microstructures of the SMA/CFRP composite. For this specific sample, 200 µm SMA wires were situated in the middle layer between 14-plies of the laminate, and they were evenly distributed along the length of the sample.

To enhance the damping and impact properties and to achieve optimal SMA's recovery upon heating within the CFRP, it is crucial to ensure efficient load transfer from the SMA to the surrounding matrix. Therefore, the adhesion or interfacial bonding between the SMA wire and the matrix plays a pivotal role. Figure 81(a) shows that at a higher magnification, the embroidery fabric and yarn can be clearly observed. However, there are noticeable gaps between the fibre and the matrix around the SMA wire, indicating the occurrence of interfacial debonding between SMA/matrix. This debonding explains the decline in the mechanical properties of the composite which we have obtained. It's worth noting that improving the bonding or adhesion levels needs to improve the surface properties of the wire, particularly its roughness, and increase the amount of PA6 in the SMA/fabric layer to enhance the interfacial bonding. Figure 81(b) presents an EDX elemental mapping which demonstrates the presence of nickel and titanium elements from NITINOL, along with a minimal amount of oxygen content.

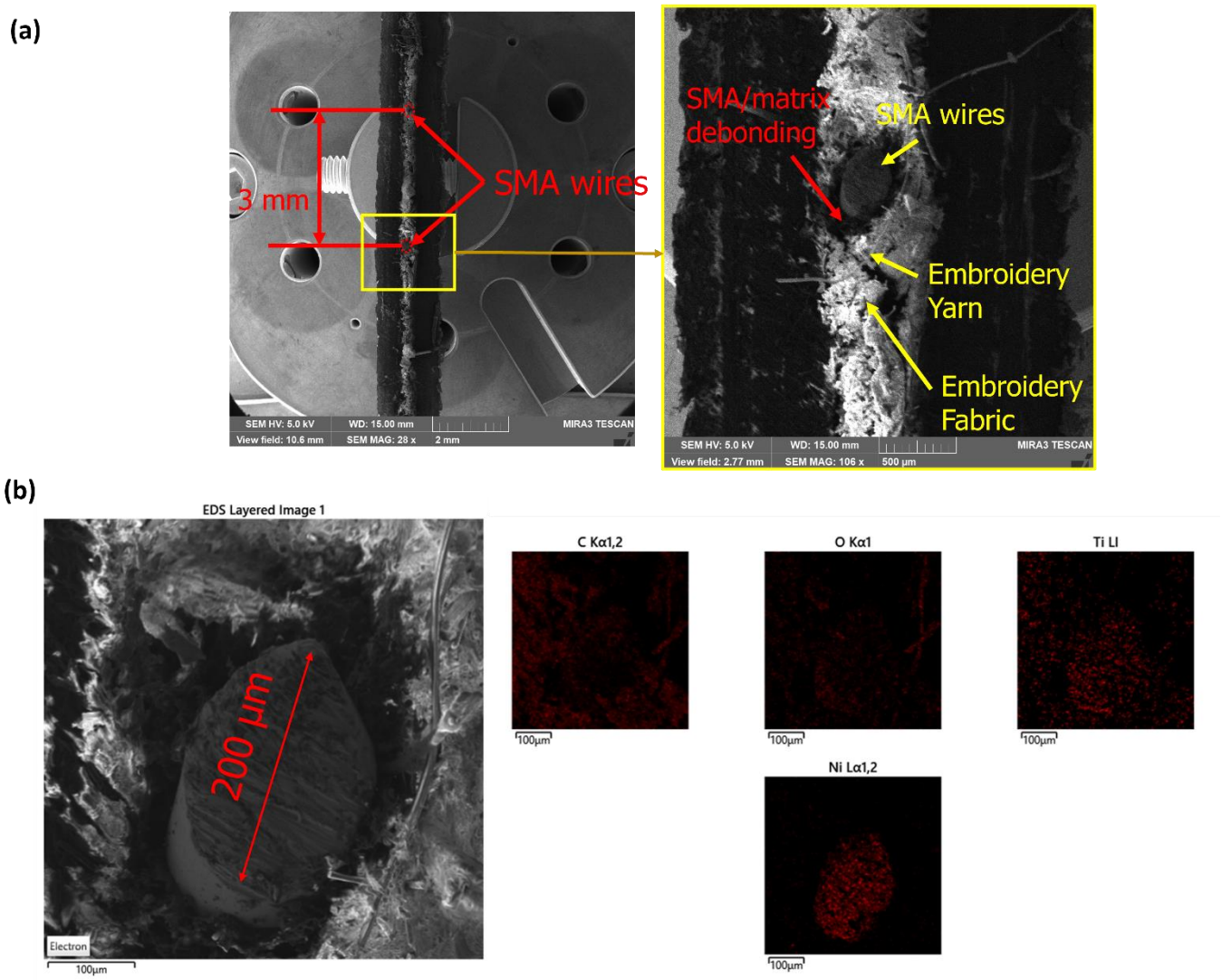

Figure 81. SEM image for the SMA/CFRP composites where the SMA wires lays in the middle layer of the composites. (a) Cross sectional image with a zoom in view, (b) EDX elemental map.

5.2.2 STRUCTURE AND SURFACE CHARACTERIZATION

Figure 82(a) exhibits the example of XRD profiles of the SMA/CFRP samples. In this specific sample with a dimension of 20 x 20 mm^2, the SMA wires are positioned on the top surface, above the 14-ply CFRP laminates. Within the XRD profile, discernible diffraction peaks corresponding to PA6 α phase of (200) and α (002) are observed at approximately 2θ = 20.23° and 23.37°, respectively. Notably, there are no discernible peaks indicative of the SMA wires, due to their low quantity.

The optical scattering test was conducted using the laser interferometer at Northumbria University. One of the typical examples are presented in Figure 82(b). However, the laser interferometer failed to provide sufficient scattering and morphology information. This is probably due to the rough or dark nature of the sample surface. In order to address this limitation, surface profile mapping via a Scanning Probe Microscope (SPM) or Atomic Force Microscope (AFM) was employed. One of the typical examples is shown in Figure 82(c). This SPM analysis revealed that the surface possesses a maximum roughness value of approximately 1.5 nm.

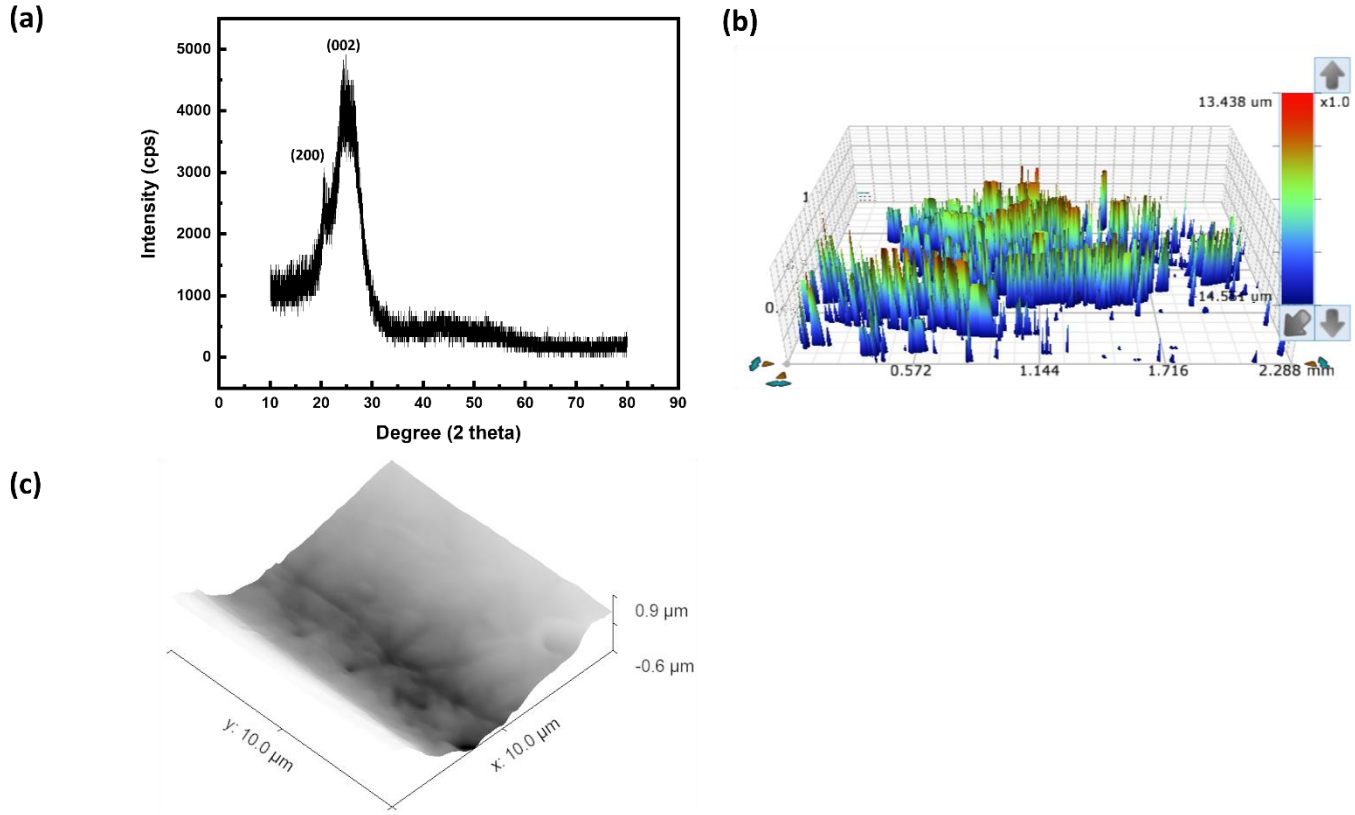

Figure 82. SMA/CFRP composites Structural and surface characterisations results, (a) X-ray diffraction profile, (b) Scattering by laser interferometer, and (c) Scanning probe microscope SPM surface profile.

5.3 BENDING TESTS

5.3.1 TEST PROCEDURE

Similar to the bending tests carried out on TP/CFRP coupons, three-point bending tests on SMA/CFRP coupons were carried out according to the prescriptions of the standard ISO 14125 [20]. Consequently, coupons of dimensions 100 mm x 15 mm x 2 mm were produced by tPE for this purpose. In all four test configurations (see Table 6 above), the span between supports was set at 35 mm, and support cylinders of diameter 4 mm were used. In the coupon that has the wires placed at the top, the wires were put in such a way that they are subjected

to tensile stresses during the tests. In the other configurations containing fibres, the positioning of the coupons is not critical as the wires are placed in the neutral fibre of the material.

A non-standard testing procedure was defined to check the effect of the activation of the SMA wires on the overall composite behaviour. The steps followed for this test were the following:

1. At room temperature, a displacement of 2 mm is applied to the coupons. This entails applying a force on the material that is well below its limits, but enough to detect and measure any changes that may occur during or after the activation of the wires.
2. When force and displacement values are stable for a minute, then temperature is steadily and slowly increased up to 110ºC without stops. Displacement is fixed at 2 mm during all the process, and force signal is tracked.
3. Coupons are kept at 110ºC until all test variables are stable. Then, the test is finished.

For the tests at temperatures other than RT, a climatic chamber (Figure 83) was employed.

Figure 83: Climatic chamber used at Cidaut in SMA/CFRP tests.

5.3.2 TEST RESULTS

Results at room temperature (austenite phase of the SMA wires)

The aspect of the tested coupons after failure is shown in Figure 84. The associated force-displacement and stress-strain curves are depicted for all configurations in Figure 85 and Figure 86, respectively.

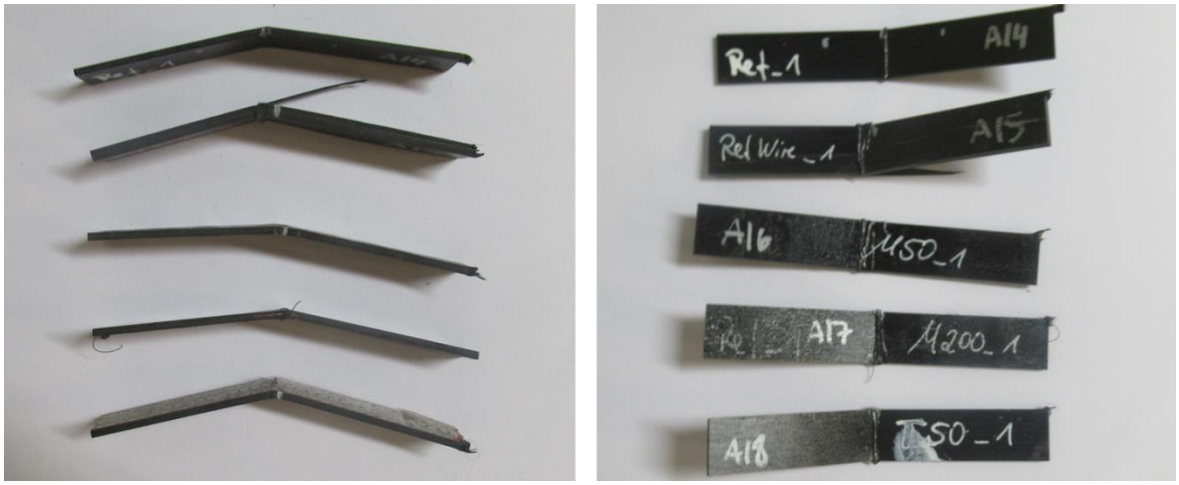

Figure 84: Aspect of SMA/CFRP coupons after three-point bending tests @ RT.

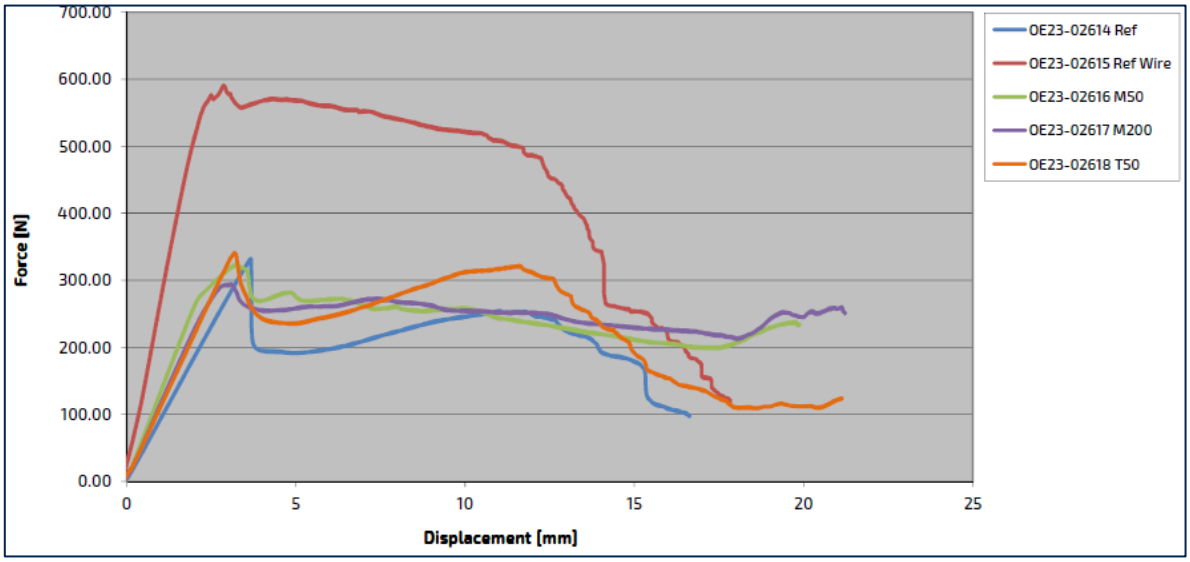

Figure 85: Force-displacement curves of all configurations tested in bending mode @ RT.

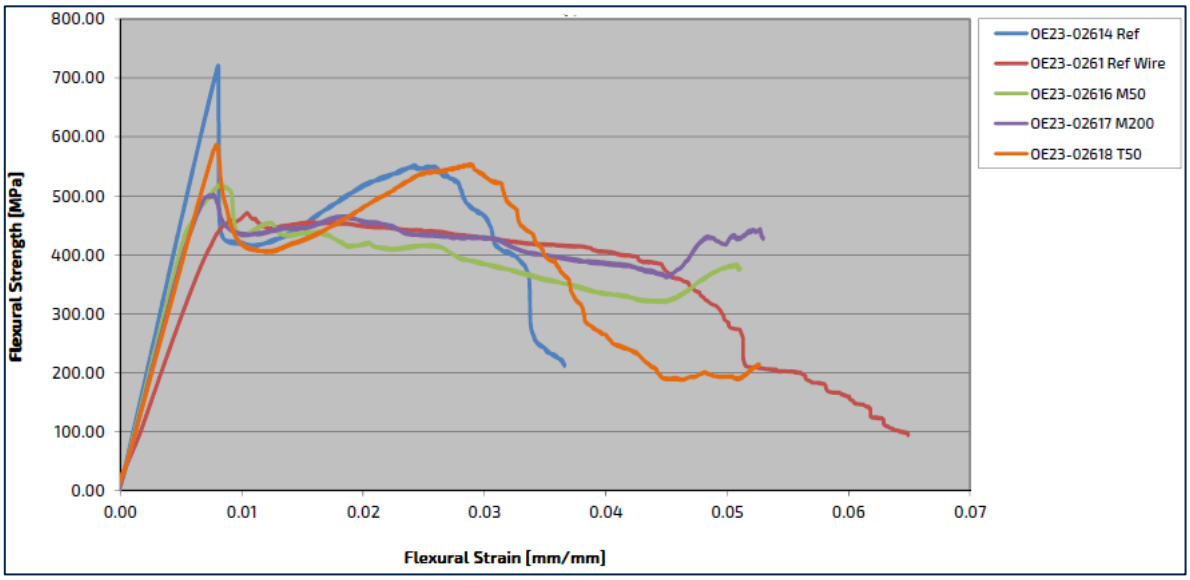

Figure 86: Stress-strain curves of all configurations tested in bending mode @ RT

Looking at the figures, it can be seen that placing the wires at the top of the CFRP does not entail any significant change in the behavior of the material, while embedding them within the CFRP does affect significantly the outcome of the test, regardless of the type and dimensions of the wires employed. Regarding the Young modulus, there is a slight drop in the values obtained for the SMA/CFRP coupons with respect to the CFRP reference, and even a more evident drop is noticed when the non-SMA wires are employed.

Results at 75ºC (transition phase of the SMA wires)

The aspect of the tested coupons after failure is shown in Figure 87. The associated force-displacement and stress-strain curves are depicted for all configurations in Figure 88 and Figure 89, respectively.

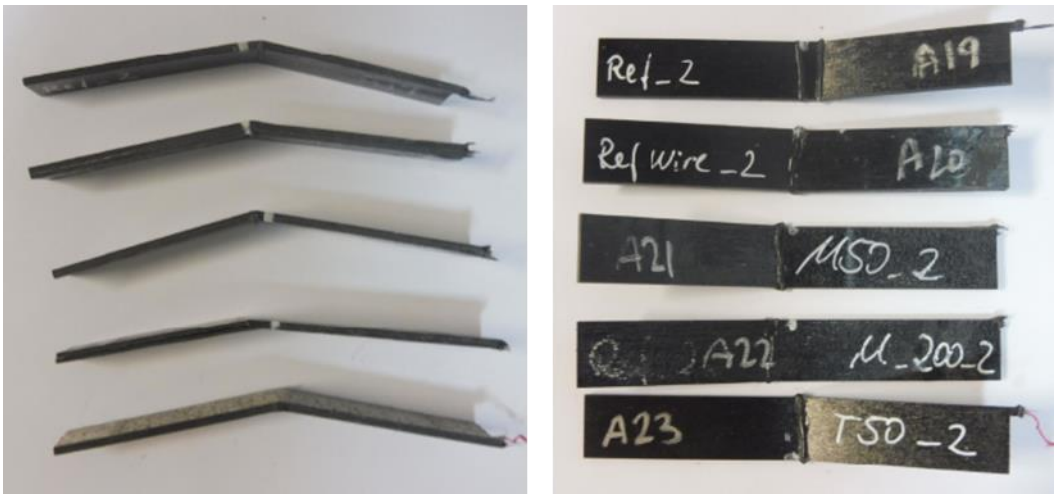

Figure 87: Aspect of SMA/CFRP coupons after three-point bending tests @ 75ºC.

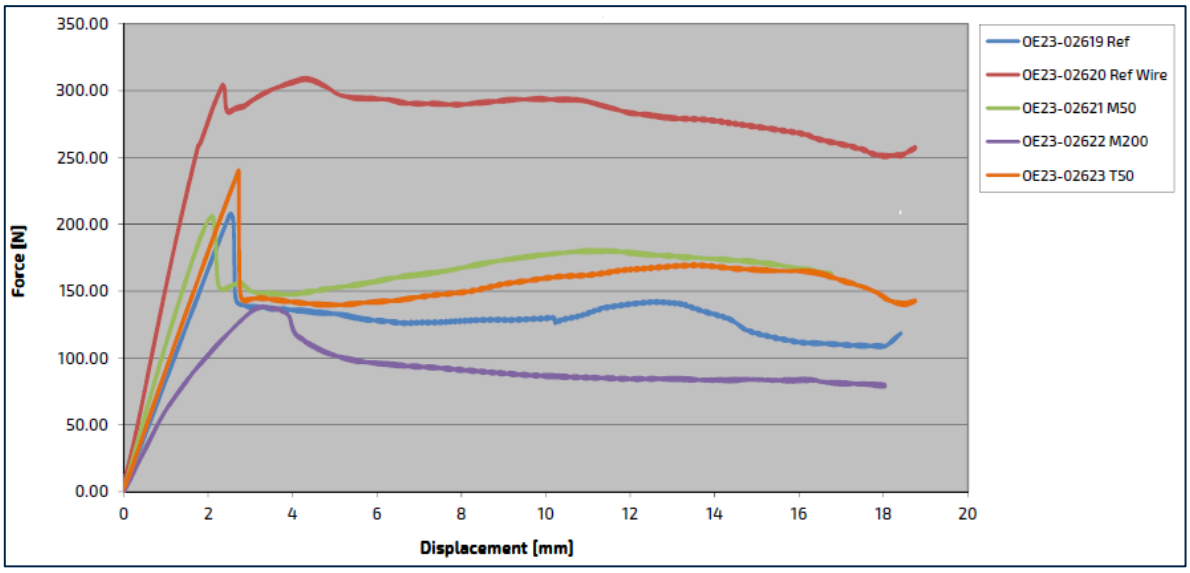

Figure 88: Force-displacement curves of all configurations tested in bending mode @75ºC.

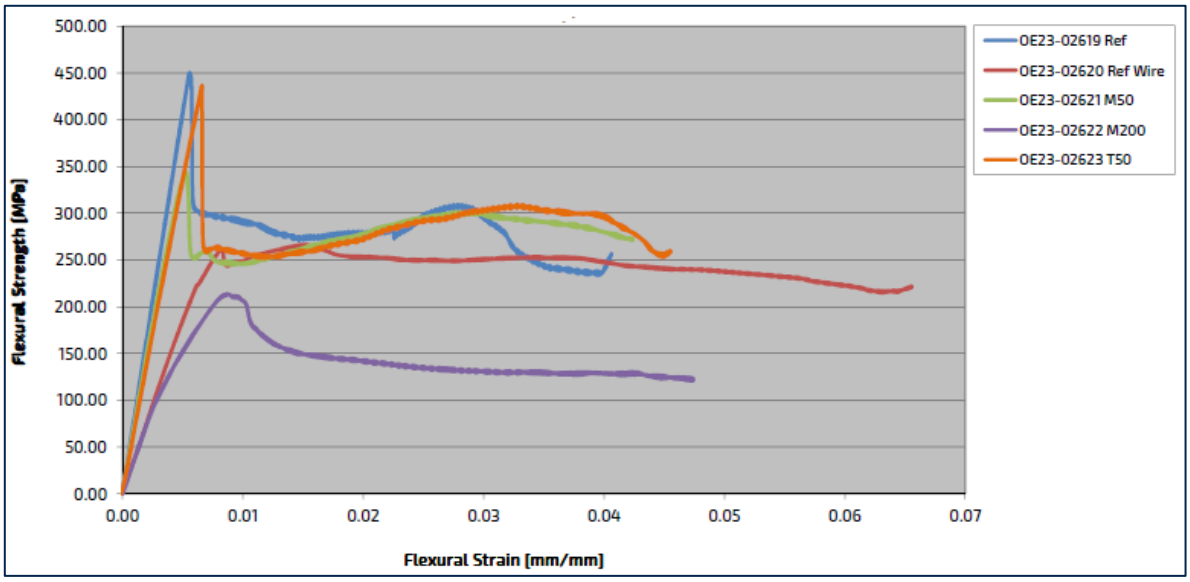

Figure 89: Stress-strain curves of all configurations tested in bending mode @75ºC.

In this test, the reference material and the coupons with 50µm wires (either placed at the top or in the middle) show similar behavior in qualitative terms, and also similar amount of strength was reached. The coupon with non-SMA wires showed worse behavior, and also the stress evolution is different due to the higher impact of the wires used on the behavior. Similar behavior is detected in the coupon with 200µm wires, what is therefore associated to the fact that bigger wires can more effectively modify the behavior of the CFRP. Nevertheless, in this last case results were greatly affected by the appearance of early delamination in the coupon, very likely motivated by the different thermal expansion coefficients of the polyamide and the SMA wires that led to premature failure. This phenomenon is considered a sign of non-optimal embedment of the 200µm wires during the manufacturing process. A detail of the delamination observed is presented in Figure 90.

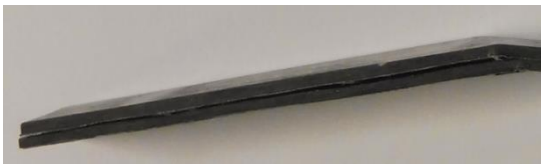

Figure 90: Early delamination observed in the coupon with 200µm wires.

Results at 100ºC (martensite phase of the SMA wires)

The aspect of the tested coupons after failure is shown in Figure 91. The associated force-displacement and stress-strain curves are depicted for all configurations in Figure 92 and Figure 93, respectively.

Figure 91: Aspect of SMA/CFRP coupons after three-point bending tests @ 100ºC.

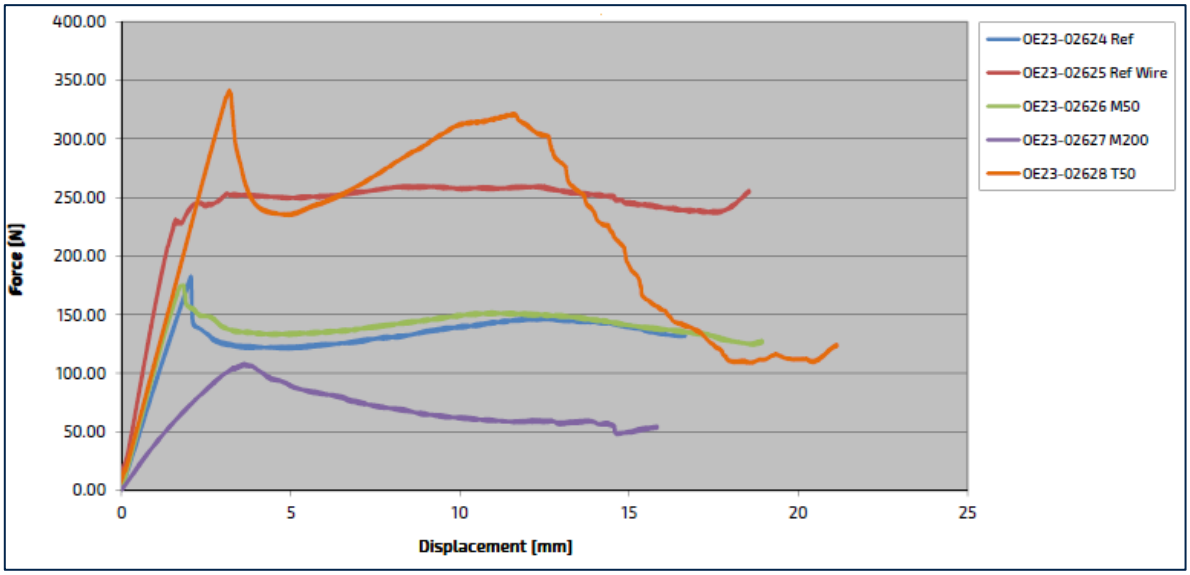

Figure 92: Force-displacement curves of all configurations tested in bending mode @100ºC.

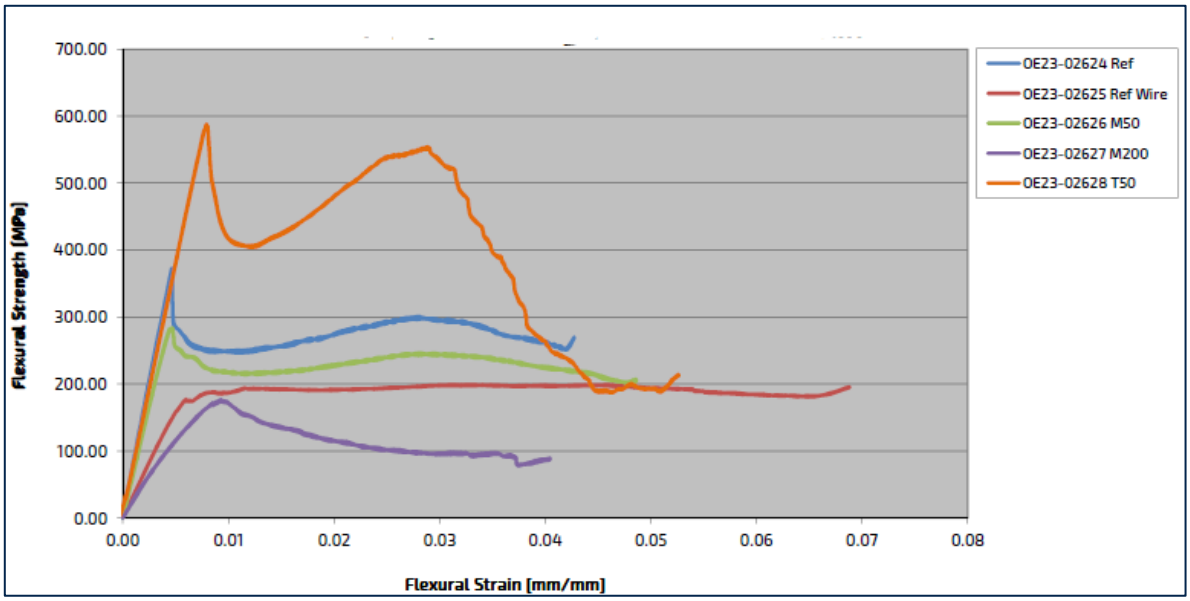

Figure 93: Stress-strain curves of all configurations tested in bending mode @100ºC.

At high temperature (100ºC) it is important to remark that the glass transition temperature (T_g) of the polyamide is surpassed, and therefore this major microstructural change may affect the results obtained. In qualitative terms, the behavior of the coupons with 50µm diameters is somewhat similar to that of the CFRP reference. The better performance is obtained when the wires are placed at the top, because that is the configuration in which the wires are undergoing the highest flexural loads, and therefore they are able to compensate at least to some extent the loss of properties associated to the softening of the polyamide. Again, early delamination was observed in the coupon with the 200µm wires embedded (Figure 94), confirming the fact that a further adjustment of the manufacturing process parameters is needed in order to allow a better understanding of the impact of these wires in the overall SMA/CFRP material behavior.

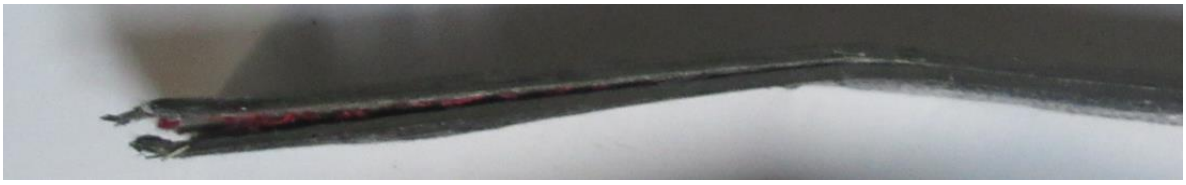

Figure 94: Delamination observed in the coupon with 200µm wires.

Bending @ RT + heating up to 110ºC

The aspect of the tested coupons after the test is shown in Figure 95.

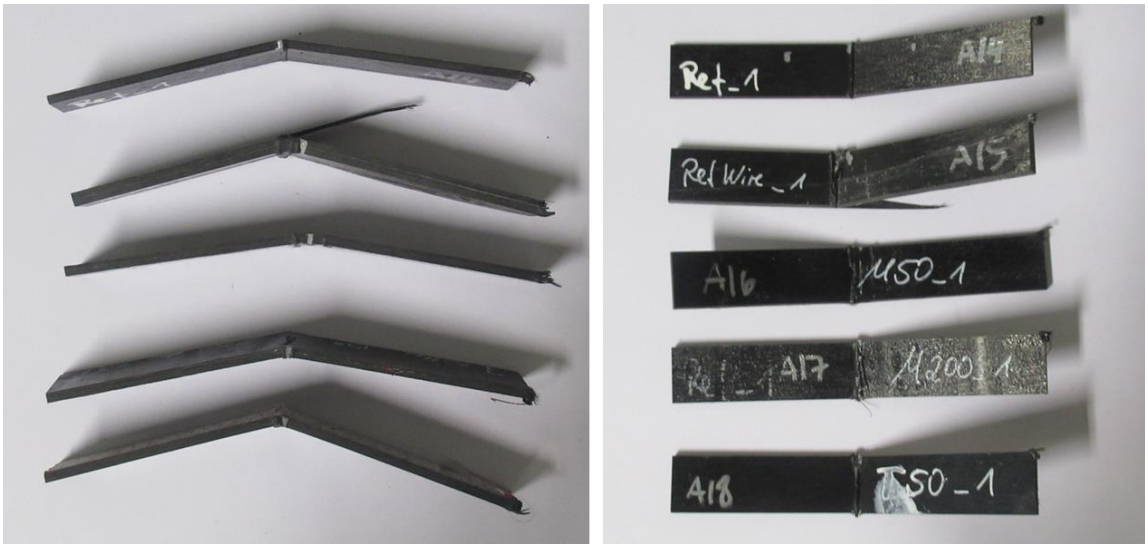

Figure 95: Aspect of SMA/CFRP coupons after bending + heating test.

In Figure 96, the temperature vs time curves for the different coupons are shown, in which it can be seen that there is a relatively short period of heating up the coupons, after which temperature is kept constant for a long time until all test parameters, and especially the force measured, remains stable. This way, it is ensured that the phase transformation of the SMA wires is effectively occurring, since thermocouples for temperature measurement were adhered to the surface of the coupons.

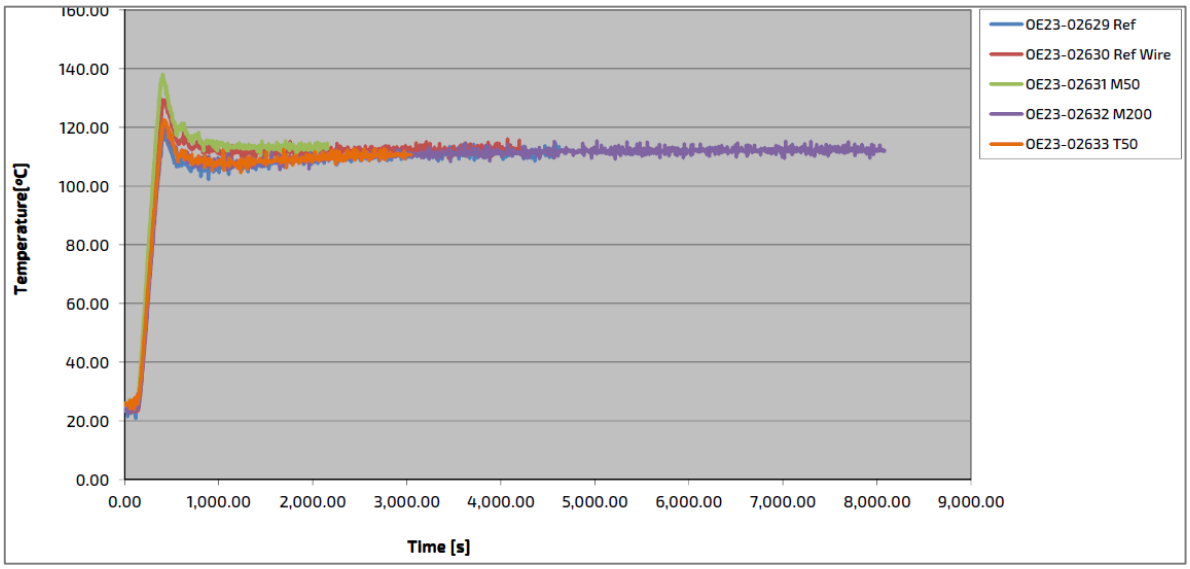

Figure 96: Temperature-time curves of all configurations tested.

Also stress-strain curves were registered (Figure 97). As expected, the limited amount of deflection employed means that no failure is observed in any of the coupons, even though slightly different maximum stress and strain values are measured for each coupon. During the heating stage and the subsequent constant temperature period, a progressive drop in the stress occurs, which is attributed to the softening on the polymer.

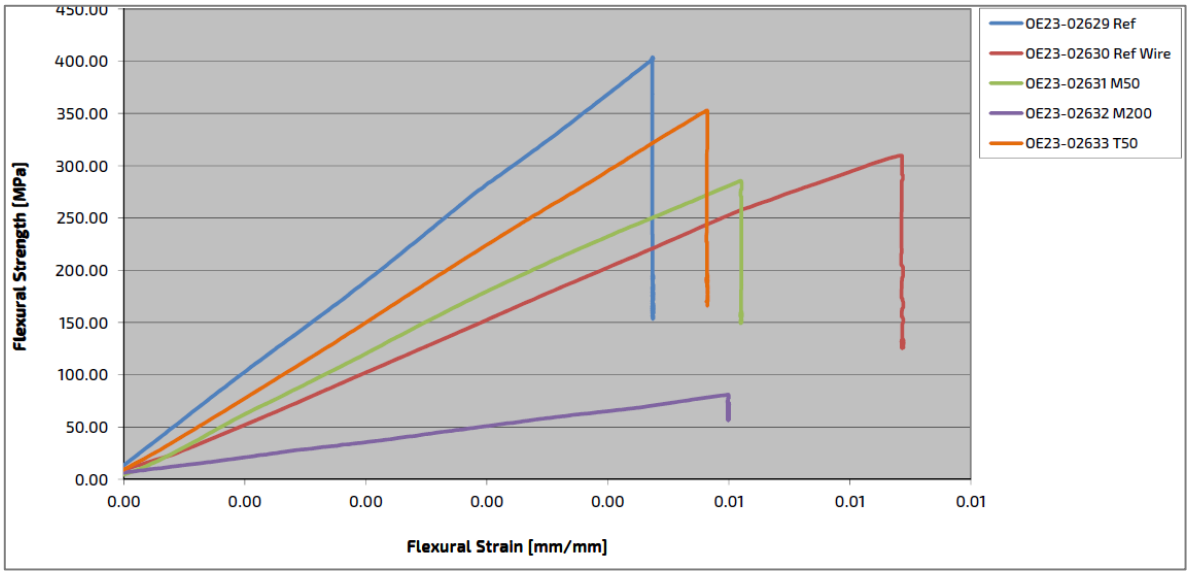

Figure 97: Stress-strain curves of all configurations tested.

Finally, the impact of the activation of the SMA wires on the behavior of the material can be preliminarily interpreted looking at the force-temperature curves presented in Figure 98. According to the properties of the matrix material (glass transition temperature around 55-70ºC) and the SMA wires (phase transition in the range 60-80ºC), all major changes should be detected in the 60-90ºC approximately. There are almost no differences between the reference material (blue curve) and the coupon with 50µm wires placed at the top (orange curve), while a less abrupt force drop is observed in the coupon with 50µm wires placed in the middle (green curve), . This effect is even more evident in the coupon with 200µm wires placed in the middle (purple curve), in which force remains approximately constant during and after the heating period. This might mean that the SMA wires are at least partially capable of compensating the softening of the matrix material, in contrast with the use non-SMA wires (red curve), that are not capable of mitigating this softening effect. In any case, the two physical processes (softening of the polyamide and activation of the SMA wires) are happening simultaneously, therefore the isolated effect of the activation of the wires could not be evaluated using this test.

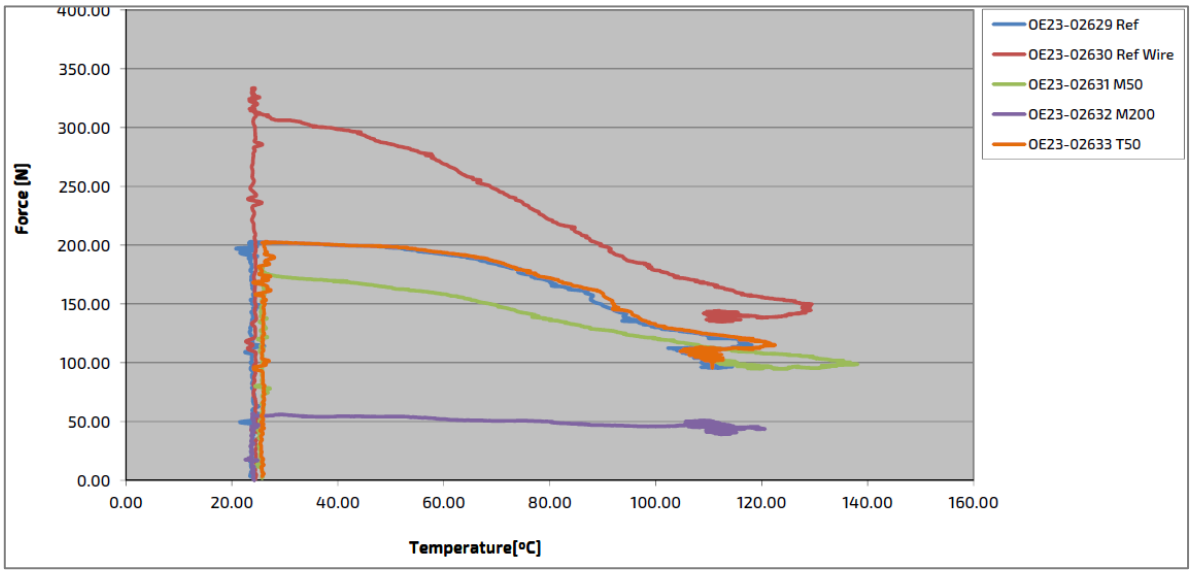

Figure 98: Force-temperature curves of all configurations tested.

5.4 TENSILE TEST

5.4.1 TEST PROCEDURE

Quasi-static tensile tests on SMA/CFRP material at room temperature were conducted in a similar fashion to tensile tests carried out on TP/CFRP material already described in section 4.3. ASTM D3039 was used as reference standard, but in this case the recommended coupon dimensions were modified because of the limitations of the manufacturing equipment. Hence, coupons of 250 mm x 15 mm x 2 mm were provided by tPE for testing. Coupons were tabbed to ensure a smooth load transfer from the machine to the coupons and therefore avoid undesired failure modes as much as possible. To this end, one of the tabs' ends was cut at 45º to minimize stress concentrations in the transition area. The coupons are shown in Figure 99.

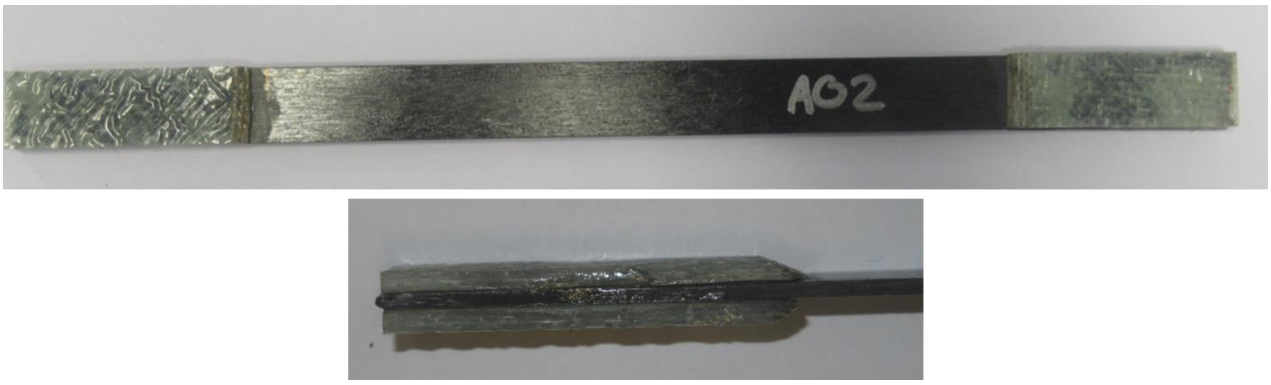

Figure 99: Example of a tensile SMA/CFRP coupon. Top: full coupon. Bottom: detail of the tab area.

5.4.2 TEST RESULTS

The aspect of the tested coupons after failure is shown in Figure 100. The associated force-displacement and stress-strain curves are depicted for all configurations in Figure 101 and Figure 102, respectively.

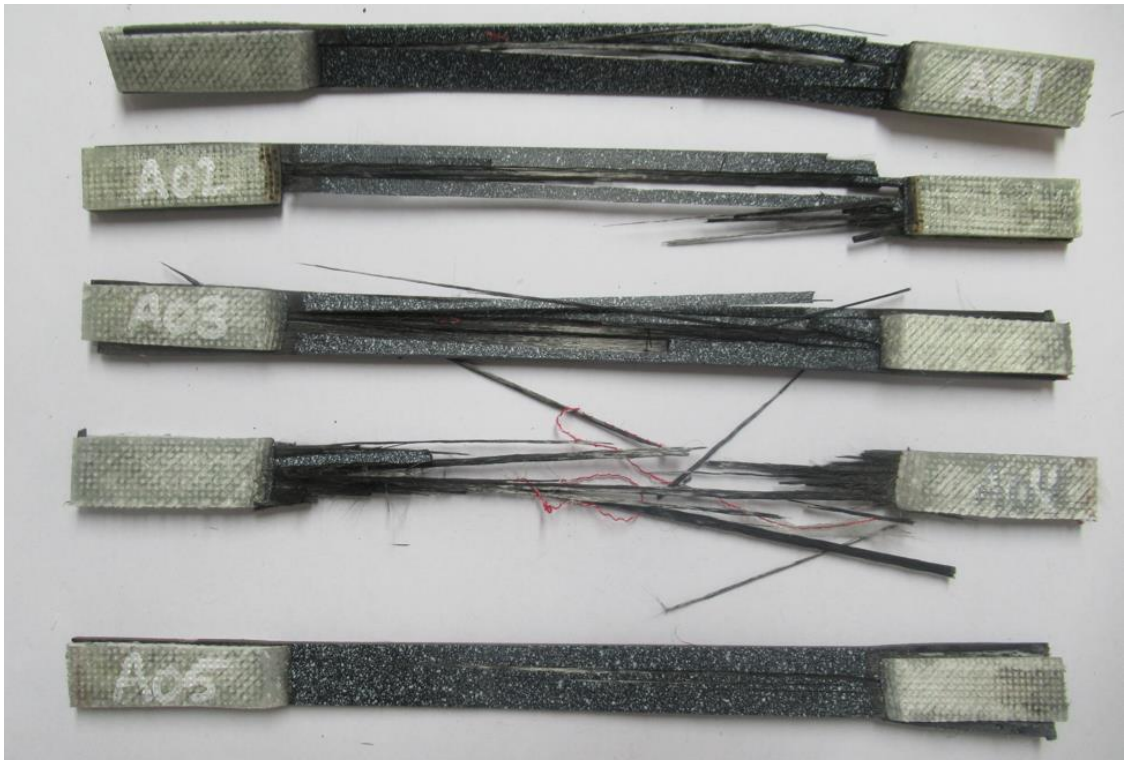

Figure 100: Aspect of SMA/CFRP coupons after QS tensile test.

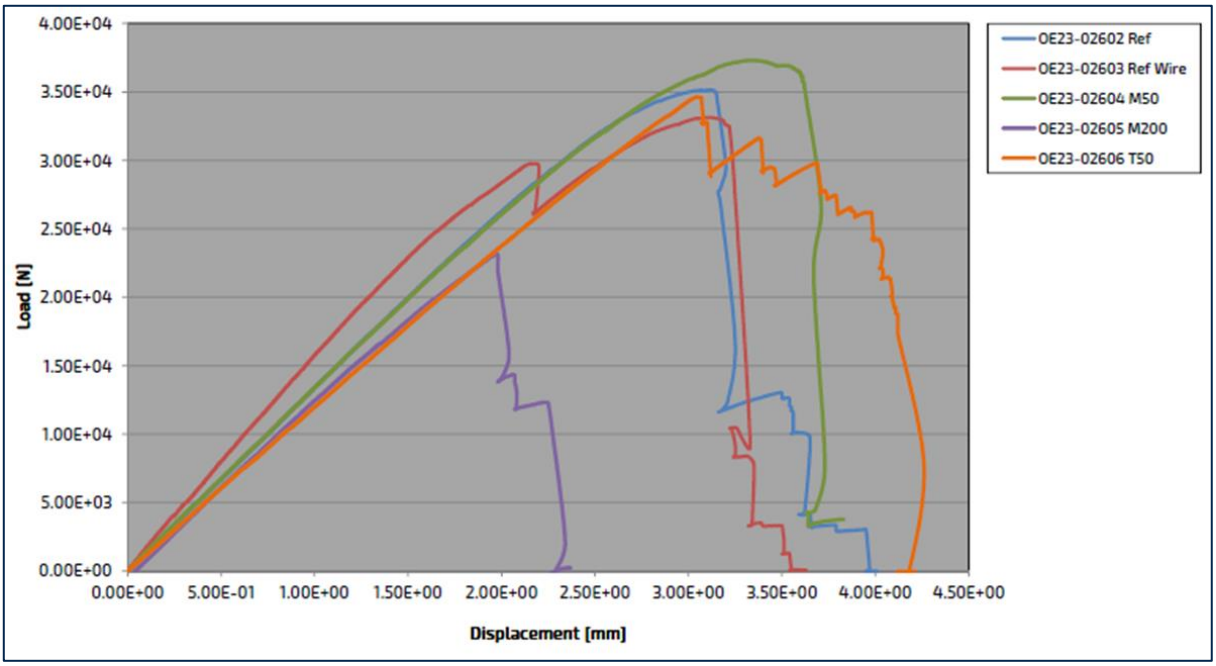

Figure 101: Force-displacement curves of all configurations tested in tensile mode @ RT.

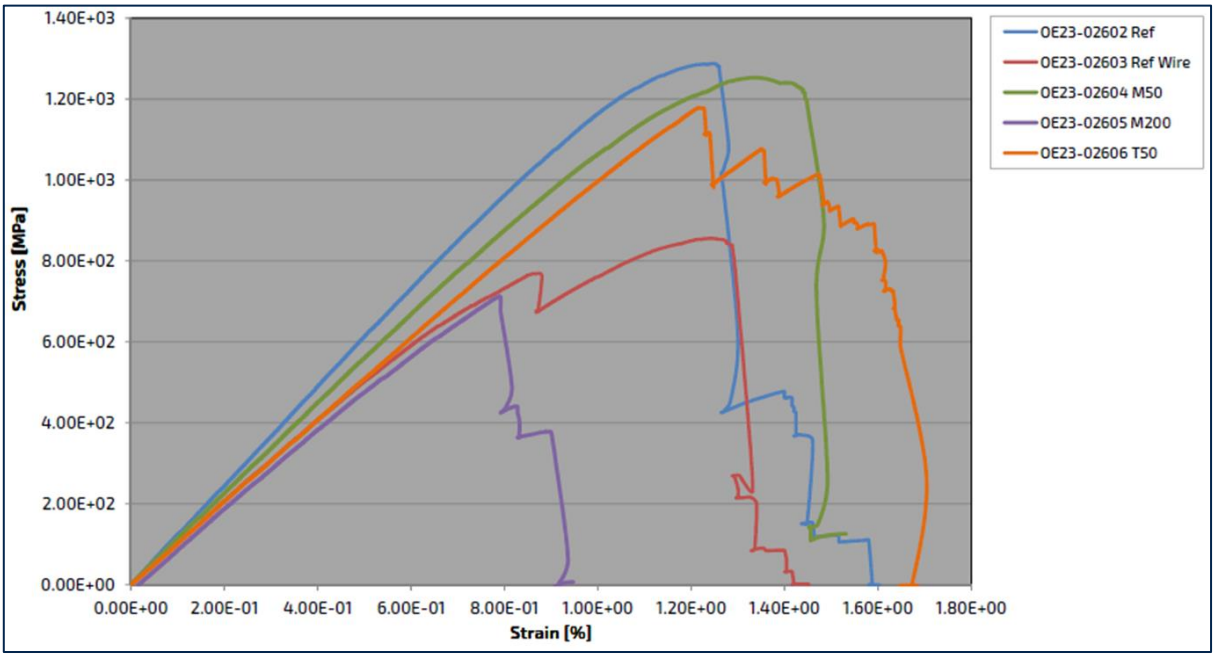

Figure 102: Stress-strain curves of all configurations tested in tensile mode @ RT.

The validity of the proposed geometry for this test and material is demonstrated looking at the ultimate stress values obtained for the reference material (around 1300 MPa), which are comparable to the ones obtained in the QS tensile tests of the CFRP with the recommended dimensions (see section 4.3). Also failure mode (longitudinal) is consistent across all coupons.

In Figure 102 it can be seen that 50µm wires (green and orange curves) outperform 200µm wires (purple curve), regardless of their positioning within the coupons. There is not a significant modification of the Young modulus of the material in any configuration. The coupon with 200µm wires embedded showed premature failure, at the lowest stress and strain of all coupons, which is considered a signal of worse integration of the wires within the polyamide.

5.5 DISCUSSION ON TEST RESULTS

A series of characterization tests on SMA/CFRP coupons was carried out with two main objectives: assess the integration of the SMA wires in the CFRP material, and evaluate the potential impact of the activation of the SMA wires in the overall behaviour of the material. To this end, bending and tensile tests were carried out, and also different testing temperatures were defined, in order to be able to check the behaviour in different states of both the SMA wires and the CFRP material (here especially the polyamide matrix). A specific test method was designed to check the activation effect of the SMA wires. Different concepts of SMA/CFRP materials were tested.

The results obtained were greatly dependent on the SMA/CFRP concept tested. Using 200µm wires seems promising in the sense that bigger wires have more remarkable impact on the material behaviour, nevertheless in this campaign the integration of the 200µm wires within the CFRP was not optimal and led to premature failure of the coupons due to delamination, especially at high temperatures, and also in the tensile test. This observations were confirmed in the microstructural analysis, where remarkable gaps were found between the wires and the matrix material. The effect of 50µm wires depended on the placement of the wires, although it is more moderate than the effect of 200µm wires in any case. If placed at the top, the behaviour is essentially similar to the CFRP reference. If placed in the middle, mild modifications in the material behaviour are seen.

Therefore, it is concluded that further optimization of the material design and the manufacturing process parameters are still needed to get the maximum performance of the SMA/CFRP material.

6. HYBRID MATERIAL AL/CFRP CHARACTERIZATION

For the use of two different materials in hybrid components, their joining quality must be investigated. In the case of a two-dimensional bond, the shear strength of the connection is of particular interest. In addition, the influence of temperature and moisture on the bonding interface must be analysed.

6.1 MANUFACTURING OF COUPONS

As described in Deliverable D3.1, a good bond to the composite (CFRP-PA6) was established with the primer Vestmelt Hylink® applied to the aluminum (see Figure 103).

Figure 103: Hybrid laminates: result with the Vestamelt Hylink® Primer

The pressed hybrid laminates were cut with waterjet cutting into standard specimens. After cutting, no delamination of the joining partners was observed, so that the next step was conditioning followed by testing (see Figure 104).

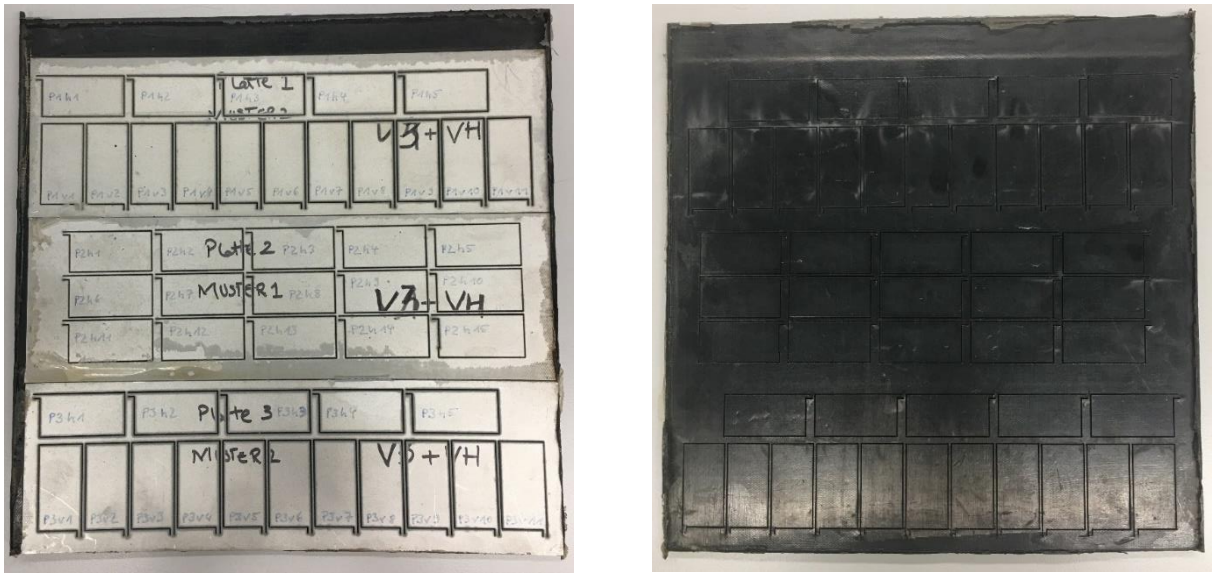

Figure 104: Cutting pattern of the specimen (front- and backside)

The layup was chosen to be quasi-isotropic. 13 layers (thickness of the single layer 0.15 mm) were used to achieve a lamina thickness of 2 mm (see Figure 105).

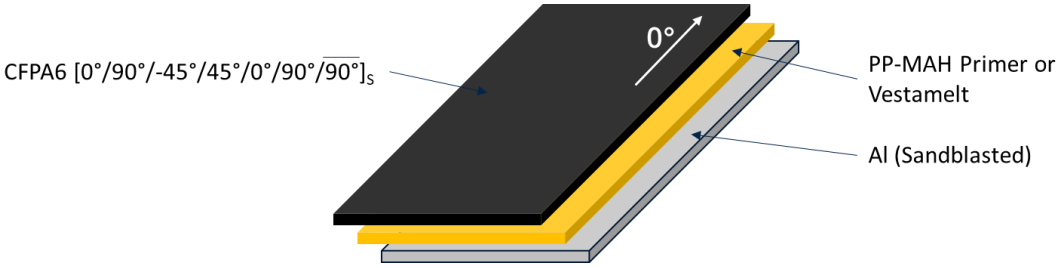

Figure 105: Layer stack-up

Aluminum strips supplied by ASAS had a width of 80 mm. Therefore, 3 of these plates had to be placed side by side in the press tool. Since there is a significant difference in the coefficient of thermal expansion between aluminum and the composite, the three aluminum plates were inserted with the shorter edge is aligned in the direction of the fiber direction of the last fiber composite layer (see Figure 106). This configuration would result in less temperature induced strain at the bond interface.

Figure 106: Placement of aluminum strips according to the last layer direction

Numbering: Horizontal and vertical specimens were optimally placed in the cutting pattern for efficient utilization of the hybrid plate material. These specimens were differentiated in the naming convention by using suffix "h", which stands for horizontal and "v", which stands for vertical according to the 0°-direction of the fibers. Since three aluminum plates were pressed into one plate, the beginning of the designation P1, P2, and P3 stand for plate 1, plate 2, and plate 3, respectively. The last number of the coding describes the consecutive specimen numbering in this group (see Figure 107).

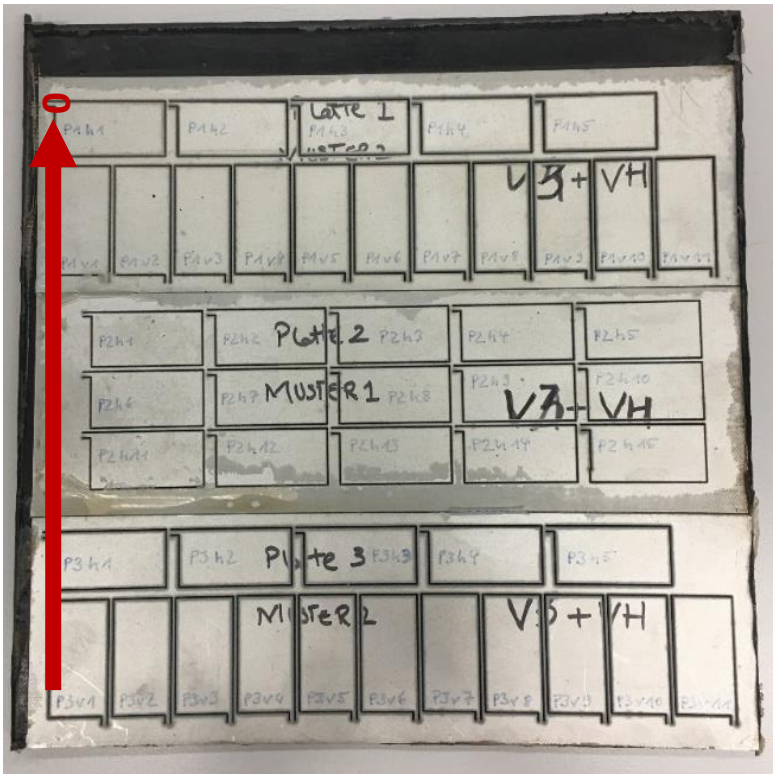

Figure 107. Numbering of the specimen (blue)

A few samples were removed from the cut plate (see Figure 108) and reserved for the testing as unconditioned specimens (reference tests). All specimens that can still be seen in the plate were tested in the PV 1200 climate change test.

Figure 108. Tested specimens in the PV 1200

6.2 MICROSTRUCTURAL CHARACTERIZATION

The UNN further conducted microstructural analysis of the hybrid Al/CFRP material, employing SEM as an imaging technique. Before the imaging process, a platinum coater was applied to deposit a conductive layer on the sample's cross-sectional surface to enhance the conductivity of the layers. Figure 109 shows one of the many typical microstructures or morphology of this hybrid material. As depicted in Figure 109(a), we can see the Al6063 layer located in the upper portion of the image, while the lower part is comprised of CFRP. Notably, there are no observable signs of debonding or any discernible volume of void defects. For further verification of the microstructural details, EDX image mapping was conducted, and a typical image is presented in Figure 109(b).

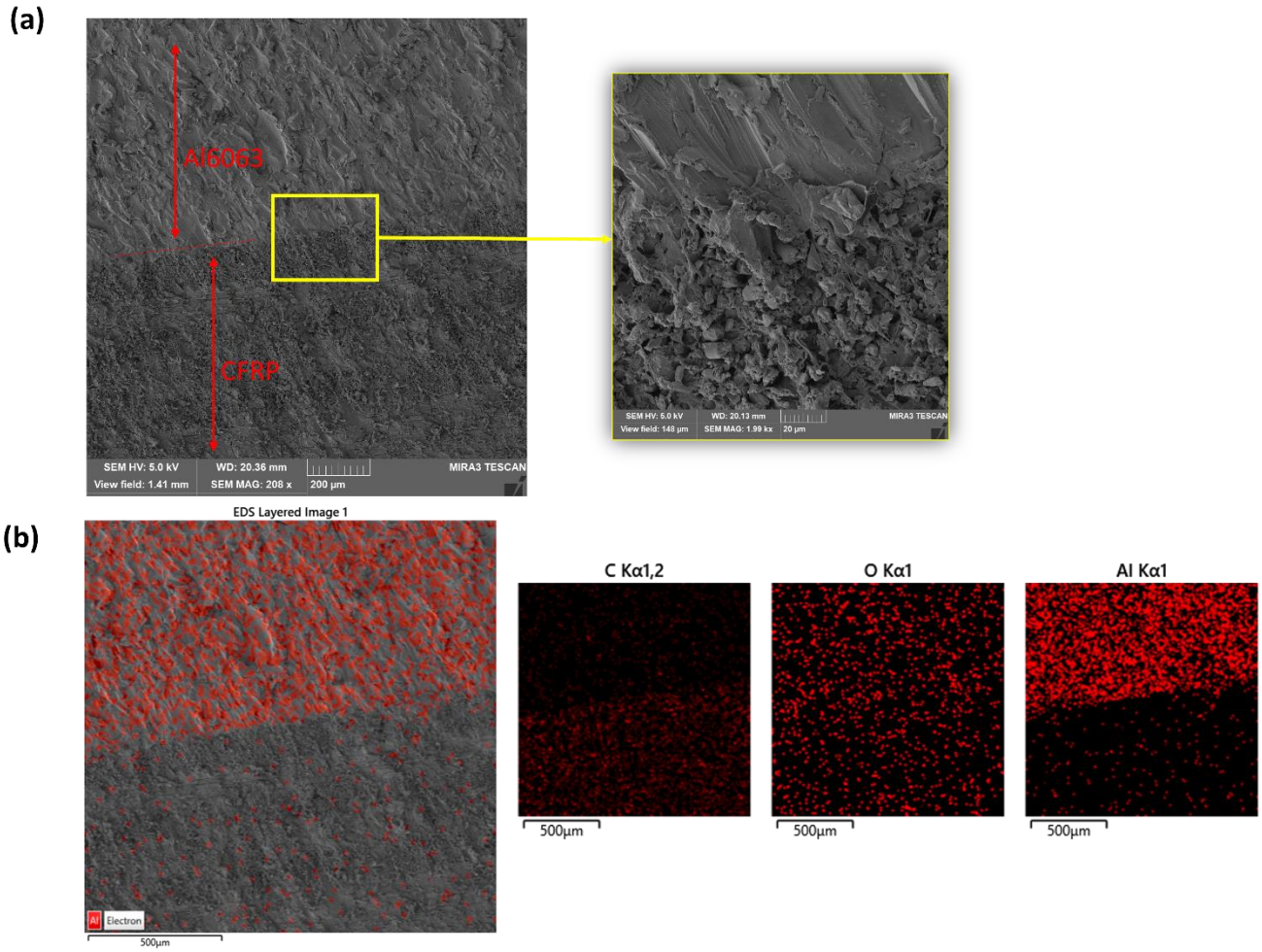

Figure 109. SEM image for the hybrid Al/CFRP composites (a) Cross-sectional image with a zoom in view, (b) EDX elemental map.

Figure 110(a) exhibits the XRD profile of the Al/CFRP hybrid composite, which has a cross-sectional dimension of 20*20 mm². The diffraction peaks of the PA6 α phases (200) and (002) are observed at approximately 2θ = 20.23° and 25.7°, respectively. The optical scattering test was conducted using the laser interferometer at UNN, and one of the typical results is presented in Figure 110(b). However, the laser interferometer failed to provide sufficient scattering or details. This is probably due to the rough or dark nature of the sample surface. The creep tests using DMA equipment did not obtain any good results, mainly because the Al alloy sample's high melting temperature and limit of equipment's maximum testing temperature. Using the DMA testing, it is expected for the hybrid material to have intermediate damping properties between the Al, and CFRP materials and increase in the T_g compared to the CFRP [21].

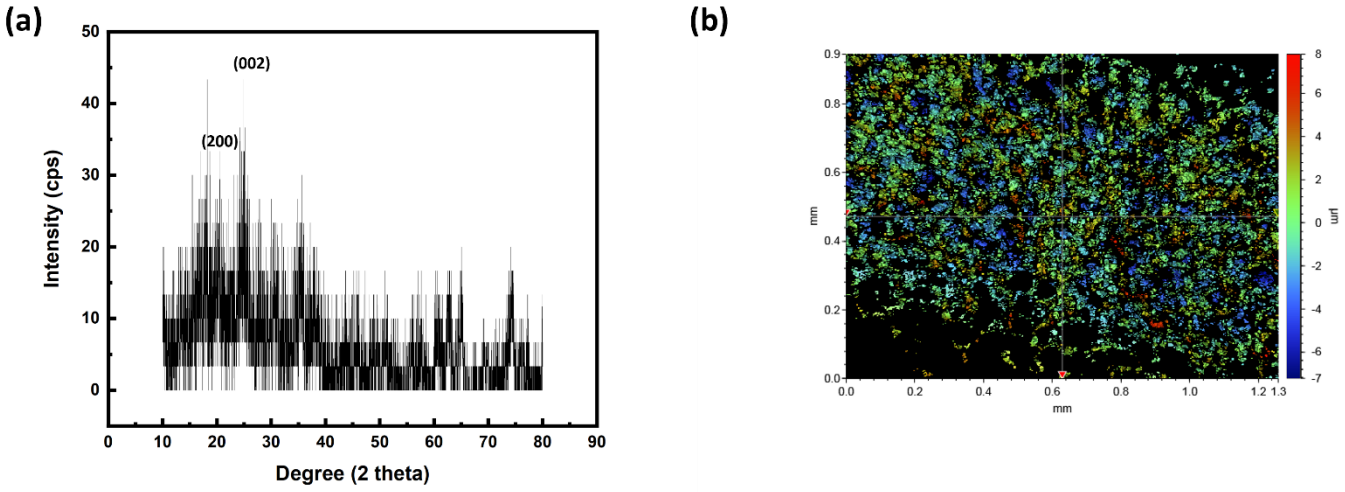

Figure 110. Hybrid composites Structural and surface characterisations results, (a) X-ray diffraction profile, (b) Scattering by laser interferometer.

6.3 AGEING + SHORT BEAM THREE POINT BENDING TESTS

6.3.1 TEST PROCEDURE

Climate Change Test

The carbon fibres contained in the composite material would contribute to corrosion of the metal if it came into direct contact with the aluminium. Therefore, it is necessary that FRA prepares the samples for coupon level tests, to determine the durability of the Al/composite hybrids under long term climatic and cyclic loading exposures. Volkswagen's PV 1200 climate change test was found to be the most appropriate for this purpose since it has been in practice in the automotive industry and defines the temperature and humidity conditions according to service conditions of a vehicle [22]. The test specification describes a cyclic climate change test on vehicle parts. One cycle (see Figure 111) lasts for 720 min (12 h) and comprises the following temperature and humidity profiles:

- 60 min heating phase to +80 °C and 80 % rel. humidity,
- 240 min holding time at +80 °C and 80 % rel. humidity,
- 120 min cooling phase to -40 °C, when freezing point is reached: approx. 30 % rel. humidity, the air humidity remains unregulated as of T < 0 °C (depending on the system, humidity regulation can also be suspended as of T < 10 °C),
- 240 min holding time at -40 °C, air humidity remains uncontrolled,
- 60 min heating phase to +23 °C, rel. humidity is regulated to 30 % as of T = 0 °C

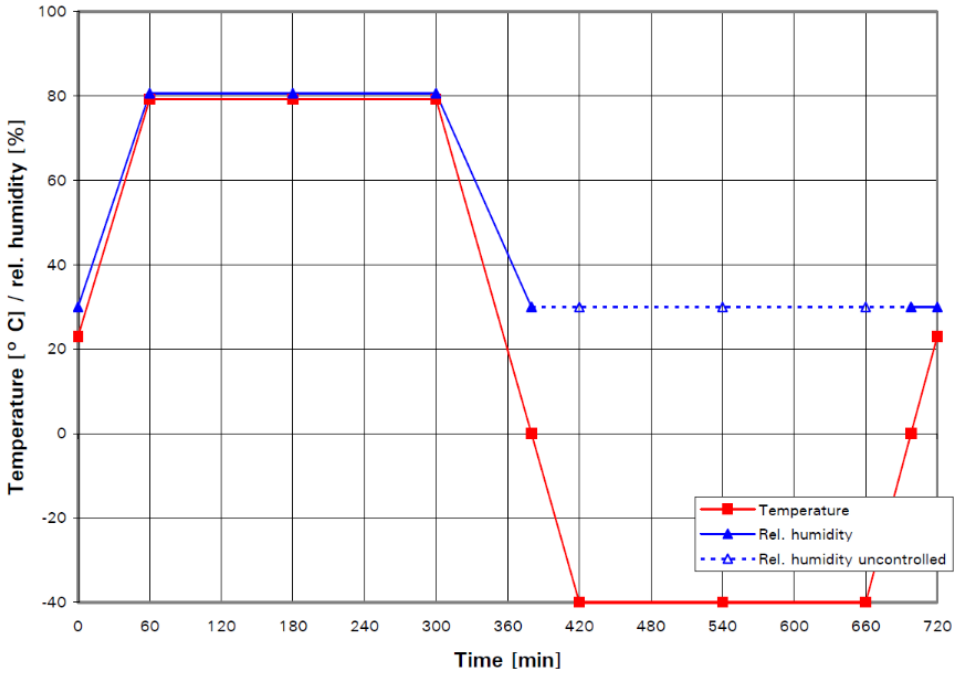

Figure 111: Test cycle for PV 1200

Short Beam Method for apparent Interlaminar Shear Strength

In aluminium/CFRP hybrid laminates, there exists essentially an interface between the two materials. With an early failure of this interface, the potential of the multi-material cannot be fully exploited. Therefore, it is recommended to assess the strength of this interface – the so-called interlaminar shear strength (ILSS). Testing standard DIN EN ISO 14130 [23] specifies a method for determining the apparent interlaminar shear strength (ILSS) of fibre-reinforced plastics using the short-beam three-point bending method (Figure 112).

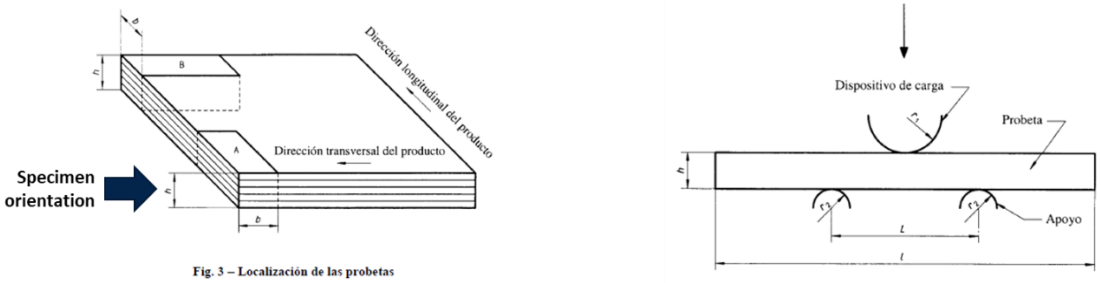

Figure 112. Short beam bending test (DIN EN ISO 14130)

In the SALIENT project, the materials provided by tPE and ASAŞ were used to fabricate hybrid sheets. Since the Al plate provided by ASAS had a thickness of 2 mm, a composite laminate of the same thickness had to be applied, i.e. 2 mm. Thus, the combined thickness of the hybrid plates was 4 mm, which is not a standard thickness for the above-mentioned test standard. In this case, the testing standard specifies a formula for determination of the specimen dimensions. Using the given relationships, a specimen dimension of 4 mm x 20 mm x 40 mm was determined.

For comparability, tests according to DIN EN ISO 14130 should be carried out for conditioned (PV 1200) and unconditioned specimens. The following Table 7 summarizes the test plan for ILSS tests.

Table 7. Test matrix for ILSS tests as per DIN EN ISO 14130

Series	0°	90°
Reference	5	5
PV 1200 (50 cycles)	5	5

6.3.2 TEST RESULTS

Execution and results of climate change test

The climate change test of the hybrid specimens lasted 25 days (50 cycles, see Annex A). The test serves as a short-term test with a time-lapse effect. The equipment employed for these test and the test setup are depicted in Figure 113.

Figure 113. Climate chamber for carrying out climate change test as per PV1200

After the test was finished, the specimens were removed for further evaluation of their bond quality. However, it was found out, that the aged hybrid specimens were no longer bonded together (Figure 114) and further testing of interlaminar shear strength was not possible. Cyclic thermal loads induced in the specimens during the accelerated ageing process act eventually as triggers of the detachment process that was observed.

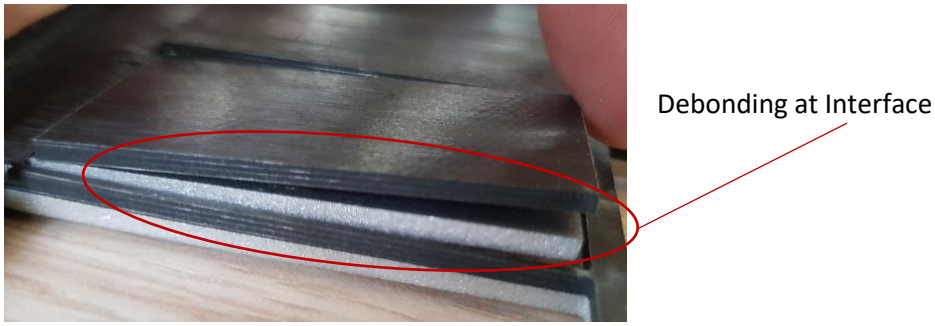

Figure 114. Failure of bonding interface after climate change test

Execution and results of short beam tests

Three-point bending tests were performed for the unconditioned specimens only, since the conditioned specimens failed the climate change test as reported above. The tests were performed with Zwick/Roell Z5.0 machine with a three-point bending test setup. The supports had a radius of 2 mm and the plunger had a radius of 5 mm. According to the measured thickness of samples, i.e. approx. 3.5 mm, the support length was adjusted to 17.5 mm (5 mm x 3.5 mm) as specified by the standard. The specimens were placed on the supports so that the plunger comes first in contact with the metallic side (Figure 115). This ensures that the CFRP side does not get damaged before to the bonding interface. All tests were carried out at room temperature.

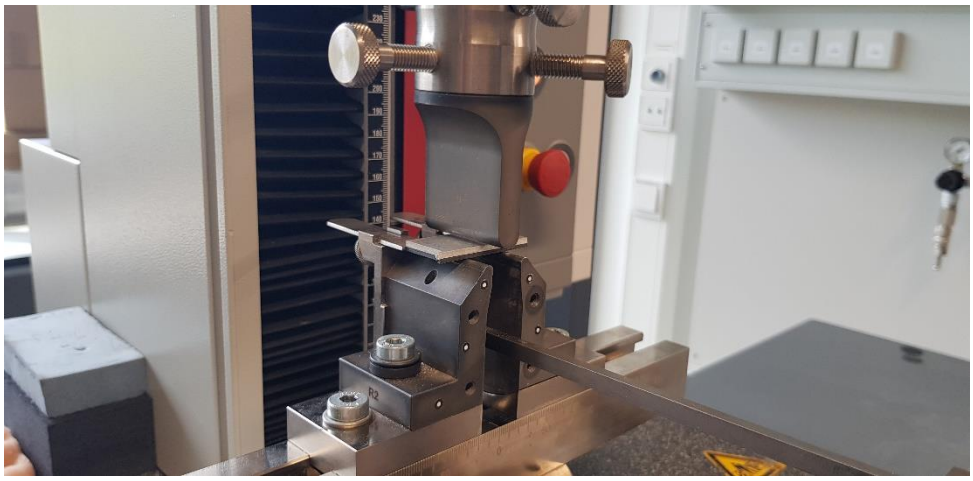

Figure 115: Test setup with mounted specimen

A representative curve from the test is shown in the diagrams below (Figure 116). The curves show the behavior of a hybrid specimen under flexural loading. The force vs. displacement behavior rises in a hyperbolic fashion until a plateau is reached, followed by a sudden drop in the force representing a failure of the bonding interface. The maximum force indicates the apparent shear strength of the bonding interface.

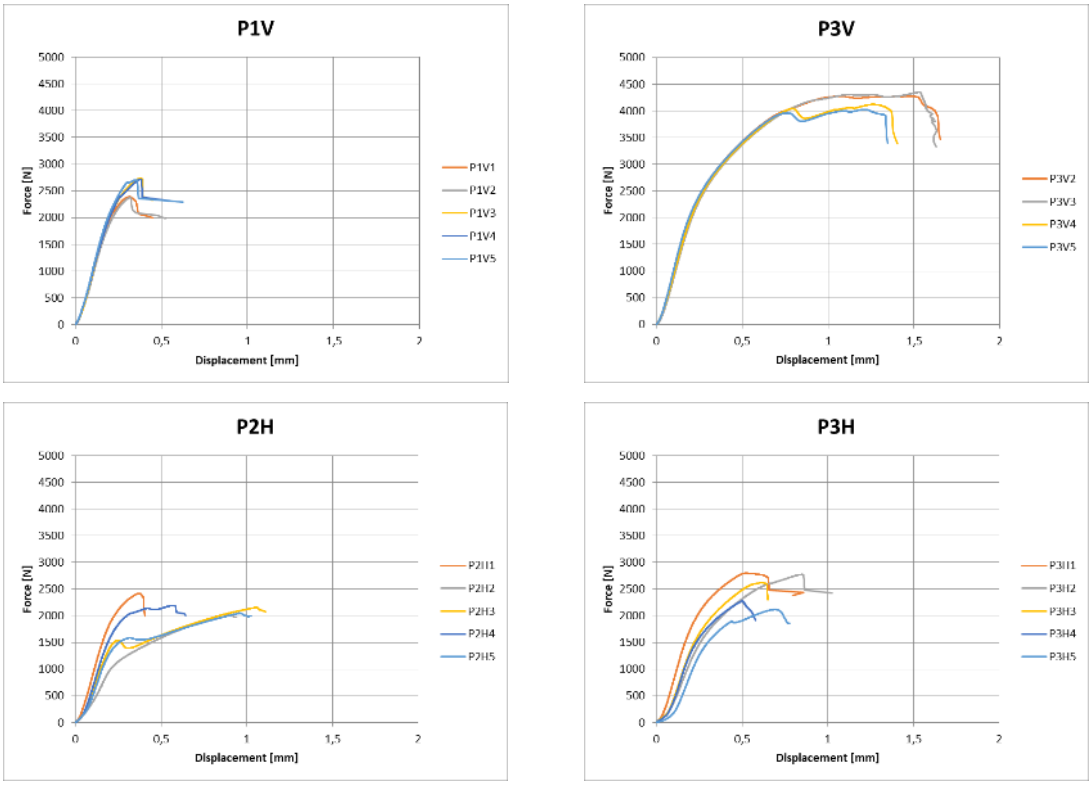

Figure 116: Force-displacement curves obtained during short beam bending tests.

From visual inspection of the specimens (Figure 117) shows that one half of the specimen is completely debonded along its length. This failure mode is characterized as a shear induced failure in DIN EN ISO 14130.

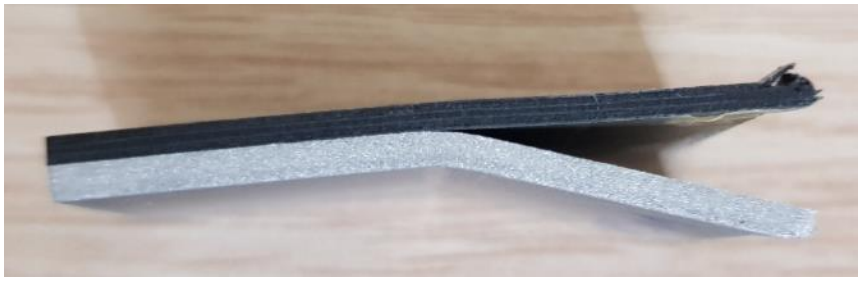

Figure 117: Tested specimen showing shear induced failure

In the diagram below, results of the four tested series are represented. As it can be seen in Figure 118, there is a large variation within most of the series. Also, the values of the bonding strength are different among the different series. For example, the values of P3V are much higher than P1V, i.e. 37.78 %. This may be caused by the variations in the laminate and specimen preparation steps, such as uneven primer application or uneven pressure distribution in the pressing process. The highest value of the apparent interlaminar shear strength was measured in the series P3V series, i.e. 45 MPa. The lowest value was measured in series P2H with 23.7 MPa (47.78 % less than the highest value). For comparison, typical shear strength of adhesively bonded Al/CFRP were reported to be around 15 MPa in [24]. In another study [25], where the shear strength of adhesively bonded Al and CFRP was optimized, a maximum shear strength of 23.68 MPa was achieved after laser treatment of the aluminum side. Another study [26] measured a shear strength of 9.31 MPa after acetone cleaning of Al and CFRP before adhesive bonding. All above mentioned studies used single-lap shear test for determination of shear strength. Further, these studies considered CF/EP composites, so the results of tests conducted by FRA cannot be directly compared with the results of the referenced studies.

Another important outcome of the results is the fact that the horizontal samples (first ply after primer orthogonal to specimen's longer side) appear to have lower apparent shear strength as compared to the vertical samples. A reason for this behaviour could be the greater contact between dry fibres and the primer in the horizontally cut samples.

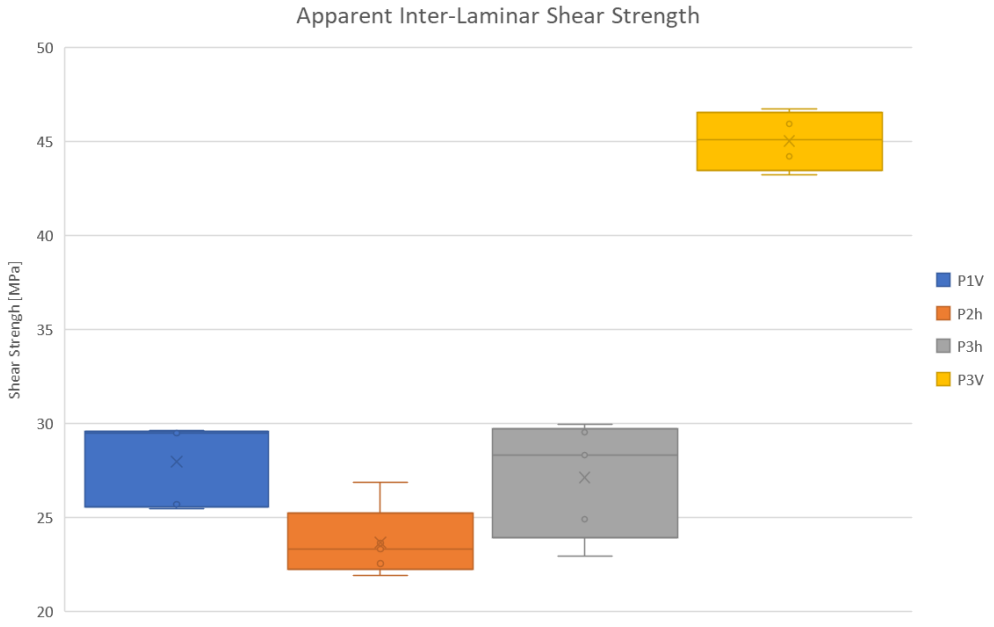

Figure 118: Results of the apparent ILSS tests according to DIN EN ISO 14130

6.4 DISCUSSION ON TEST RESULTS

Al/CFRP hybrid laminates mentioned in D3.1 were tested for their weather endurance and bond strength. The reference series of unconditioned samples show a good bonding strength with a maximum of 45 MPa. However, a high variation of results could be observed various factors, such as manufacturing technique, sample position and orientation, etc.

Furthermore, it was found out that after 50 cycles of climate change tests according to PV 1200, the bonding interface of these laminates failed, resulting in complete debonding. This result implies that such hybrid laminates are not suitable to be used for FES due to their poor durability.

Also, the additional preparation steps of metallic surface by sandblasting or priming are not well suited for large series production applications.

Another important factor is the poor recyclability of hybrid crash structures, which can have a negative environmental impact.

Considering above results as well as economic and environmental aspects, FRA recommends usage of single material (either CFRP or Al) for crash structures (such as crash box) in the SALIENT project.

7. CONCLUSIONS

In this deliverable D3.2 belonging to task T3.2 a detailed reporting of the testing activities performed on the four materials (Al6063, TP/CFRP, SMA/CFRP, hybrid material Al-TP/CFRP) used within Salient to design, manufacture and test a lightweight FES meeting all crashworthiness, sustainability and recyclability requirements is provided. In general terms, this work enables the creation of tailored material cards for the simulations to be carried out within WP5 (reported in D3.2 and to be further optimized within the framework of T5.2) as well as provides some specific insights about the material performance that can be used by the material manufacturers as basis for the optimization activities made in T3.4. Specifically, a short overview of the conclusions obtained per material is provided below:

- **Al6063**: the material performance was as expected for this aluminium grade. Exceptional repetitiveness and quality of results was obtained in all load cases and test conditions. No evident signs of anisotropy were found in the tests specifically designed to analyse this feature. Also, a slight sensitivity to strain rate was observed in the range considered for this applications. All this results are coherent with the available literature on the subject.
- **TP/CFRP**: the material shows exceptional performance at 0º, although failure may be conditioned to the appearance of delamination. In contrast, it presents a very soft behaviour a 90º due to the fact that in this configuration only the matrix is withstanding the applied loads. Therefore, the use of purely UD laminates is not recommended for the design activities. Moreover, a multitude of loading conditions (tensile, compression, bending) and failure mechanisms (translaminar and interlaminar fracture toughness) was characterized.
- **SMA/CFRP**: several material configurations were tested under tensile and bending load cases, in the latter also at different temperatures. Two objectives were pursued in these characterizations: check the potential of the SMA wires to modify the behaviour of the TP/CFRP, and also to evaluate the quality of the integration of the SMA wires within the TP/CFRP. Some early delaminations were observed when using the biggest wire size (200 µm), what indicates that the behaviour of this material is essentially depending on the manufacturing process parameters involved.
- **Hybrid Al-TP/CFRP**: the main objective of the characterization made on this material was to evaluate the appropriateness of the adhesion between the two base materials by means of short beam bending tests. Also the long term durability of the material was assessed through and ageing process widely used in the automotive sector. While the as-manufactured coupons showed a suitable behaviour, none of the coupons remained unaltered after the ageing process due to debonding. Hence, this material is not recommended to be used in the FES.

REFERENCES

[1] J. P. Rojas, J. E. González-Hernández, J. M. Cubero-Sesin, Z. Horita and D. González-Flores, "Benchmarking of Aluminum Alloys Processed by High-Pressure Torsion: Al-3% Mg Alloy for High-Energy Density Al–Air Batteries," Energy & Fuels, vol. 37, no. 6, pp. 4632-4640, 2023.

[2] ASTM E8: Standard test methods for tension testing of metallic materials

[3] Digital Image Correlation (DIC). Extracted from: https://www.dantecdynamics.com/solutions/digital-image-correlation-dic/

[4] ISO 8253: Plastics – Determination of tensile-impact strength.

[5] R. Smerd, S. Winkler, C. Salisbury, M. Worswick, D. Lloyd, M. Finn. High strain rate tensile testing of automotive aluminum alloy sheet, International Journal of Impact Engineering, Volume 32, Issues 1–4, 2005, Pages 541-560, ISSN 0734-743X, https://doi.org/10.1016/j.ijimpeng.2005.04.013.

[6] Ezio Cadoni, Matteo Dotta, Daniele Forni, Hanspeter Kaufmann, Effects of strain rate on mechanical properties in tension of a commercial aluminium alloy used in armour applications, Procedia Structural Integrity, Volume 2, 2016, Pages 986-993, ISSN 2452-3216, https://doi.org/10.1016/j.prostr.2016.06.126.

[7] Khlif, M., Aydi, L., Nouri, H., Bradai, C. (2018). High Strain-Rate Tensile Behaviour of Aluminium A6063. In: Haddar, M., Chaari, F., Benamara, A., Chouchane, M., Karra, C., Aifaoui, N. (eds) Design and Modeling of Mechanical Systems—III. CMSM 2017. Lecture Notes in Mechanical Engineering. Springer, Cham. https://doi.org/10.1007/978-3-319-66697-6_84

[8] ASTM D790-17: Standard test methods for flexural properties of unreinforced and reinforced plastics and electrical insulating materials.

[9] J. C. Farias-Aguilar, M. J. Ramírez-Moreno, L. Téllez-Jurado and H. Balmori-Ramírez, "Low pressure and low temperature synthesis of polyamide-6 (PA6) using Na0 as catalyst," Materials Letters, vol. 136, pp. 388-392, 2014.

[10] H. O. Pierson,, Handbook of carbon, graphite, diamonds and fullerenes: processing, properties and applications., William Andrew, 1994.

[11] ASTM D3039: Standard test method for tensile properties of polymer matrix composite materials.

[12] ASTM D6641: Standard test method for compressive properties of polymer matrix composite materials using a combined loading compression test fixture.

[13] ASTM D5045: Standard Test Methods for Plane-Strain Fracture Toughness and Strain Energy Release Rate of Plastic Materials

[14] ASTM E399: Standard Test Method for Linear-Elastic Plane-Strain Fracture Toughness K_{Ic} of Metallic Materials

[15] Yousef Saadati, Gilbert Lebrun, Christophe Bouvet, Jean-François Chatelain, Yves Beauchamp. Study of translaminar fracture toughness of unidirectional flax/epoxy composite. Composites Part C: Open Access, Volume 1, 2020, 100008, https://doi.org/10.1016/j.jcomc.2020.100008.

[16] ASTM E1922: Standard Test Method for Translaminar Fracture Toughness of Laminated and Pultruded Polymer Matrix Composite Materials

[17] ASTM D5528: Standard Test Method for Mode I Interlaminar Fracture Toughness of Unidirectional Fiber-Reinforced Polymer Matrix Composites

[18] ISO 15114: Fibre-reinforced plastic composites — Determination of the mode II fracture resistance for unidirectionally reinforced materials using the calibrated end-loaded split (C-ELS) test and an effective crack length approach

[19] Murray BR, Fonteyn S, Carrella-Payan D, Kalteremidou K-A, Cernescu A, Van Hemelrijck D, et al. Crack Tip Monitoring of Mode I and Mode II Delamination in CF/Epoxies under Static and Dynamic Loading Conditions Using Digital Image Correlation. The 18th International Conference on Experimental Mechanics 2018. https://doi.org/10.3390/icem18-05225.

[20] ISO 14125: Fibre-reinforced plastic composites – Determination of flexural properties

[21] N. I. N. Haris, M. Z. Hassan, R. Ilyas, M. A. Suhot, S. Sapuan, R. Dolah, R. Mohammad and M. Asyraf, “Dynamic mechanical properties of natural fiber reinforced hybrid polymer composites: a review,,” Journal of Materials Research and Technology,, vol. 19, pp. 167-182, 2022.

[22] https://www.aso-skz.de/branchen/automotive/pruefnormen/pv-1200

[23] DIN EN ISO 14130: Fibre-reinforced plastic composites — Determination of apparent interlaminar shear strength by short-beam method

[24] Technologies for Lightweight Structures 3(1) (2019), pp. 1–8, Special issue: 4th International MERGE Technologies Conference (IMTC), 18th–19th September 2019, Chemnitz

[25] M. Ö. Bora et al, Comparison of novel surface treatments of Al 2024 alloy for al/cfrp adhesive bonded joints, International Journal of Adhesion and Adhesives, Volume 103, 2020, 102721, ISSN 0143-7496, https://doi.org/10.1016/j.ijadhadh.2020.102721

[26] K. Diharjo et al., Effect of Adhesive Thickness and Surface Treatment on Shear Strength on Single Lap Joint Al/CFRP using Adhesive of Epoxy/Al Fine Powder, AIP Conference Proceedings 1710, 030030 (2016), https://doi.org/10.1063/1.4941496

ANNEX A

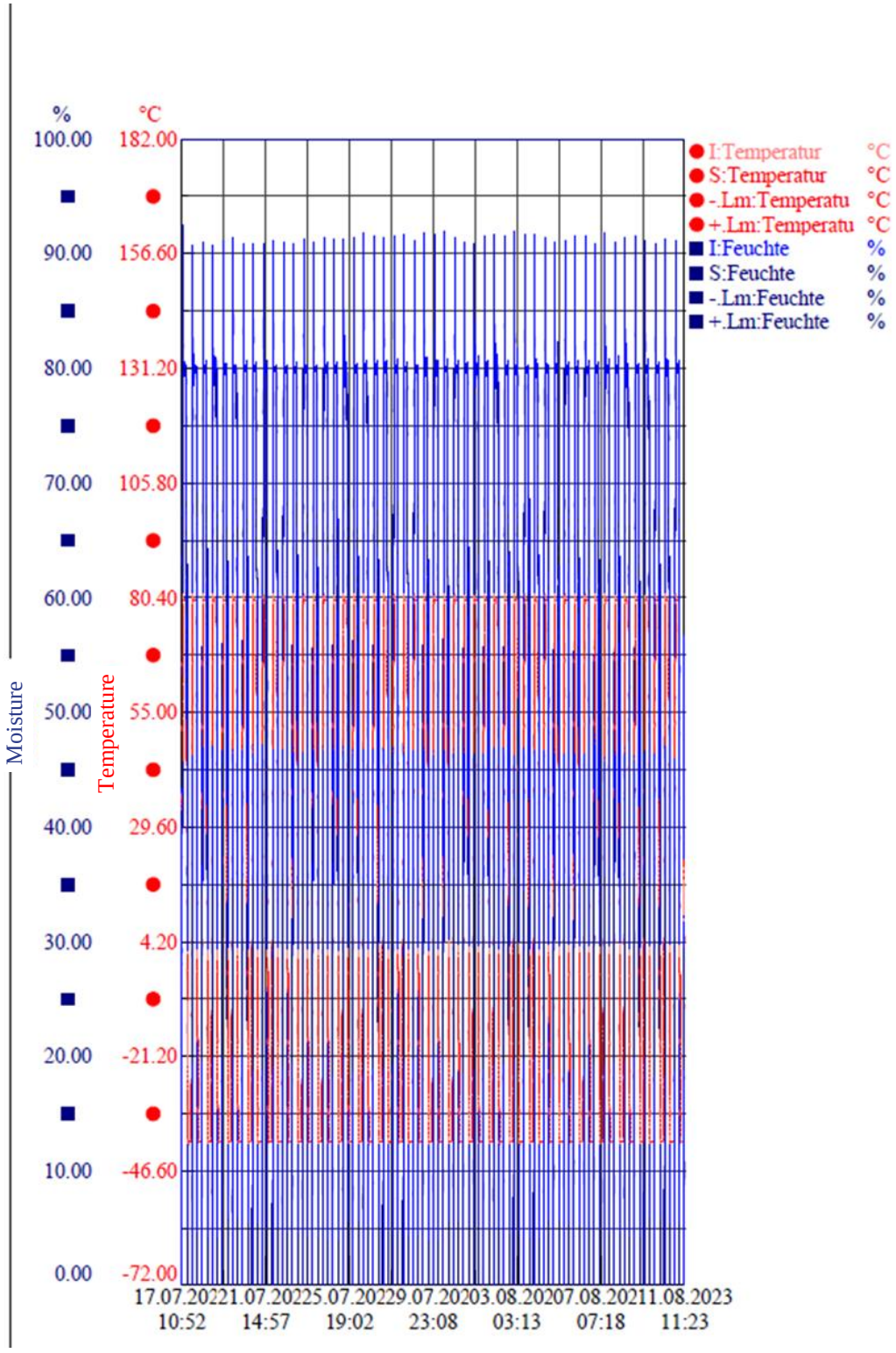

Figure 119. PV1200 Climate change test performed at FRA